Università degli studi di Padova
Dipartimento di Fisica e Astronomia "Galileo Galilei"
Master Degree in Physics

Final Dissertation

Solving the collective Schrödinger equation to study fission rates

Thesis supervisor
Prof. Lorenzo Fortunato
Università degli studi di Padova

Thesis co-supervisor
Dr. Wouter Ryssens
Université libre de Bruxelles

Candidate
Daniel Castiblanco

Academic year 2025/2026

Abstract

Spontaneous fission proceeds from the ground state by pure quantum tunneling through a fission barrier, and because the rate is exponential in the barrier action, half-lives span around 35 orders of magnitude across the chart. The tunneling probability is almost always evaluated with the Wentzel-Kramers-Brillouin (WKB) approximation, whose accuracy has not been assessed systematically across a wide range of nuclei. This thesis provides that assessment by solving the one-dimensional collective Schrödinger equation numerically along microscopic fission paths and quantifying the deviation of the WKB half-lives from the exact ones. A dedicated solver integrates the collective Schrödinger equation, with its coordinate-dependent inertia, using a Runge-Kutta RK5(4) scheme; the transmission coefficient is extracted from the transmitted amplitude after truncating the barrier to impose plane-wave asymptotics. The physical input is the BSkG3 energy-density-functional dataset (MOCCa code): potential energy surfaces and perturbative cranking inertias, from which least-action paths are extracted using the quadrupole moment as the collective coordinate.

Applied to more than 3200 nuclei with available BSkG3 fission paths at a zero-point energy of 0.5 MeV above the ground state, WKB stays within about 0.2 orders of magnitude of the exact result for the large majority, consistently across half-lives spanning more than 200 orders of magnitude. The residual offset was traced to a boundary-reflection effect at the barrier feet, produced by the physically-motivated truncation of the barrier. About 1.3% of the nuclei depart by more than half an order of magnitude, and by up to 3–4, through resonances from quasi-bound states of the isomeric well, a genuinely quantum effect that WKB cannot capture by construction. No significant correlations are found between the deviation and different fission barrier features such as A, Z, height or length ($|\rho| \leq 0.4$). The sensitivity of the deviation to the choice of the zero-point energy was studied, revealing a distribution peaking at 0.3–0.4 orders of magnitude below about 1.5 MeV, settling near zero above roughly 2 MeV. Apart from resonances, the deviation is thus bounded below one order of magnitude already at a few MeV, making it only mildly sensitive to this choice; however, the absolute half-lives are not, given their enormous span and exponential behavior, and the proper choice of this energy remains an open discussion.

Overall, the semiclassical treatment is not the limiting approximation in current large-scale SF predictions: the entire WKB-Schrödinger spread sits comfortably within the deviation of state-of-the-art EDF half-lives from experiment. The exact solver nonetheless matters for individual nuclei near a resonance, and offers a natural route to multi-dimensional fission paths, where the notion of a unique path breaks down and tunneling amplitude can branch across competing valleys.

Keywords: spontaneous fission, half-life, collective Schrödinger equation, WKB approximation, least-action path, BSkG3, collective inertia, class-II resonances.

Contents

List of Figures

Chapter 1

Introduction

Nuclear fission is the process in which a heavy nucleus, made of Z protons and N neutrons, splits into two (occasionally more) lighter fragments. It is a typical example of *large-amplitude collective motion* in a quantum many-body system [1]: the nucleus deforms far beyond the small vibrations of its ground state, so that the whole system rearranges itself rather than a single particle being emitted. This makes fission one of the most challenging nuclear processes to model accurately [2]. This process results from the competition between the nuclear surface tension, favoring compact shapes, and the Coulomb repulsion among protons, favoring elongated ones; this balance is measured by the fissility $x \approx Z^2/[50.88\,A(1-\eta I^2)]$, with $I = (N-Z)/A$ the nucleon asymmetry (and $\eta \approx 1.7826$). For $x > 1$ the nucleus becomes unstable against fission, as in actinides and transactinides [3]. Fission can be *induced* by a reaction with neutrons, protons or photons, and is then characterized by the properties of the fragments, or occur *spontaneously* from the ground state, and be characterized by its half-life $t_{1/2}^{\mathrm{SF}}$, the time it takes for half of a sample of such nuclei to undergo fission [3]. This work is interested in spontaneous fission (SF), where the nucleus reaches the two-fragment configuration by *quantum tunneling* through a potential barrier.

Since the fissility grows as Z^2, spontaneous fission is one of the main mechanisms limiting the existence of superheavy elements, and the search for the next island of stability depends largely on accurate SF half-lives [1, 3]. It plays an equally important role in astrophysics: simulations of neutron-star mergers suggest a rapid neutron-capture process (the *r-process*) with *fission recycling*, in which the flow builds up heavier and heavier nuclei until they fission back into lighter fragments, which then capture neutrons again and repeat the cycle [3, 4]. Fission properties thereby shape the resulting abundances and the heating that powers kilonovae [4, 5]. The nuclei involved lie far from stability, in regions the scarce experimental data does not cover, so the key challenge is predictive power: how reliably a model extrapolates to neutron numbers where no measurement exists [2]. Beyond astrophysics, fission is relevant to nuclear technology, from energy production to forensics and non-proliferation [1], and it is a demanding test of nuclear models, since its description is sensitive to essentially all aspects of an energy density functional [2, 6].

In practice, these half-lives are almost always computed with the semiclassical Wentzel-Kramers-Brillouin (WKB) approximation [3]. Since fission is best understood as a deformation process, the nucleus is described by a small set of *collective coordinates*, which in most cases are chosen as parameters of its shape, and the energy over this *collective space* defines a potential energy surface (PES). Tunneling is evaluated along a one-dimensional path through that space, and the transmission probability follows from a single integral along it. Two ingredients enter that integral: the potential energy along the path, that is, the fission barrier, and an inertia that plays the role of a mass and measures how much the nucleus resists deformation.

The calculation is delicate. Measured half-lives span more than thirty-five orders of magnitude [3, 7], a direct consequence of the transmission depending exponentially on the inputs: a small error in either ingredient is amplified into many orders of magnitude in the half-life. Neither is under full control: fission barriers are not directly observable and depend on the model used to obtain them, the inertia depends on the prescription adopted for it, and the energy at which tunneling starts is a loosely fixed parameter.

These ingredients are obtained today either in the macroscopic-microscopic framework, from a deformed liquid drop corrected for shell and pairing effects [8], or self-consistently, from constrained Hartree-Fock-Bogoliubov calculations with an energy density functional (EDF) [3], using Skyrme [9] or Gogny [10] parametrizations. Predictions still differ substantially between approaches [3], and considerable effort goes into improving them. A recent example are the large-scale calculations with the BSkG3 functional of [2], which reproduce the 136 known SF half-lives within less than four orders of magnitude without introducing additional parameters [5], and are computationally efficient enough to reach the thousands of neutron-rich nuclei relevant for the *r*-process. Realistic fission paths are therefore now available for a large number of nuclei, all obtained within the same framework.

The tunneling step, by contrast, is treated identically in most of the literature and has hardly been questioned. Alternatives have been proposed, mostly based on functional integrals and imaginary-time mean-field dynamics, which in principle avoid the choice of collective coordinates altogether [11, 12]. In most cases, these have so far been tested on simplified model Hamiltonians, and their connection to the standard WKB formula is still missing [3]. On the other hand, exact solutions, are available only for schematic barriers built from simple analytic shapes [13, 14]. It is not obvious that these conclusions carry over to realistic barriers, since far from stability the fission path cannot in general be approximated by parabolic humps [4], and that is precisely the region where predictions are needed. To the best of our knowledge, the accuracy of the WKB step has never been quantified on barriers of microscopic origin, or systematically across the nuclear chart.

The aim of this work is therefore to test the WKB approximation against the solution of the problem it approximates, the one-dimensional collective Schrödinger equation, of which the WKB formula is the semiclassical limit. Three objectives follow. The first is to implement a solver for that equation, able to handle realistic fission barriers of microscopic origin together with their coordinate-dependent inertia. The second is to quantify the deviation of the WKB half-lives from the exact ones and to characterize its systematics over thousands of nuclei, both quantitatively and in the qualitative features that WKB cannot reproduce by construction. The third is to establish whether going beyond WKB is needed in large-scale calculations of spontaneous fission and, if so, for which nuclei. The comparison is carried out along fission paths obtained from EDF calculations performed with the MOCCa code using the BSkG3 functional, following the procedure of [2], with the quadrupole moment as the collective coordinate and keeping axial symmetry.

This thesis is organized as follows. Chapter 2 develops the theoretical framework: the origin of the PES and of the collective inertia in microscopic calculations, the collective Schrödinger equation, and the derivation of the WKB transmission coefficient from it. Chapter 3 then presents the numerical methods, together with their validation on analytically solvable and double-humped barriers and the corresponding stability and accuracy tests. Finally, chapter 4 applies the solver to the microscopic fission paths and studies the systematics of the deviation across the chart, as well as its dependence on the barrier features and on the zero-point energy.

Chapter 2

Modelling fission in a collective space

In order to describe a complex phenomenon such as fission from a microscopic point of view, a simpler alternative approach beyond the difficult quantum many-body problem is often adopted. The standard strategy, and the one considered in this work, is instead to reduce the problem to the slow evolution of a few *collective coordinates* (usually related to the deformation of the nucleus) as it moves from its ground state towards *scission*, the point at which the nucleus splits into two fragments. This reduction is justified by the *adiabatic approximation*. Within this picture, the fission dynamics are governed by two ingredients: the *potential energy surface* (PES), which encodes the fission barriers, and the *collective inertia tensor*, which plays the role of a (coordinate-dependent) mass. Both can be obtained from microscopic frameworks such as the *energy density functional* (EDF) theory, built on the *Hartree-Fock-Bogoliubov* (HFB) equations, with the inertia arising naturally from the *generator coordinate method* (GCM) or the *adiabatic time-dependent HFB* (ATDHFB) approach. These ingredients are the input to a *collective Schrödinger equation*, whose solution determines the transmission across the barrier and, ultimately, the spontaneous fission half-life $t_{1/2}$.

This chapter collects the details of this framework as found in the literature. Section 2.1 motivates the choice of collective coordinates and the adiabatic approximation. Section 2.2 introduces the PES and the collective inertia, together with the frameworks from which they emerge and are calculated. Section 2.3 discusses tunneling along the fission path, the *least action path* (LAP) and the connection to the half-life through the traditionally used *Wentzel-Kramers-Brillouin* (WKB) approximation. Finally, sections 2.4–2.5 derive, in more detail than is usually found in the literature, the collective Schrödinger equation by quantizing the collective Hamiltonian and recover the WKB transmission coefficient as its semiclassical limit directly from it in one dimension. Section 2.6 briefly discusses how the well-known formula for the transmission coefficient can be extended to multi-dimensional collective spaces from the collective Schrödinger equation.

2.1 Collective spaces

Fission constitutes a many-body problem with a large number of degrees of freedom, involving large-amplitude motion and important correlation effects, making it a particularly challenging and complex problem. Fortunately, the evolution of the fissioning system can be modeled in terms of a more tractable number of macroscopic parameters, which has proved to be fruitful in semi-phenomenological and microscopic approaches [3].

Therefore, the first step in most current fission approaches is the choice of a set of *collective coordinates*; these are assumed to dominate the fission dynamics. This is the *adiabatic approximation*, which states that: (i) the collective motion of the system is slow compared to the single-particle

motion of the individual nucleons [15], and (ii) there is a decoupling between the motion in collective space and the intrinsic motion of individual nucleons [1]. This hypothesis is reasonable in the case of fission (at least at low energies): the time from saddle to scission is typically of the order of 10^{-19} s, which is about three orders of magnitude slower than the time scale associated with the average binding energy per nucleon $B \approx 8$ MeV ($\sim \hbar/B \approx 10^{-22}$ s) [3, 16].

Although there is some freedom in the choice of these collective variables, the success of semi-phenomenological approaches suggests using a small number of collective coordinates related to the shape evolution of the nucleus and its deformation [3, 16].

The choice of deformation coordinates is well-motivated. Although the notion of nuclear deformation was originally introduced to account for spectroscopic observables, it has a deeper origin as a spontaneous symmetry breaking of the nuclear mean field, whose average potential is no longer invariant under rotations [1]. In the case of fission, the deformation of the nucleus at scission is closely connected to the distribution of the fission fragments, while the overlaps between states at different deformations is directly related to the fission probabilities [1].

In practical applications, between one to four of these collective coordinates are used to describe the collective motion [17, 18]. In nuclear DFT approaches, each collective variable is defined as the expectation value of a one-body operator, and the HFB equations are solved under constraints on these expectation values [3, 17, 19]. This is described in detail in the next section.

The traditional choice of collective variables to describe the shape of the nucleus is based on the multipole moments q_{lm}, expectation values of the multipole moment operators [3, 5]:

$$q_{lm} \equiv \langle \hat{Q}_{lm} \rangle = \mathrm{tr}(\hat{Q}_{lm}\hat{\rho}) = C_{lm} \int r^l \mathrm{Re}(Y_{lm}(\theta,\phi))\rho(\mathbf{r})\ \mathrm{d}^3\mathbf{r}\,, \tag{2.1}$$

where (r, θ, ϕ) are the spherical coordinates, Y_{lm} are the spherical harmonics, C_{lm} are constant factors depending on convention and $\hat{\rho}$ is the nuclear one-body mass density operator. Such operators are loosely related to the multipole expansion of the nuclear surface in macroscopic-microscopic methods [18]. This choice is mostly justified by the experimental observation of low-energy vibrational states of quadrupole, octupole, etc. character, and have been applied consistently for fission with success [19].

Among these, the most natural coordinate to describe fission is the *quadrupole deformation* q_{20}, which governs the overall elongation of the nucleus [20, 21]. For a more thorough description of the nuclear shape, the *octupole deformation* q_{30} and *second quadrupole* q_{22} can be included. The former describes deviations from reflection symmetry, introducing mass asymmetry of fission fragments, useful for actinides [3]. The latter characterizes the degree of *triaxial* deformation, applicable to deviations of axial symmetry in the nucleus' evolution to fission [20]. Both of these provide significant reduction of the fission barriers for actinide nuclei compared to just considering q_{20} [5].

Other useful constraints act more directly on the scission shape and the properties of the fission fragments. These include the *hexadecapole moment* q_{40}, which influences neck formation [17], and the *neck operator* $\hat{Q}_N$, whose expectation value $\langle \hat{Q}_N \rangle = \langle \exp(-(z - z_\mathrm{N})^2/a_\mathrm{N}^2) \rangle$ measures the number of particles in the neck region connecting the prefragments, located at position z_N with width $a_\mathrm{N} \approx 1$ fm [19, 21].

Multipole moments are not the only possibilities: fission observables are sensitive to pairing correlations and particle fluctuations, which have been shown to be important to describe the fission process [22]. More specifically, for example, increasing pairing correlations decreases the fission barrier and lead to scission occurring at lower elongations and imply a strong decrease of the inertia [3, 23]. Collective variables such as the average of the pairing gap within the BCS formalism and the expectation value of the fluctuation of number of particles (for both types of nucleons) are some of the most important ones to consider [3].

2.2 Potential energy surface and collective inertia

Once a collective space is chosen, a collective Hamiltonian in these variables should be constructed from microscopic arguments, in principle. This Hamiltonian will provide an effective potential and mass, or inertia.

The *collective inertia* and the potential, the latter more commonly referred to as the *potential energy surface* (PES), are the two main ingredients for the theoretical determination of spontaneous fission lifetimes within the adiabatic approximation.

Semi-phenomenological choices of the form of the inertia and the potential are also common options. In this case, the potential is often taken from a macroscopic-microscopic approach, e.g., based on a deformed liquid-drop description with shell and pairing corrections, and the inertia is taken from a cranking method or parametrized empirically [3, 24].

The PES, that is, the potential energy as a function of the collective variables, determines the fission paths and governs the large-amplitude dynamics of the nucleus [1]. The PES can be used to locate fission barriers and estimate fission rates based on its properties. The PES is also the starting point for many dynamical (time dependent) calculations of the fission process [25]. The differences in the characteristics of barriers of nuclei qualitatively explains the range of spontaneous fission half-lives observed experimentally. Even in neutron-induced fission, the time from saddle to scission is also strongly dependent on the characteristics of the PES [25].

Key information can be extracted from it by a projection on a one-dimensional subspace: the *fission path*. This has the added benefit of avoiding the difficulty of visualizing a multi-dimensional PES directly. In most actinide nuclei, this path is typically characterized by a first minimum of the potential, corresponding to the *ground state*, and a second, meta-stable minimum at larger deformation: the *fission isomer* [1]. These two minima are separated by potential energy barriers in most actinides: the *inner barrier*, lying between the ground state and the fission isomer, and the *outer barrier*, lying between the fission isomer and the region of increasing deformation that leads towards scission. Although double-humped fission barriers are the most common case for actinides, some calculations seem to predict a triple-humped barrier with a very shallow isomer for ^{232}Th and other actinides, for example [26]. Transactinides are mostly single-humped: fission isomers are generally suppressed in superheavy elements, which is predicted by different models [27]. These fission barriers are fundamental for the tunneling process and therefore for the calculation of fission half-lives.

The collective inertia, on the other hand, contains the response of the nucleus to a change in the collective variables and effectively plays the role of the mass of the collective wave-packet [1]; as we will see, it takes precisely the form of a (coordinate-dependent) mass in the Schrödinger equation written in the collective variables. It is a considerably more abstract object than the PES: it is not simply the mass of the nucleus, and its evaluation is far from simple. Both arise naturally in the classical as well as the quantum treatment of the dynamics in collective space, and in particular in microscopic approaches such as the GCM and ATDHFB. As we will see, they both have a strong influence on the calculation of half-lives, since they enter the definition of the WKB action and therefore affect the predicted lifetimes exponentially.

Before discussing the collective Hamiltonian, and therefore the collective Schrödinger equation, in the next section, we can describe more precisely how the potential and inertia emerge from more microscopic approaches.

2.2.1 Energy density functional theory (EDF)

Since in nuclear theory the number of degrees of freedom of the many-body system involved makes an exact determination of nuclear observables intractable in practice, the energy density functional theory (EDF) has become one of the most widely used frameworks for the description of the nuclear many-body system.

Density functional theory (DFT) has its roots in the *Hohenberg-Kohn theorem*, which shows that the total energy of a many-fermion system can be expressed in terms of an *energy density functional* (EDF) depending only on the local one-body density distribution ρ, a quantity with a clear physical meaning that can be accessed experimentally [28, 29][1]. Therefore, DFT allows one to establish a mapping between the strongly interacting many-body system and a functional theory that can be solved from a mean-field perspective.

By reformulating the problem in terms of one-body densities, the computational cost is lessened and the number of degrees of freedom is considerably reduced, potentially allowing one to describe nuclei across the whole chart of nuclides. EDF is currently the only microscopic framework able to address the full diversity of nuclear phenomena across the entire nuclear chart: nuclear spectroscopy, small- and large-amplitude dynamics, and equilibrium and non-equilibrium thermodynamics [32].

The density alone does not determine the ground-state energy: in the nuclear case, where nuclei are self-bound and correlations are strong, superfluidity plays a central role. As a result, the nuclear energy density functional is determined by the pairing densities as well. The energy can therefore be expressed as a functional of the intrinsic, one-body, non-local density matrix ρ and the non-local pairing tensor κ: $E = E[\rho, \kappa, \kappa^*]$ [3].

These pairing correlations are reflected in the importance of the Bogoliubov transformation, which we will see in the next section. Other degrees of freedom representing distributions of spin, momentum and kinetic energy are also important, arising from currents and derivatives of the densities [29].

While the existence of a unique density functional for a fermionic system is predicted by DFT, its specific functional form is still to be determined. The EDF can either (i) be parametrized directly from a phenomenological perspective and confronted with experiment, or (ii) be computed from the expectation value of some microscopic Hamiltonian on a quasiparticle vacuum, as explained in the next section. In either case, the functional form depends on a number of free parameters that must be adjusted to experimental data [18].

In the microscopic case, this expectation-value procedure is motivated from the Hohenberg-Kohn theorem which gives a variational principle for the ground state: if $\hat{H}$ is the many-body nuclear Hamiltonian, the ground-state density can be determined as the one for which the energy is minimized, or more precisely [33]:

$$E_{\mathrm{GS}} \equiv E[\hat{\rho}_{\mathrm{GS}}] = \min_{\hat{\rho}} E[\hat{\rho}] = \min_{\Phi} \frac{\langle \Phi | \hat{H} | \Phi \rangle}{\langle \Phi | \Phi \rangle}, \tag{2.2}$$

where $\{|\Phi\rangle\}$ is the set of HFB wave functions, introduced in the next section.

In practice, EDFs have been based on in-medium, two-body effective nuclear interactions (or pseudo-potentials), such as the zero-range Skyrme force or the finite-range Gogny force.

[1] Applying the Hohenberg-Kohn theorem to nuclei is not entirely straightforward, since the theorem is formulated for a system bound by an external potential, such as electrons in a Coulomb field, while nuclei are self-bound. The formalism is usually justified by reformulating the theorem for the *intrinsic* density defined in the center-of-mass frame [30, 31], though whether it holds as rigorously as in the electronic case remains a somewhat open question.

In the Skyrme case, the effective interaction is written as a delta function in the relative coordinate, supplemented by momentum-dependent (gradient) terms that mimic finite range, plus a density-dependent term that captures three-body effects, all controlled by a set of parameters [34]. Many parametrizations of this functional have been proposed over the years, but parametrizations such as SkM* or UNEDF1 are among the most used since they provide well-calibrated deformation properties commonly used in fission applications [18].

A well-suited choice for this purpose is the Brussels-Skyrme-on-a-Grid (BSkG) series, whose goal is to provide consistent nuclear data for astrophysical applications, competitive with more phenomenological approaches while remaining fully microscopic [5]. It reproduces the 45 primary and secondary barriers with rms (root-mean-square) errors of 0.33 and 0.51 MeV and 28 isomer excitation energies with an rms of 0.36 MeV, alongside global rms deviations of 0.631 MeV and 0.024 fm for all known masses and charge radii [35]. On this basis, BSkG3, from which the dataset used in this work was obtained, reproduces all known SF half-lives within less than four orders of magnitude from large-scale EDF calculations, with no additional parameters [2].

The Gogny force can be seen as a modification of the Skyrme potential where the zero-range central potential is replaced by the sum of two Gaussians in the spatial part [3]. Although finite-range interactions are an improvement over Skyrme, Gogny calculations are far more computationally expensive, making Skyrme the preferred choice for large-scale fission calculations. The D1S parametrization is the most used in the Gogny case for fission applications [18].

Currently, however, most modern nuclear DFT applications do not assume the energy density functional to derive from any given effective Hamiltonian; the functional is instead postulated directly, without reference to an underlying effective interaction [29].

2.2.2 PES calculation: the HFB equation

As mentioned before, the EDF approach is largely built on the Hartree-Fock-Bogoliubov (HFB) theory. In this approach, quasiparticles are introduced using a set of annihilation and creation operators $\{\beta_i,\ \beta_i^\dagger\}_{i=1}^{N_\mathrm{b}}$, instead of the single-particle operators $\{c_i, c_i^\dagger\}_{i=1}^{N_\mathrm{b}}$ of the Fock space (with N_b the size of the single-particle basis set, usually truncated). These two sets are related by the *Bogoliubov transformation*, the most general linear transformation between these operators:

$$\beta_i = \sum_j U_{ji}^* c_j + V_{ji}^* c_j^\dagger, \qquad \beta_i^\dagger = \sum_j U_{ji} c_j^\dagger + V_{ji} c_j. \tag{2.3}$$

This can be written in matrix form as:

$$\begin{pmatrix} \beta \\ \beta^\dagger \end{pmatrix} = \mathsf{W}^\dagger \begin{pmatrix} c \\ c^\dagger \end{pmatrix}, \qquad \mathsf{W} \equiv \begin{pmatrix} \mathsf{U} & \mathsf{V}^* \\ \mathsf{V} & \mathsf{U}^* \end{pmatrix}. \tag{2.4}$$

where $(\mathsf{V})_{ij} = V_{ij}$ and $(\mathsf{U})_{ij} = U_{ij}$ are the Bogoliubov transformation matrices. It can be proven that the Bogoliubov transformation is unitary because the quasiparticle operators must satisfy the usual anticommutation relations as the old ones [33]. The HFB theory considers the vacuum corresponding to the quasiparticle operators as an approximation of the ground state wavefunction of the many-body system. Therefore, the ground state can be constructed as follows:

$$|\Phi\rangle = \prod_i \beta_i \,|-\rangle\,, \tag{2.5}$$

where $|-\rangle$ is the vacuum state. The density matrix and pairing tensor can be calculated in the HFB formalism as follows:

$$\rho_{ij} \equiv \langle\Phi|c_j^\dagger c_i|\Phi\rangle = (\mathsf{V}^*\mathsf{V}^{\mathrm{T}})_{ij}, \qquad \kappa_{ij} \equiv \langle\Phi|c_j c_i|\Phi\rangle = (\mathsf{V}^*\mathsf{U}^{\mathrm{T}})_{ij}. \tag{2.6}$$

A generalized density matrix can be defined to encapsulate all the degrees of freedom of the theory as follows:

$$\mathsf{R} \equiv \begin{pmatrix} \langle\Phi|c_j^\dagger c_i|\Phi\rangle & \langle\Phi|c_j c_i|\Phi\rangle \\ \langle\Phi|c_j^\dagger c_i^\dagger|\Phi\rangle & \langle\Phi|c_j c_i^\dagger|\Phi\rangle \end{pmatrix} = \begin{pmatrix} \rho & \kappa \\ -\kappa^* & 1-\rho^* \end{pmatrix}. \tag{2.7}$$

It can be shown that this matrix satisfies that $\mathsf{R}^2 = \mathsf{R}$. This condition, analogously present in HF theory ($\rho^2 = \rho$), ensures that the quasiparticle vacuum is a physical state: their eigenvalues must be 0 or 1 and respects the relations between ρ and κ ($\rho^2 - \rho = -\kappa\kappa^\dagger$ and $\rho\kappa = \kappa\rho^*$).

In the spirit of equation (2.2), the HFB equations can be obtained by minimizing the energy functional $E = E[\mathsf{R}]$ in the manifold of R matrices, under the condition that the HFB solution remains a quasiparticle vacuum, that is, $\mathsf{R}^2 = \mathsf{R}$. By introducing a set of Lagrange multipliers, the variation can be written as follows [3, 21]:

$$\delta E'_{\mathrm{HFB}}[\mathsf{R}] \equiv \delta\left\{E[\mathsf{R}] - \mathrm{tr}\big(\Lambda(\mathsf{R}^2 - \mathsf{R})\big) - \sum_{q=\mathrm{n,p}} \lambda_q(\langle\hat{N}_q\rangle - N_q) - \sum_{lm} \lambda_{lm}(\langle\hat{Q}_{lm}\rangle - q_{lm})\right\} = 0, \tag{2.8}$$

where Λ is a matrix of (undetermined) multipliers. Equation (2.8) has some additional Lagrange multipliers for constraints on, for example, the particle number and the multipole operators (as discussed in the previous section):

$$\langle\hat{N}_{q=\mathrm{n,p}}\rangle = N_{q=\mathrm{n,p}}, \qquad \langle\hat{Q}_{lm}\rangle = q_{lm}. \tag{2.9}$$

By construction, the quasiparticle vacuum is not an eigenstate of the particle number operator, and therefore, it is always necessary to impose a constraint on proton and neutron particle numbers [3]. In fission studies, the collective space can also be explored by seeking solutions to the HFB equations that yield specific values of the collective variables: this is how potential energy surfaces are computed in practice.

By taking into account that the particle number and multipole operators are one-body operators:

$$\hat{N}_q = \sum_{ij} \delta_{ij}\delta_{\tau_i,q} c_i^\dagger c_j, \qquad \hat{Q}_{lm} = \sum_{ij} \langle i|\hat{Q}_{lm}|j\rangle\, c_i^\dagger c_j \equiv \sum_{ij} (\mathsf{Q}_{lm})_{ij} c_i^\dagger c_j, \tag{2.10}$$

where τ_i is the particle type of the i-th single particle state (n or p) and $|i\rangle = c_i^\dagger|-\rangle$, it can be proved that the equation (2.8) leads to $[\mathsf{H}', \mathsf{R}] = 0$, where we define:

$$\mathsf{H}' \equiv \begin{pmatrix} \mathsf{h} - \lambda - \sum_{lm} \lambda_{lm}\mathsf{Q}_{lm} & \Delta \\ -\Delta^* & -\mathsf{h}^* + \lambda + \sum_{lm} \lambda_{lm}\mathsf{Q}^*_{lm} \end{pmatrix}, \tag{2.11}$$

where:

$$(\mathsf{h})_{ij} = \frac{\partial E}{\partial \rho_{ij}}, \qquad (\Delta)_{ij} = \frac{\partial E}{\partial \kappa^*_{ij}}, \qquad \lambda = \mathrm{diag}(\lambda_\mathrm{n} \mathbf{1}_\mathrm{n}, \lambda_\mathrm{p} \mathbf{1}_\mathrm{p}). \tag{2.12}$$

This commutator relation implies that both R and H' can be simultaneously diagonalized, and therefore, have a common eigenbasis. It can be shown that the transformation matrix W diagonalizes R, which implies that H' is also diagonalized by W. Using this, the more proper eigenvalue form of the HFB equations can be obtained as follows [33]:

$$\mathsf{H}' \begin{pmatrix} U_k \\ V_k \end{pmatrix} = E_k \begin{pmatrix} U_k \\ V_k \end{pmatrix}, \tag{2.13}$$

where $(U_k)_i = (\mathsf{U})_{ik}$ and $(V_k)_i = (\mathsf{V})_{ik}$ are the k-th columns of the matrices U and V, and E_k is the k-th eigenvalue, which can be identified as a *quasiparticle energy*. Since the matrix H' itself depends on U and V through the ρ and κ dependence in h, Δ and Q_{lm}, the HFB equations (2.8) are in fact a non-linear problem. Along with constraints (2.9), this system of equations must be solved.

The HFB equation is usually solved iteratively, starting from an initial guess for ρ and κ, calculating H', diagonalizing it to obtain U and V and therefore the updated densities (2.6) of the next step. At each step, the Lagrange multipliers λ_q and λ_{lm} are updated by adjusting them until the constraints (2.9) are met. The total energy is calculated at each iteration with $E^{(n)} = E[\mathsf{R}^{(\mathrm{n})}]$, and the process is repeated until convergence, where the difference $\delta E = |E^{(n+1)} - E^{(n)}|$ is smaller than a desired precision (W or R could be used for the difference criteria as well) [3, 36]. The final energy $V(\mathbf{q}) = E[\mathsf{R}, \mathbf{q}]$ yields one point of the potential energy surface.

This procedure is often time-consuming and convergence is not always guaranteed. An alternative popular method is based on the direct minimization of the HFB energy using any of the variants of the gradient method, which follows the line of steepest perpendicular to the gradient with respect to $\hat{Q}_{lm}$ [3, 33].

The value of λ_q for the particle number constraint is usually handled with a root-finding algorithm, remembering that $\langle \hat{N}_q \rangle$ is a function of λ_q since R, and therefore H' depend on λ_q. However, λ_{lm} needs to be handled with care, since in general $\langle \hat{Q}_{lm} \rangle$ is not monotonic with λ_{lm}, in contrast to the previous case. Methods such as the gradient method and the augmented Lagrangian method help to avoid this issue [3, 33].

An expression for the energy functional can be derived from an effective two-body Hamiltonian, as usual in nuclear physics:

$$\hat{H} = \sum_{ij} t_{ij} c_i^\dagger c_j + \sum_{ijkl} \bar{v}_{ijkl} c_i^\dagger c_j^\dagger c_l c_k, \tag{2.14}$$

where t_{ij} and $\bar{v}_{ijkl}$ correspond to the matrix elements of the one-body kinetic operator and the anti-symmetrized elements of the two-body potential [3]. In spirit of equation (2.2), an energy functional can be derived for this Hamiltonian with the expectation value on the HFB ground state, obtaining [33]:

$$E[\rho, \kappa, \kappa^*] = \mathrm{tr}(\mathsf{t}\rho) + \frac{1}{2}\,\mathrm{tr}(\Gamma\rho) - \frac{1}{2}\,\mathrm{tr}(\Delta\kappa^*), \tag{2.15}$$

where $(\mathsf{t})_{ij} = t_{ij}$ and we define the mean field potential and the pairing field as:

$$\Gamma_{ij} = \sum_{kl} \bar{v}_{ijkl} \rho_{lk}, \qquad \Delta_{ij} = \frac{1}{2} \sum_{kl} \bar{v}_{ijkl} \kappa_{kl}. \tag{2.16}$$

Note that these expressions are not applicable to density-dependent potentials since they cannot be expressed as two-body operators, but can still appear separately in the energy functional as rearrangement terms [3, 33].

In all mean-field approaches such as HFB, the ground-state wave function violates fundamental symmetries of the Hamiltonian, namely translational, rotational, parity, and particle number [3, 21]: this is called *spontaneous symmetry breaking*. This is clearly an issue: since the symmetries of the nuclear Hamiltonian are not necessarily conserved anymore, HFB solutions do not have good quantum numbers. Therefore, a correction to the ground-state energy is needed to account for the missing symmetries.

In practice, the type of correction depends on the symmetry considered. Previously, we mentioned that the particle number symmetry breaking is handled (at least in average) by introducing a constraint through a Lagrange multiplier.

Translational symmetry breaking can be treated by correcting the energy from spurious zero-point center-of-mass motion with the correlation energy $E_{\text{c.m.}} \sim -\langle \hat{\mathbf{P}}^2_{\text{c.m.}} \rangle / 2m_{\text{nuc}}A$. This effect varies as much as 1 MeV with deformation for heavy nuclei [3].

Rotational symmetry can be restored with an angular momentum projection, which effect can be approximated with the energy of a deformed nucleus. The correlation energy is then $E_{\text{rot}} \sim -\langle \mathbf{J}^2 \rangle / 2\mathcal{I}$, where $\mathcal{I}$ is the moment of inertia of the deformed nucleus, which is deformation dependent [3, 21]. This is one of the most significant correlation effects, varying up to 7-8 MeV for strongly quadrupole deformed nuclei, but negligible for spherical nuclei [3].

2.2.3 Collective inertia from microscopic approaches

As we mentioned before, in the *single-reference EDF* theory or SR-EDF, which introduces a HFB quasiparticle vacuum as the reference state paired with an energy functional, several symmetries are explicitly broken and some correlation energies can be introduced to account for them. The *multi-reference EDF* theory or MR-EDF provides a systematic way to overcome this limitation. This is a more general approach which describes the quantum mechanics of nuclear collective motion. MR-EDF is not only used to restore symmetry, but also provides a tool of choice to access excited states of the nucleus [32].

In this framework, the *generator coordinate method* (GCM) will also provide a natural description of the collective inertia, and a way to calculate it. The GCM assumes that the many-body wavefunction is a linear superposition of single-reference states labeled by continuous parameters, the generator coordinates:

$$|\Psi\rangle = \int f(\mathbf{q}) \, |\Phi(\mathbf{q})\rangle \, \mathrm{d}\mathbf{q} \,, \tag{2.17}$$

where $\mathbf{q}$ is, in general, a set of collective coordinates, which constrain the single-reference ansatz $|\Phi(\mathbf{q})\rangle$, that is, a HFB state for example. The weight function can be determined from a variational principle on the total energy of the system $E[\Psi] = \langle \Psi | \hat{H} | \Psi \rangle \, / \, \langle \Psi | \Psi \rangle$. This procedure leads to the Hill-Wheeler (HW) equation for the weights $f(\mathbf{q})$:

$$\int [\mathcal{H}(\mathbf{q}', \mathbf{q}) - E\mathcal{N}(\mathbf{q}', \mathbf{q})] f(\mathbf{q}) \, \mathrm{d}\mathbf{q} = 0, \tag{2.18}$$

where $\mathcal{H}(\mathbf{q}, \mathbf{q}') = \langle \Phi(\mathbf{q}) | \hat{H} | \Phi(\mathbf{q}') \rangle \, / \, \langle \Phi(\mathbf{q}) | \Phi(\mathbf{q}') \rangle$ and $\mathcal{N}(\mathbf{q}, \mathbf{q}') = \langle \Phi(\mathbf{q}) | \Phi(\mathbf{q}') \rangle$. This is an integro-differential, non-local in the generator coordinates, and nonlinear. In practice, the full HW equation is very difficult to solve for more than one generator coordinate [25].

A standard simplification, known as the *Gaussian overlap approximation* (GOA), reduces the HW equation to a time-independent Schrödinger-like equation with respect to the generator coordinates. This approximation assumes that the norm overlap $\mathcal{N}(\mathbf{q}, \mathbf{q}')$ is a sharply peaked function around $\mathbf{q} = \mathbf{q}'$ [3, 21], which allows a quadratic expansion of the energy kernel $\mathcal{H}(\mathbf{q}, \mathbf{q}')$ around $\mathbf{q} = \mathbf{q}'$.

This Schrödinger-like equation has a potential $V(\mathbf{q}) = \langle\Phi(\mathbf{q})|\hat{H}|\Phi(\mathbf{q})\rangle$, which is the HFB energy, a zero-point energy correction and a $\mathbf{q}$-dependent mass in terms of a tensor. Therefore, this local approximation provides insight on the collective dynamics, which is driven by the behavior of the PES (with a zero-point correction) and the collective inertia. We will see the form of this collective Schrödinger-like equation in the following sections.

This formalism can be extended to a time-dependent form by replacing the weight function by a time-dependent one, $f(\mathbf{q}, t)$, and applying a variational procedure as in the static case, obtaining the corresponding time-dependent Schrödinger-like equation.

Since fission is intrinsically a dynamical process, where the ground state (or other excited configurations) evolves with time towards a two-fragment solution, time-dependent approaches are a natural framework to describe it. An alternative approach, in which a collective inertia also arises naturally, is the *time-dependent density functional theory* (TDDFT), where the wave function of the system at each time is assumed to remain a product state at all times [1]. This label includes methods such as TDHF and TDHFB. This approach, in principle, offers a more realistic description of fission fragment properties since it does not rely on adiabaticity [3]. Furthermore, TDHF(B) does not require constraints in collective variables during the time evolution and the single particle degrees of freedom are automatically included, which implies that the PES calculation is not required [25].

The TDHF and TDHFB formalisms are referred to as semi-classical, in the sense that they do not allow collective quantum tunneling directly: a calculation initialized inside a well would be expected to remain in that well [1]. For this reason they are not applied directly to spontaneous fission, which proceeds entirely by sub-barrier tunneling from the ground state. TDHFB remains useful in this context, however, as a tool to compute realistic collective inertias for WKB-type calculations, as we detail in the next section, so that the explicit time evolution of the system in collective space is not needed [3].

TDHFB provides an equation of motion for the HFB densities [3, 32]:

$$i\hbar\dot{\mathsf{R}}(t) = [\mathsf{H}[\mathsf{R}(t)], \mathsf{R}(t)], \tag{2.19}$$

where R is the time-dependent version of (2.7) and H is the matrix (2.11) (without the constraints). This expression arises from a time-dependent variational principle restricted to the manifold of HFB states at all times, or alternatively, by calculating the evolution of the components of R with the Ehrenfest theorem and Wick's theorem [32]. Notice how in the static case, the equation reduces to the HFB equation $[\mathsf{H}, \mathsf{R}] = 0$.

In order to get an expression of the inertia, the *adiabatic TDHFB* theory (ATDHFB) considers a further approximation and expands $\mathsf{R}(t)$ around a slowly varying $\mathsf{R}_0(t)$ (time-even) in powers of the collective momenta $\chi_i(t)$ (time-odd):

$$\mathsf{R}(t) = \mathsf{R}_0(t) + \mathsf{R}_1(t) + \mathsf{R}_2(t)..., \tag{2.20}$$

where the expansion is kept to second order (quadratic in the momenta), and the time-odd (R_1) and time-even (R_0, R_2) parts are considered separately [15].

This expansion can be performed similarly to H, which depends on $\mathsf{R}(t)$. Then, the HFB energy (2.15) can be separated into a zero-order term, which resembles the HFB energy with the R_0 density, and a second-order term reminiscing a classic kinetic energy [15]. This kinetic energy-like term

is the origin of the definition of the ATDHFB inertia. The adiabatic approximation also assumes that only a few relevant collective coordinates $\{q_i(t)\}$ are responsible for the time evolution of the system, and therefore, the time derivative of R_0 is reduced in terms of $\dot{q}_i$ through the chain rule: $\dot{\mathsf{R}}_0 = \sum_i \partial_{q_i} \mathsf{R}_0 \dot{q}_i$. With this in mind, it can be shown that the so-called kinetic term and the corresponding inertia take the form [15]:

$$\frac{i\hbar}{4}\,\mathrm{tr}\big(\dot{\mathsf{R}}_0[\mathsf{R}_0,\mathsf{R}_1]\big) \equiv \frac{1}{2}\sum_{ij} M_{ij}\dot{q}_i\dot{q}_j, \qquad M_{ij} = \frac{i\hbar}{2\dot{q}_j}\,\mathrm{tr}\left(\frac{\partial \mathsf{R}_0}{\partial q_i}\left[\mathsf{R}_0,\mathsf{R}_1^j\right]\right), \tag{2.21}$$

where $\mathsf{R}_1 = \sum_j \mathsf{R}_1^j$ and R_1^j is the first time-odd response of the system with respect to the collective coordinate q_j. Instead of evaluating the trace directly, it is convenient to eliminate the unknown time-odd density R_1, which can be related to $\dot{\mathsf{R}}_0$ through the *linear response matrix* $\mathbb{L}$ of the system: a matrix in the space of two-quasiparticle excitations, closely related to the one appearing in the random phase approximation (RPA), which encodes how the density responds to a perturbation. Then, it can be shown that the collective inertia takes the compact form [3]:

$$M_{ij} = \frac{\partial \mathsf{R}_0}{\partial q_i}\,\mathbb{L}^{-1}\,\frac{\partial \mathsf{R}_0}{\partial q_j}. \tag{2.22}$$

This expression reflects how the collective inertia is indeed governed by the linear response of the system to a change in the collective coordinates.

Evaluating (2.22) requires inverting $\mathbb{L}$, whose dimension is set by the number of two-quasiparticle excitations and is therefore very large. In practice, two separate simplifications are made. The first is the *cranking approximation*, in which $\mathbb{L}$ is replaced by a diagonal matrix whose elements are the two-quasiparticle excitation energies E_μ and E_ν, which neglects the residual quasiparticle interaction. The second concerns the evaluation of the derivatives of R_0, which can be obtained from linear response theory, making use of $\mathbb{L}^{-1}$ once again. These assumptions lead to the *perturbative cranking* formula [3, 15]:

$$M_{ij}^{\mathrm{crank,p}} = \hbar^2 \left[\mathsf{M}^{(-1)}\right]^{-1} \mathsf{M}^{(-3)} \left[\mathsf{M}^{(-1)}\right]^{-1}, \tag{2.23}$$

written in terms of the energy-weighted moments:

$$(\mathsf{M}^{(-n)})_{ij} = \sum_{\mu<\nu} \frac{\langle\Phi|\hat{Q}_i^\dagger|\mu\nu\rangle\,\langle\mu\nu|\hat{Q}_j|\Phi\rangle}{(E_\mu + E_\nu)^n}, \tag{2.24}$$

where $\hat{Q}_i$ is the one-body operator being constrained to q_i as in (2.9), $|\Phi\rangle$ is the quasiparticle vacuum at the point $\mathbf{q}$ and $\big|\mu\nu\big\rangle = \beta_\mu^\dagger\beta_\nu^\dagger|\Phi\rangle$ a two-quasiparticle excitation built on it. Each pair of quasiparticles contributes to the inertia according to how strongly the collective operator connects it to the vacuum, weighted by inverse powers of its excitation energy. The collective inertias used in this work are of this type [2].

The collective inertia emerging from ATDHFB is a different tensor than the one from GCM, with the former being more reliable since it contains the effect of collective momenta [3, 18]. However, ATDHFB does not provide any zero-point correction in contrast to GCM, since such corrections have a quantum-mechanical origin that has no equivalent in the classical dynamics that the ATDHFB theory relies on [18].

2.3 Tunneling and the fission path

We have mentioned the existence of a collective Schrödinger equation, which can be solved, given a potential energy barrier and a collective inertia tensor. This equation might be, in general, time-dependent.

In the previous section, we discussed how time-dependent approaches provide a natural framework to describe fission, since in a decay process such as this one the transition from the ground state to a two-fragment final state has a non-zero probability. Strictly speaking, the ground state of a fissioning nucleus is therefore not a stationary state but a metastable (resonance) state, since there exist open channels through which the nucleus can decay [3].

However, in spontaneous fission, the decay proceeds through classically-forbidden regions, that is regions where the potential is higher than the energy of the system. Therefore, this probability, measured by a transmission coefficient, is exponentially small. The evolution towards the open channels is consequently extremely slow compared to nuclear timescales, and therefore, it is an excellent approximation to treat the ground state as quasi-stationary.

In this case, the probability of transition (and the corresponding half-life) is related to the transmission coefficient across a potential energy barrier. Such a transmission coefficient can be estimated from a time-independent perspective, and can be approximated to a well-known expression through the *Wentzel-Kramers-Brillouin* (WKB) approximation.

We will show in detail how the WKB approximation emerges from the collective Schrödinger equation in section 2.5.

But from a more general perspective, this approach provides an approximation of the wave function on the Schrödinger equation in the presence of a slowly varying potential. This refers to potentials which remain almost constant over a region of the order of the de Broglie wavelength $\lambda\!\!\!^{-} = \hbar/p$, where p is the (local) momentum. This is the case in classical systems, where the wavelength approaches zero, which implies that the WKB approximation is a semiclassical approximation [37].

This approximation is achieved by considering the wavefunction as $\sim \exp(iS(\mathbf{r})/\hbar)$, modulated by a slowly varying amplitude. In this case, by taking into account that terms of the order of $\hbar$ are small in the classical limit, an expression for the phase and the amplitude can be found. The phase satisfies a classical Hamilton-Jacobi equation, and therefore, can be identified with the *classical action*, that is, the integral of local momentum in the coordinate space.

In one dimension, the tunneling problem can be defined more clearly, and a well-known closed expression for the WKB solution can be found. These solutions are exponentially decaying in classically-forbidden regions, and oscillatory in classically-allowed regions. By matching these solutions on both sides of the *turning points*, that is, the points where the potential is equal to the energy, the transmission coefficient can be obtained.

The well-known expression for the WKB transmission coefficient at energy E for a barrier $V(q)$ with two turning points is $T_{\mathrm{WKB}} \sim \exp(-2\gamma)$, where we define the (dimensionless) action:

$$\gamma(q_1, q_2) \equiv \frac{1}{\hbar}\int_{q_1}^{q_2} |p(q)|\,\mathrm{d}q \equiv \frac{1}{\hbar}\int_{q_1}^{q_2} \sqrt{2M(q)(V(q)-E)}\,\mathrm{d}q\,, \tag{2.25}$$

where q_1 and q_2 are the turning points, $M(q)$ is the mass term on the Schrödinger equation, that for the collective Schrödinger equation is coordinate-dependent as we will see in section 2.5. The norm $|\cdot|$ means the complex absolute value, since, as we will see in section 2.5.1, the momentum is imaginary below the barrier ($V(q) > E$). As mentioned before, this transmission coefficient is exponentially suppressed by the action γ accumulated across the barrier.

Now, going back to the case of fission, the dynamics of the system is reduced to a small number of relevant collective variables, which comes from the adiabatic approximation, as discussed in

section 2.1. The use of the WKB formula is somewhat justified after this reduction to the set of collective variables. The role of the mass of the particle in the one-dimensional problem should be played by the collective inertia tensor from section 2.2.3. The potential energy barrier should be replaced by the potential energy surface values along the fission path, possibly supplemented by correlation corrections or zero-point energies as discussed in section 2.2.2.

Since the collective space $\{q_i\}$ can be multi-dimensional, the WKB action can be extended to a multi-dimensional space. This can be expressed using a parametrization along the fission path, guided by the coordinate s, as follows [21]:

$$\gamma(s_1, s_2) \equiv \frac{1}{\hbar}\int_{\mathbf{q}_1}^{\mathbf{q}_2} |\mathbf{p}(\mathbf{q})| \cdot \mathrm{d}\mathbf{q} \equiv \frac{1}{\hbar}\int_{s_1}^{s_2} \sqrt{2M(s)(V(s)-E)}\ \mathrm{d}s\,, \tag{2.26}$$

where $\mathbf{q}_1$ and $\mathbf{q}_2$ are entrance and exit turning points, $V(s) = V(\mathbf{q}(s))$ is the potential energy along the fission path and:

$$M(s) \equiv \sum_{ij} M_{ij}(\mathbf{q}(s))\frac{\mathrm{d}q_i}{\mathrm{d}s}\frac{\mathrm{d}q_j}{\mathrm{d}s}, \tag{2.27}$$

is the collective inertia along the fission path. Analogously to (2.25), we introduce the complex absolute value $|\cdot|$ to account for the imaginary part of the momentum. We will briefly motivate this expression in section 2.6.

The entrance point is usually taken as the ground state or isomer configurations at the corresponding energy E, while the exit point can be taken as either (i) a semiclassical outer turning point at the same energy or (ii) a configuration consisting of two distinct fragments [2].

In one dimension, there is no ambiguity with the definition of fission path, however, with a multi-dimensional collective space it is necessary to define more appropriately the fission path. There is not a proper quantum mechanical least action principle for this type of trajectory in contrast to a classical description, however, semi-classical arguments tend to favor trajectories that minimize the classical action. Therefore, we define the fission path as the *least action path* (LAP).

Several approaches can be used to find the LAP in practice. Grid-based methods, such as the dynamic programming method (DPM) or Dijkstra's method, which attempt to solve multi-decision optimization problems by breaking the problem down into simpler overlapping sub-problems, are traditional choices [17, 38]. A popular choice originated in molecular systems is given by the nudged elastic band method (NEB), an iterative method which consists of a sequence of discrete points or *images* connected by fictitious spring forces and driven by the perpendicular component of the action gradient [17]. The spring forces keep the images from drifting too much from each other while the gradient forces move the path closer to the LAP. This last method can achieve accuracy comparable or better to the other methods mentioned at a reduced computational cost [17].

Regarding the value of E in equation (2.26): although this is often taken as the ground-state HFB energy in the case of spontaneous fission, some calculations agree on zero-point corrections on top of this value. A common estimation of this correction can simply be taken as a phenomenological and adjustable parameter between $\sim$ 0.5–1 MeV in order to reproduce existing data [1, 39]. This choice is reasonable since the zero-point energy of a harmonic oscillator is equal to half of the corresponding phonon energy, that is $\hbar\omega/2$, and experimental values of the average quadrupole phonon energy are about $\hbar\omega \sim 1$ MeV for actinides [40].

Finally, the half-life can be written in terms of the transmission coefficient. Since the decay constant is probability of decay per unit time, then $\lambda = nT$, where n is the number of fission *attempts* per unit time and $T(E)$ is the transmission coefficient at energy E (ground-state or isomer energy, for example). As before, if we consider the ground-state approximately a harmonic oscillator well, the

assault frequency to the barrier can be estimated by the oscillator frequency $n = \omega/2\pi$. Therefore, the half-life is given by [41]:

$$t_{1/2}(E) = \frac{\ln 2}{nT(E)}. \tag{2.28}$$

If we use $\hbar\omega \approx 1$ MeV, $n \approx 10^{20.38}$ s^{-1} [41].

The spontaneous fission half-life is a key quantity computed by current theoretical approaches and compared with experimental measurements. This is very challenging since the experimental values of the half-lives cover several orders of magnitude, from $\sim 10^{-6}$ s for ^{250}No to $\sim 10^{17}$ s for ^{232}Th [1]. Spontaneous fission half-lives are also very sensitive on each of the ingredients involved due to the exponential dependence of the transmission coefficient: small variations of the potential energy, collective inertia and zero-point energy, uncertainties in the calibration of energy functionals or even the number of collective variables chosen, can change the half-life by orders of magnitude [1]. Therefore, accurate predictions of the ingredients are a difficult but crucial task.

2.4 Emergence of the collective Schrödinger equation

As mentioned in section 2.2.3, the existence of the collective Schrödinger equation in terms of collective variables was motivated in the GCM-GOA approach, and instead of describing tunneling with the WKB approximation, we are interested in using the full Schrödinger equation. This can be observed in more detail starting from a classical framework, motivated from the ATDHFB approach, where the classic kinetic energy (2.21) is the origin from which a collective inertia can be defined (2.21).

For general classical systems, the classical kinetic energy is bilinear in the velocities. Therefore, the energy of the collective nuclear motion in deformed nuclei can be expressed in the form [14, 42]:

$$\mathcal{H}_{\text{class}} = \frac{1}{2}\sum_{ij} M_{ij}(\mathbf{q})\dot{q}_i\dot{q}_j + V(\mathbf{q}), \tag{2.29}$$

where $\mathbf{q}$ denotes the set of collective coordinates, $V(\mathbf{q})$ is the collective potential and $M_{ij}(\mathbf{q})$ is, in general, a $\mathbf{q}$-dependent tensor (which is symmetric and positive-definite). This expression has a close similarity with a Hamiltonian on a curved spatial background with a *metric tensor* [43]. This tensor is, in general, not reducible to a diagonal and constant form by coordinate transformations. There is thus a need of a non-Euclidean metric in the collective space [42]. The natural volume element associated with this collective metric is:

$$\mathrm{d}\tau = \sqrt{\det \mathsf{M}(\mathbf{q})}\ \mathrm{d}\mathbf{q} \equiv D(\mathbf{q})\ \mathrm{d}\mathbf{q}\,. \tag{2.30}$$

In order to obtain a proper quantum mechanical description in the collective space, we need to quantize the collective Hamiltonian (2.29), from which we can obtain the collective Schrödinger equation.

This is not a trivial task in more general coordinate systems: if we naively replace the classical momenta by their quantum version, this does not lead to correct results [44]. The main reason is the fact that the metric needs to be consistent with the normalization of the wavefunction in this curved space. Also, this quantization is subject to operator-ordering ambiguities: the choice of how momenta and inertia operators are organized is not unique [43], and furthermore, some choices might lead to non-Hermitian Hamiltonians [45]. We analyze this in the following section.

2.4.1 Quantizing the collective Hamiltonian

First, we can identify M_{ij}, which rises naturally as the inertia tensor of GCM-GOA and ATDHFB, as a tentative metric in the collective space [21]. Indeed, it can be shown that the quantized Hamiltonian leads to a multi-dimensional Hamilton-Jacobi equation in the classical limit, where the metric can be identified with this mass/inertia tensor [42].

The quantized Hamiltonian takes the form:

$$\hat{H}_{\text{coll}} = -\frac{\hbar^2}{2}\frac{1}{D(\mathbf{q})}\sum_{ij}\frac{\partial}{\partial q_i}D(\mathbf{q})\,B_{ij}(\mathbf{q})\frac{\partial}{\partial q_j} + V(\mathbf{q}), \tag{2.31}$$

where $B_{ij} = (\mathsf{B})_{ij} \equiv (\mathsf{M}^{-1})_{ij}$. The kinetic operator takes the form of a Laplace-Beltrami operator, which is the natural generalization of the Laplacian to curved spaces. This operator is Hermitian and invariant under coordinate transformations, and leads to the correct classical limit [21, 42, 43].

A rather simple and natural motivation for this expression is shown in the original work of E. Schrödinger, where he introduced his homonymous equation, and we will explain next. This Hamiltonian is derived from a variational principle, constrained to normalization in the collective space under the metric [46].

The proposed quantized energy functional takes a homogeneous quadratic form of $1, p_1, p_2 \ldots$ (and their conjugates) and replaces $1 \longrightarrow \psi$ and $p_i \longrightarrow -i\hbar\partial_i\psi$:

$$\mathcal{H}[\psi] = \int\left(\frac{\hbar^2}{2}\sum_{ij}B_{ij}(\mathbf{q})\frac{\partial\psi^*}{\partial q_i}\frac{\partial\psi}{\partial q_j} + V(\mathbf{q})\left|\psi\right|^2\right)D(\mathbf{q})\;\mathrm{d}\mathbf{q}\,, \tag{2.32}$$

which we extremize under the following normalization constraint in the collective space:

$$\int\left|\psi\right|^2 D(\mathbf{q})\;\mathrm{d}\mathbf{q} = 1. \tag{2.33}$$

This condition is enforced by introducing a Lagrange multiplier:

$$\delta\left(\mathcal{H}[\psi] - E\int\left|\psi\right|^2 D(\mathbf{q})\;\mathrm{d}\mathbf{q}\right) = 0, \tag{2.34}$$

where E is a Lagrange multiplier that can be identified with the energy eigenvalue. Since ψ is complex, we vary ψ and ψ^* independently. Varying with respect to ψ^*, we find:

$$0 = \int\left(\frac{\hbar^2}{2}\sum_{ij}B_{ij}\frac{\partial(\delta\psi^*)}{\partial q_i}\frac{\partial\psi}{\partial q_j} + (V-E)\delta\psi^*\psi\right)D\;\mathrm{d}\mathbf{q}\,. \tag{2.35}$$

The first term contains a derivative acting on $\delta\psi^*$. Integrating it by parts gives:

$$\int\sum_{ij}B_{ij}\frac{\partial(\delta\psi^*)}{\partial q_i}\frac{\partial\psi}{\partial q_j}D\;\mathrm{d}\mathbf{q} = \oint\delta\psi^*\sum_{ij}DB_{ij}\frac{\partial\psi}{\partial q_j}\;\mathrm{d}S_i - \int\delta\psi^*\sum_{ij}\frac{\partial}{\partial q_i}\left(DB_{ij}\frac{\partial\psi}{\partial q_j}\right)\mathrm{d}\mathbf{q}\,. \tag{2.36}$$

Since the variation of the wavefunction vanishes at the boundary of the collective domain, the surface term is zero. Therefore:

$$0 = \int \delta\psi^* \left(-\frac{\hbar^2}{2} \sum_{ij} \frac{\partial}{\partial q_i} \left(D B_{ij} \frac{\partial \psi}{\partial q_j} \right) + D(V - E)\psi \right) \mathrm{d}\mathbf{q} \,. \tag{2.37}$$

Since $\delta\psi^*$ is arbitrary, the expression in parentheses vanishes, and the collective Schrödinger equation is obtained:

$$-\frac{\hbar^2}{2} \frac{1}{D(\mathbf{q})} \sum_{ij} \frac{\partial}{\partial q_i} \left(D(\mathbf{q}) B_{ij}(\mathbf{q}) \frac{\partial \psi}{\partial q_j} \right) + V(\mathbf{q})\psi(\mathbf{q}) = E\psi(\mathbf{q}). \tag{2.38}$$

The variation with respect to ψ gives the same result as (2.38) if V, D and B_{ij} are real and $B_{ij} = B_{ji}$.

Finally, in the one-dimensional case, the collective Hamiltonian reduces to:

$$-\frac{\hbar^2}{2} \frac{1}{\sqrt{M(q)}} \frac{\mathrm{d}}{\mathrm{d}q} \left(\frac{1}{\sqrt{M(q)}} \frac{\mathrm{d}\psi}{\mathrm{d}q} \right) + V(q)\psi(q) = E\psi(q). \tag{2.39}$$

2.5 The WKB approximation for the collective Schrödinger equation

As introduced in section 2.3, tunneling across a fission barrier is often described through a semi-classical approach with the WKB approximation [2, 3, 17], which simplifies the computation of transmission coefficients and half lives.

Its use is motivated by the large number of degrees of freedom in the nuclear many-body system, which make the extension of tunneling beyond the usual one-dimensional problem non-trivial. The adiabatic approximation, together with the WKB formula, becomes reasonably justified after reducing the dynamics to a small number of relevant collective variables [3]. Also, in spontaneous fission the barriers are typically high and wide, which further supports the use of the WKB approximation [17].

In this section, we are interested in using the WKB approximation for the collective Schrödinger equation in detail. We derive the expression for the transmission coefficient in the one-dimensional case (2.25), verifying the well-known expression for $\mathbf{q}$-dependent inertia [22].

We start from the collective Schrödinger equation written in the multidimensional collective space (2.38), multiplying by D and moving the term of the right-hand side to the left:

$$-\frac{\hbar^2}{2} \sum_{ij} \frac{\partial}{\partial q_i} \left(D B_{ij}(\mathbf{q}) \frac{\partial}{\partial q_j} \right) \psi(\mathbf{q}) + D(V(\mathbf{q}) - E)\psi(\mathbf{q}) = 0. \tag{2.40}$$

To extract the semiclassical limit, we use the WKB ansatz $\psi(\mathbf{q}) = A(\mathbf{q}) \exp(iS(\mathbf{q})/\hbar)$. Here $S(\mathbf{q})$ is related to the classical action (notice the units of angular momentum) and $A(\mathbf{q})$ is a slowly varying amplitude. Its first derivative is:

$$\frac{\partial \psi}{\partial q_j} = \left(\frac{\partial A}{\partial q_j} + \frac{iA}{\hbar} \frac{\partial S}{\partial q_j} \right) e^{iS/\hbar}. \tag{2.41}$$

Substituting this expression into the derivative term of (2.40), we obtain:

$$\frac{\partial}{\partial q_i} \left(D B_{ij} \frac{\partial \psi}{\partial q_j} \right) = \frac{\partial}{\partial q_i} \left(D B_{ij} \frac{\partial A}{\partial q_j} e^{iS/\hbar} \right) + \frac{i}{\hbar} \frac{\partial}{\partial q_i} \left(D B_{ij} A \frac{\partial S}{\partial q_j} e^{iS/\hbar} \right), \tag{2.42}$$

We now expand each contribution separately. The first term gives:

$$\frac{\partial}{\partial q_i}\left(DB_{ij}\frac{\partial A}{\partial q_j}e^{iS/\hbar}\right)=\left[\frac{\partial}{\partial q_i}\left(DB_{ij}\frac{\partial A}{\partial q_j}\right)+\frac{i}{\hbar}DB_{ij}\frac{\partial A}{\partial q_j}\frac{\partial S}{\partial q_i}\right]e^{iS/\hbar}, \tag{2.43}$$

while the second term gives:

$$\frac{\partial}{\partial q_i}\left(DB_{ij}A\frac{\partial S}{\partial q_j}e^{iS/\hbar}\right)=\left[\frac{\partial}{\partial q_i}\left(DB_{ij}A\right)\frac{\partial S}{\partial q_j}+DB_{ij}A\left(\frac{\partial^2 S}{\partial q_i\partial q_j}+\frac{i}{\hbar}\frac{\partial S}{\partial q_i}\frac{\partial S}{\partial q_j}\right)\right]e^{iS/\hbar}. \tag{2.44}$$

After substituting these expressions into the Schrödinger equation, we can order the terms according to their powers of $\hbar$. The leading real part resembles the *Hamilton-Jacobi equation* [42, 47], while the next-order imaginary part gives the transport equation for the WKB amplitude:

$$-\frac{\hbar^2}{2}\sum_{ij}\frac{-1}{\hbar^2}DB_{ij}\frac{\partial S}{\partial q_i}\frac{\partial S}{\partial q_j}Ae^{-iS/\hbar}+V(\mathbf{q})DAe^{-iS/\hbar}=EDAe^{-iS/\hbar}, \tag{2.45}$$

$$\sum_{ij}\left[\frac{\partial}{\partial q_i}\left(DB_{ij}\right)A^2\frac{\partial S}{\partial q_j}+DB_{ij}A\left(\frac{\partial A}{\partial q_i}\frac{\partial S}{\partial q_j}+\frac{\partial A}{\partial q_j}\frac{\partial S}{\partial q_i}\right)+DB_{ij}A^2\frac{\partial^2 S}{\partial q_i\partial q_j}\right]e^{-iS/\hbar}=0. \tag{2.46}$$

where in the first equation we have neglected the term $O(\hbar^2)$, which depended on the second derivatives of A (assumed to be small in the WKB approximation). In the second equation, we multiplied it by A. Dividing by the common factors, the two equations become:

$$\frac{1}{2}\sum_{ij}B_{ij}\frac{\partial S}{\partial q_i}\frac{\partial S}{\partial q_j}+V(\mathbf{q})=E, \tag{2.47}$$

$$\sum_{ij}\left[\frac{\partial}{\partial q_i}\left(DB_{ij}\frac{\partial S}{\partial q_j}\right)A^2+DB_{ij}A\left(\frac{\partial A}{\partial q_i}\frac{\partial S}{\partial q_j}+\frac{\partial A}{\partial q_j}\frac{\partial S}{\partial q_i}\right)\right]=0. \tag{2.48}$$

Now we can more explicitly observe that the first equation takes the form of the Hamilton-Jacobi equation, from which the WKB phase S is identified as the classical action. Given S from the first equation, the second equation determines the amplitude A.

2.5.1 The WKB transmission coefficient: the one-dimensional case

We now specialize the previous expressions to a one-dimensional collective path. In this case, the tensors $\mathsf{M}(\mathbf{q})$ and $\mathsf{B}(\mathbf{q})$ are replaced by $M(q)$ and $M^{-1}(q)$, respectively. Therefore, from (2.48):

$$\frac{\mathrm{d}}{\mathrm{d}q}\left(DM^{-1}\frac{\mathrm{d}S}{\mathrm{d}q}\right)A^2+2DM^{-1}A\frac{\mathrm{d}A}{\mathrm{d}q}\frac{\mathrm{d}S}{\mathrm{d}q}=\frac{\mathrm{d}}{\mathrm{d}q}\left(DM^{-1}A^2\frac{\mathrm{d}S}{\mathrm{d}q}\right)=0. \tag{2.49}$$

Now, if we define the local collective momentum as $p(q)=\sqrt{2M(q)(E-V(q))}$, and we use (2.47) and (2.49), then:

$$S(q)=\pm\int^q p(q')\,\mathrm{d}q'\,, \tag{2.50}$$

$$A(q)=\frac{C}{\sqrt{DM^{-1}(q)p(q)}}=\frac{C}{[2|E-V(q)|]^{1/4}}, \tag{2.51}$$

where we used that $D = \sqrt{M(q)}$ in the one-dimensional case and that C is a constant. Therefore, the WKB solutions along the collective coordinate can be written as right- and left-moving semiclassical waves:

$$\psi_{\pm}(q) = \frac{C_{\pm}}{[2|E - V(q)|]^{1/4}} \exp\left(\pm \frac{i}{\hbar} \int^{q} p(q')\, \mathrm{d}q'\right). \tag{2.52}$$

We now apply these solutions to tunneling through a barrier. We assume tunneling across a potential barrier $V(q)$ with an energy E below the maximum. We assume that the potential has two classical turning points at q_1 and q_2. This situation is depicted in figure (2.1).

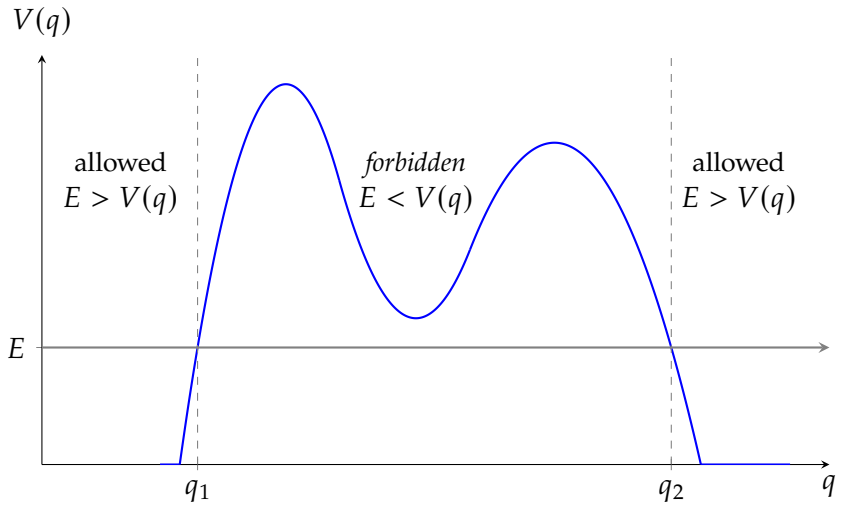

Figure 2.1: Illustration of a potential barrier $V(q)$ showing turning points and allowed/forbidden regions for WKB tunneling at energy E.

Then, the WKB wavefunction can be written with linear combinations of the solutions (2.52) with coefficients A, B, C, D, F as:

$$\psi(q < q_1) = \frac{1}{[2(E - V(q))]^{1/4}} \left[A \exp\left(-i \int_{q_1}^{q} k(q')\, \mathrm{d}q'\right) + B \exp\left(i \int_{q_1}^{q} k(q')\, \mathrm{d}q'\right)\right], \tag{2.53}$$

$$\psi(q_1 < q < q_2) = \frac{1}{[2(V(q) - E)]^{1/4}} \left[C \exp\left(-\int_{q_1}^{q} \kappa(q')\, \mathrm{d}q'\right) + D \exp\left(\int_{q_1}^{q} \kappa(q')\, \mathrm{d}q'\right)\right], \tag{2.54}$$

$$\psi(q > q_2) = \frac{F}{[2(E - V(q))]^{1/4}} \exp\left(i \int_{q_2}^{q} k(q')\, \mathrm{d}q'\right), \tag{2.55}$$

where:

$$k(q) = \frac{\sqrt{2M(q)(E - V(q))}}{\hbar}, \qquad \kappa(q) = \frac{\sqrt{2M(q)(V(q) - E)}}{\hbar}, \tag{2.56}$$

are the local wavenumbers in the classically allowed and forbidden regions, respectively. We assumed incidence from the left only, so the reflected wave on the right of the barrier was neglected.

In this convention, the coefficient B multiplies the wave travelling from left to right before the barrier, A multiplies the reflected wave, and F multiplies the transmitted wave after the barrier.

The WKB form is not valid exactly at the turning points, since $k(q)$ and $\kappa(q)$ vanish there. To connect the solutions across each turning point, we use the asymptotic forms of the Airy functions, which are the exact solutions of the problem for a linear approximation of the potential close to each turning point. This procedure is done following [47] and we show explicitly this procedure for the variable mass case in appendix A.1.

At the first turning point, the potential is increasing, so the region on the left is classically allowed and the region on the right is classically forbidden. The wavefunction close to the turning point can be written as:

$$\psi(q \simeq q_1) = \begin{cases} \dfrac{1}{[2(E-V(q))]^{1/4}} \left[2C \sin\left(\displaystyle\int_q^{q_1} k(q')\, \mathrm{d}q' + \frac{\pi}{4} \right) + D \cos\left(\displaystyle\int_q^{q_1} k(q')\, \mathrm{d}q' + \frac{\pi}{4} \right) \right], & q \lesssim q_1, \\ \dfrac{1}{[2(V(q)-E)]^{1/4}} \left[C \exp\left(-\displaystyle\int_{q_1}^{q} \kappa(q')\, \mathrm{d}q' \right) + D \exp\left(\displaystyle\int_{q_1}^{q} \kappa(q')\, \mathrm{d}q' \right) \right], & q \gtrsim q_1. \end{cases} \tag{2.57}$$

At the second turning point, the potential is decreasing, so the region on the left is classically forbidden and the region on the right is classically allowed. The wavefunction close to the turning point is:

$$\psi(q \simeq q_2) = \begin{cases} \dfrac{1}{[2(V(q)-E)]^{1/4}} \left[C' \exp\left(-\displaystyle\int_q^{q_2} \kappa(q')\, \mathrm{d}q' \right) + D' \exp\left(\displaystyle\int_q^{q_2} \kappa(q')\, \mathrm{d}q' \right) \right], & q \lesssim q_2, \\ \dfrac{1}{[2(E-V(q))]^{1/4}} \left[2C' \sin\left(\displaystyle\int_{q_2}^{q} k(q')\, \mathrm{d}q' + \frac{\pi}{4} \right) + D' \cos\left(\displaystyle\int_{q_2}^{q} k(q')\, \mathrm{d}q' + \frac{\pi}{4} \right) \right], & q \gtrsim q_2. \end{cases} \tag{2.58}$$

To relate these expressions to the WKB travelling waves written above, we express the sine and cosine functions in terms of exponentials:

$$2\sin\left(-\phi_1 + \frac{\pi}{4}\right) = e^{i\pi/4} e^{i\phi_1} + e^{-i\pi/4} e^{-i\phi_1}, \qquad \cos\left(-\phi_1 + \frac{\pi}{4}\right) = \frac{1}{2} e^{-i\pi/4} e^{i\phi_1} + \frac{1}{2} e^{i\pi/4} e^{-i\phi_1}, \tag{2.59}$$

$$2\sin\left(\phi_2 + \frac{\pi}{4}\right) = e^{-i\pi/4} e^{i\phi_2} + e^{i\pi/4} e^{-i\phi_2}, \qquad \cos\left(\phi_2 + \frac{\pi}{4}\right) = \frac{1}{2} e^{i\pi/4} e^{i\phi_2} + \frac{1}{2} e^{-i\pi/4} e^{-i\phi_2}, \tag{2.60}$$

$$\tag{2.61}$$

where $\phi_1 = \int_{q_1}^{q} k(q')\, dq'$ and $\phi_2 = \int_{q_2}^{q} k(q')\, dq'$. Using these expressions, we can match the coefficients of the exponentials for the left turning point with (2.53) and (2.57):

$$A = e^{-i\pi/4} C + \frac{1}{2} e^{i\pi/4} D, \qquad B = e^{i\pi/4} C + \frac{1}{2} e^{-i\pi/4} D, \tag{2.62}$$

For the right turning point, the forbidden-region solution in (2.58) must first be rewritten using the integral with q_1 instead of the one with q_2. This introduces the total action across the barrier. First, we match the forbidden region with (2.54) and (2.58) as follows:

$$C e^{-\phi_1} + D e^{\phi_1} = C' e^{-\gamma} e^{\phi_1} + D' e^{\gamma} e^{-\phi_1}, \tag{2.63}$$

where $\phi_2 = \phi_1 - \gamma$ and we define a dimensionless action across the barrier as:

$$\gamma = \int_{q_1}^{q_2} \kappa(q')\, dq' = \frac{1}{\hbar} \int_{q_1}^{q_2} \sqrt{2M(q)(V(q)-E)}\, \mathrm{d}q\,. \tag{2.64}$$

Therefore, $C' = D\theta$ and $D' = C/\theta$, where $\theta = \exp(\gamma)$. With these expressions of C' and D', we match the right turning point with (2.55) and (2.58):

$$F = e^{-i\pi/4} D\theta + \frac{1}{2} e^{i\pi/4} \frac{C}{\theta}, \qquad 0 = e^{i\pi/4} D\theta + \frac{1}{2} e^{-i\pi/4} \frac{C}{\theta}, \tag{2.65}$$

where the second expression is the zero-amplitude of the reflecting solution on the right region. Substituting this relation into the first equation, we obtain that $D\theta = e^{i\pi/2} C/2\theta$ and therefore:

$$F = e^{i\pi/4} \frac{C}{\theta} = 2e^{-i\pi/4} D\theta.$$

Using this relation in the second expression of (2.62), we can express B in terms of F:

$$B = e^{i\pi/4} \theta e^{-i\pi/4} F + \frac{1}{2} e^{-i\pi/4} e^{i\pi/4} \frac{F}{2\theta} = \left(\theta + \frac{1}{4\theta}\right) F. \tag{2.66}$$

The transmission coefficient can be calculated from the coefficients of the incident and transmitted waves as usual. We give a non-trivial derivation of the transmission coefficient for a variable-mass Schrödinger equation in the appendix A.2. Since B is the incident amplitude and F is the transmitted amplitude, the WKB transmission coefficient is:

$$T = \frac{|F|^2}{|B|^2} = \frac{1}{\left(\theta + \frac{1}{4\theta}\right)^2} \approx \exp(-2\gamma) = \exp\left(-\frac{2}{\hbar} \int_{q_1}^{q_2} \sqrt{2M(q)(V(q) - E)}\, dq'\right), \tag{2.67}$$

where the latter well-known expression is valid for $\gamma \gg 1$, applicable to thick barriers and low energies (such as the ones of spontaneous fission) [22].

An alternative expression for this transmission coefficient is given by Kemble's formula:

$$T = \frac{1}{1 + \exp(2\gamma)}, \tag{2.68}$$

which reduces to the previous expression for $\gamma \gg 1$. This formula improves the result for small γ, i.e., for energies closer to the top of the barrier [48]. Also, it can be shown that the Kemble formula provides the exact result for the transmission coefficient of an inverted parabolic barrier (with constant inertia) [49].

It is important to remark that this result applies only when the energy lies below the barrier everywhere, $E < V(q)$ for all q between the turning points, as figure (2.1) shows. This is usually the case for spontaneous fission. When the energy rises above the floor of an intermediate well, that region becomes classically allowed and the single-integral formula is no longer defined there; a more careful treatment combines the transmission across each peak with the phase accumulated across the well, reproducing the class-II resonances of section 3.2.2 [13]. This is more rigorous but remains restricted to a limited range of energies, and cumbersome to generalize to several wells. For the irregular barriers of the large-scale calculations over thousands of nuclei in chapter 4, we are instead interested in the simplicity of formula (2.68) and in testing its performance even outside its strict range of validity.

2.6 Extending the WKB formula to the multi-dimensional case

Obtaining such result for the WKB transmission coefficient for a multi-dimensional collective space starting from equations (2.48) and (2.47) is not trivial.

However, we can follow the idea of the action of a path across a barrier, in the spirit of the one-dimensional case (2.64). In section 2.3, we already introduced the extension of the WKB action to a multi-dimensional collective space, shown in equation (2.26).

As mentioned in section 2.3, we assume that the fission path is a least action path: a classical trajectory $\mathbf{q} = \mathbf{q}(t)$ in the collective space which satisfies Hamilton's equations and minimizes the action (2.26). We consider that this trajectory crosses a hypersurface enclosing a region of classically forbidden points $V(\mathbf{q}) > E$, which we assume convex for simplicity, at two points $\mathbf{q}_1$ and $\mathbf{q}_2$: the multi-dimensional analogs of the turning points of the one-dimensional case.

In this classical framework, using (2.29), the momentum conjugate to q_i is given by:

$$p_i = \frac{\partial \mathcal{E}_{\text{kin}}}{\partial \dot{q}_i} = \frac{\partial}{\partial \dot{q}_i}\left(\frac{1}{2}\sum_{jk} M_{jk}(\mathbf{q})\dot{q}_j\dot{q}_k\right) = \sum_j M_{ij}\dot{q}_j, \tag{2.69}$$

where we assumed that M is symmetric. The action is generalized as a line integral of the momentum along the fission path connecting the two turning points. If we introduce the parametrization $\mathbf{q} = \mathbf{q}(s)$, where s is the path length along the trajectory, the WKB action can be written as:

$$\gamma(s_1, s_2) \equiv \frac{1}{\hbar}\int_{\mathbf{q}_1}^{\mathbf{q}_2} |\mathbf{p}(\mathbf{q})| \cdot \mathrm{d}\mathbf{q} = \frac{1}{\hbar}\int_{s_1}^{s_2} |\mathbf{p}| \cdot \frac{\mathrm{d}\mathbf{q}}{\mathrm{d}s}\, \mathrm{d}s\,, \tag{2.70}$$

where, as mentioned before, the absolute value $|\cdot|$ is used to account for the imaginary part of the momentum, which is the case when $V(\mathbf{q}) > E$. From (2.69) we have that:

$$\mathbf{p} \cdot \frac{\mathrm{d}\mathbf{q}}{\mathrm{d}s} = \sum_{ij} M_{ij}\frac{\mathrm{d}q_i}{\mathrm{d}s}\dot{q}_j = \sum_{ij} M_{ij}(\mathbf{q})\frac{\mathrm{d}q_i}{\mathrm{d}s}\frac{\mathrm{d}q_j}{\mathrm{d}s}\,\dot{s} \equiv M(s)\,\dot{s}, \tag{2.71}$$

where we defined $M(s)$ as the collective inertia along the fission path (2.27). On the other hand, since in a conservative system $\mathcal{H}_{\text{class}} = E$, from (2.29) we have that:

$$\mathbf{p} \cdot \frac{\mathrm{d}\mathbf{q}}{\mathrm{d}s}\,\dot{s} = \sum_i p_i\dot{q}_i = \sum_{ij} M_{ij}(\mathbf{q})\,\dot{q}_i\dot{q}_j = 2\mathcal{E}_{\text{kin}} = 2\big(E - V(\mathbf{q})\big). \tag{2.72}$$

Multiplying (2.71) by $\dot{s}$ and equating with (2.72), we obtain:

$$\dot{s} = \sqrt{\frac{2(E - V(\mathbf{q}))}{M(s)}}. \tag{2.73}$$

Introducing (2.73) in (2.71), and using this in (2.70), we finally obtain the multi-dimensional WKB action along the fission path:

$$\gamma(s_1, s_2) = \frac{1}{\hbar}\int_{s_1}^{s_2} \left|\sqrt{2M(s)\,(E - V(\mathbf{q}))}\right| \mathrm{d}s\,. \tag{2.74}$$

Since the region of interest is the classically forbidden region, where $V(\mathbf{q}) > E$, we have $|E - V(\mathbf{q})| = V(\mathbf{q}) - E$, and the previously shown expression (2.26) is recovered.

This derivation has a subtle point: it manipulates a classical trajectory across a region where no real classical trajectory exists, which is precisely the regime where a quantum description is required. The path integral formulation of tunneling of [50] offers a useful perspective on this point, at least for the one-dimensional case with constant inertia: there, the WKB transmission coefficient is obtained from the Feynman propagator built on the classical Hamiltonian, and the

absence of real classical paths is resolved by allowing the propagation time to take complex values, so that the trajectory crosses the barrier in imaginary time, evolving classically in the inverted potential.

However, these approaches do not start from the collective Schrödinger equation, as we did for the one-dimensional case. We can instead try to obtain this result from the multi-dimensional collective Schrödinger equation by reducing it approximately to a one-dimensional equation along the fission path coordinate. The one-dimensional results of section 2.5 could, in principle, yield the transmission coefficient directly.

Following the spirit of the *reaction path* Hamiltonian of [51], developed for chemical reactions in molecular systems, we describe the dynamics in terms of the position along the fission path $\mathbf{q}(s)$ and small displacements orthogonal to it. Points in a neighborhood of the path are described by the coordinates $(s, u_1, \ldots, u_{n-1})$ through:

$$\mathbf{q}(s,u) = \mathbf{q}(s) + \sum_\alpha u_\alpha \mathbf{e}_\alpha(s), \tag{2.75}$$

where the transverse directions $\mathbf{e}_\alpha(s)$ are chosen orthogonal to the path in the sense of the inner product defined by the inertia tensor:

$$\langle \mathbf{a}, \mathbf{b} \rangle_M \equiv \sum_{ij} M_{ij}(\mathbf{q}) a_i b_j, \tag{2.76}$$

where $\mathbf{a}$, $\mathbf{b}$ are vectors in collective space.

The components of the metric in the coordinates $(s, \mathbf{u})$ follow from the kinetic energy. The collective velocity for a trajectory in the collective space is:

$$\dot{\mathbf{q}} = \frac{\partial \mathbf{q}}{\partial s}\,\dot{s} + \sum_\alpha \frac{\partial \mathbf{q}}{\partial u_\alpha}\,\dot{u}_\alpha, \tag{2.77}$$

with the coordinate basis vectors given by:

$$\frac{\partial \mathbf{q}}{\partial s} = \frac{\mathrm{d}\mathbf{q}}{\mathrm{d}s} + \sum_\alpha u_\alpha \frac{\mathrm{d}\mathbf{e}_\alpha}{\mathrm{d}s}, \qquad \frac{\partial \mathbf{q}}{\partial u_\alpha} = \mathbf{e}_\alpha(s). \tag{2.78}$$

Inserting (2.77) into the kinetic energy of (2.29) we obtain:

$$2\mathcal{E}_{\mathrm{kin}} = \langle \dot{\mathbf{q}}, \dot{\mathbf{q}} \rangle_M = \left\langle \frac{\partial \mathbf{q}}{\partial s}, \frac{\partial \mathbf{q}}{\partial s} \right\rangle_M \dot{s}^2 + 2\sum_\alpha \left\langle \frac{\partial \mathbf{q}}{\partial s}, \frac{\partial \mathbf{q}}{\partial u_\alpha} \right\rangle_M \dot{s}\,\dot{u}_\alpha + \sum_{\alpha\beta} \left\langle \frac{\partial \mathbf{q}}{\partial u_\alpha}, \frac{\partial \mathbf{q}}{\partial u_\beta} \right\rangle_M \dot{u}_\alpha \dot{u}_\beta. \tag{2.79}$$

The coefficients of the previous quadratic form are, by definition, the components of the metric in the new coordinates: the inner products of the coordinate basis vectors (2.78). Evaluated in the neighborhood of the path, where $u_\alpha \approx 0$ and therefore $\partial\mathbf{q}/\partial s = \mathrm{d}\mathbf{q}/\mathrm{d}s$, they are:

$$M_{ss} = \left\langle \frac{\mathrm{d}\mathbf{q}}{\mathrm{d}s}, \frac{\mathrm{d}\mathbf{q}}{\mathrm{d}s} \right\rangle_M = M(s), \qquad M_{s\alpha} = \left\langle \frac{\mathrm{d}\mathbf{q}}{\mathrm{d}s}, \mathbf{e}_\alpha \right\rangle_M = 0, \qquad M_{\alpha\beta} = \langle \mathbf{e}_\alpha, \mathbf{e}_\beta \rangle_M, \tag{2.80}$$

where we identify the inertia along the fission path $M(s)$ introduced in (2.27), and we used the orthogonality of the transverse directions $\mathbf{e}_\alpha$ with respect to the path. The metric is therefore block-diagonal, and its inverse $\mathsf{B} = \mathsf{M}^{-1}$ and determinant $D(\mathbf{q}) = \sqrt{\det \mathsf{M}(\mathbf{q})}$ factorize:

$$B_{ss} = \frac{1}{M(s)}, \qquad B_{\alpha\beta} = (\mathsf{M}_{\mathrm{tr}}^{-1})_{\alpha\beta}, \qquad D(\mathbf{q}) = \sqrt{M(s)}D_{\mathrm{tr}}, \qquad D_{\mathrm{tr}} \equiv \sqrt{\det \mathsf{M}_{\mathrm{tr}}}, \tag{2.81}$$

where we defined $(\mathsf{M}_{\mathrm{tr}})_{\alpha\beta} = M_{\alpha\beta}$ as the transverse metric and D_{tr} as the determinant of the transverse metric.

The kinetic operator in (2.31), in a Laplace-Beltrami form, which retains the same form under any change of coordinates, can now be rewritten in the new coordinates $(s, \mathbf{u})$ as:

$$-\frac{\hbar^2}{2}\frac{1}{D(\mathbf{q})}\sum_{ij}\frac{\partial}{\partial q_i}D(\mathbf{q})B_{ij}(\mathbf{q})\frac{\partial}{\partial q_j} = -\frac{\hbar^2}{2}\frac{1}{D(\mathbf{q})}\left(\frac{\partial}{\partial s}D(\mathbf{q})B_{ss}\frac{\partial}{\partial s} + \sum_{\alpha\beta}\frac{\partial}{\partial u_\alpha}D(\mathbf{q})B_{\alpha\beta}\frac{\partial}{\partial u_\beta}\right) \tag{2.82}$$

where the crossed terms vanish due to the block-diagonal form of the metric. The potential energy is also expressed in the new coordinates as $V(\mathbf{q}) = V(s, \mathbf{u})$.

Let us check the first term of (2.82). This term is similar to the kinetic part in (2.39), but with $D(s) = \sqrt{M(s)}D_{\mathrm{tr}}(s)$ instead of $D(q) = \sqrt{M(q)}$. In section 2.5, we noticed that $D(\mathbf{q})$ only contributes to the amplitude of the WKB solution (at order $\hbar$); see equation (2.48). By the arguments of appendix A.2, the amplitude does not affect the transmission coefficient. Therefore, if D_{tr} varies slowly along the path, we can neglect its contribution to the longitudinal kinetic operator.

On the other hand, let us consider the second term of (2.82). We first isolate the part of the equation acting on the transverse coordinates alone. Define, at each fixed s, the transverse Hamiltonian:

$$\hat{H}_\perp \equiv -\frac{\hbar^2}{2}\frac{1}{D_{\mathrm{tr}}}\sum_{\alpha\beta}\frac{\partial}{\partial u_\alpha}\left(D_{\mathrm{tr}}B_{\alpha\beta}\frac{\partial}{\partial u_\beta}\right) + V(s, \mathbf{u}) - V(s), \tag{2.83}$$

where we defined the potential along the path as $V(s) \equiv V(s, 0)$. This Hamiltonian contains the transverse kinetic operator and the potential relative to its value on the path. Its eigenvalue problem at fixed s,

$$\hat{H}_\perp \chi_m(\mathbf{u}; s) = \epsilon_m(s)\,\chi_m(\mathbf{u}; s), \qquad \int \chi_m \chi_{m'}\, \mathrm{d}^{n-1}\mathbf{u} = \delta_{mm'}, \tag{2.84}$$

defines the transverse eigenstates.

If the potential rises away from the path, $\hat{H}_\perp$ describes a potential well in the transverse directions, and its lowest eigenvalue $\epsilon_0(s) > 0$ is the zero-point energy of transverse confinement at position s. This holds exactly for the reaction path Hamiltonian of [51], whose path follows the bottom of the potential valley, where $\partial_{\mathbf{u}} V = 0$. However, the least action path used here departs in general from the valley bottom, so the transverse well is displaced from the path. The eigenvalue problem remains well defined, but interpreting $\epsilon_0(s)$ as a zero-point energy is then an approximation to first order in this displacement.

Now, we can split the wave function into a longitudinal part $\phi(s)$, which will carry the tunneling, and the transverse part $\chi_0(\mathbf{u}; s)$ which takes into account the spread of the wave function in the transverse directions, not far from the path. For simplicity, we assume that the transverse part is the lowest eigenstate of the transverse Hamiltonian at each s[2]. Therefore:

[2]We could consider a superposition with more excited transverse states χ_m. However, notice that the corresponding longitudinal wave function tunnels through an effective barrier which is higher by ϵ_m, which are exponentially more suppressed. Therefore, considering only the lowest transverse state χ_0 is reasonable, at first approximation.

$$\psi(s, \mathbf{u}) = \phi(s)\chi_0(\mathbf{u}; s). \tag{2.85}$$

We now insert this wave function into the Hamiltonian:

$$\hat{H}_{\text{coll}} = -\frac{\hbar^2}{2}\frac{1}{\sqrt{M(s)}}\frac{\partial}{\partial s}\left(\frac{1}{\sqrt{M(s)}}\frac{\partial}{\partial s}\right) + V(s) + \hat{H}_{\perp}. \tag{2.86}$$

First, the action of the transverse part of $\hat{H}_{\text{coll}}$ on the wave function is straightforward due to the eigenvalue equation of the transverse Hamiltonian (2.84):

$$\hat{H}_{\perp}\psi(s, \mathbf{u}) = \phi(s)\hat{H}_{\perp}(s)\chi_0(\mathbf{u}; s) = \epsilon_0(s)\phi(s)\chi_0(\mathbf{u}; s) = \epsilon_0(s)\psi(s, \mathbf{u}). \tag{2.87}$$

Regarding the longitudinal part of the kinetic operator, we can expand the derivatives and obtain:

$$-\frac{\hbar^2}{2}\frac{1}{\sqrt{M}}\frac{\partial}{\partial s}\left(\frac{1}{\sqrt{M}}\frac{\partial}{\partial s}\psi(s, \mathbf{u})\right) = -\frac{\hbar^2}{2}\frac{\chi_0}{\sqrt{M}}\frac{\mathrm{d}}{\mathrm{d}s}\left(\frac{\phi'}{\sqrt{M}}\right) - \frac{\hbar^2}{2M}\left(2\phi'\frac{\partial\chi_0}{\partial s} - \frac{M'}{2M}\phi\frac{\partial\chi_0}{\partial s} + \phi\frac{\partial^2\chi_0}{\partial s^2}\right). \tag{2.88}$$

We can now eliminate the transverse coordinates in the Hamiltonian by projecting the equation onto the transverse ground state: multiplying by χ_0 and integrating over the transverse coordinates. The terms containing $\partial_s\chi_0$ vanish due to:

$$\int \chi_0 \frac{\partial\chi_0}{\partial s}\,\mathrm{d}^{n-1}\mathbf{u} = \frac{1}{2}\frac{\mathrm{d}}{\mathrm{d}s}\int \chi_0^2\,\mathrm{d}^{n-1}\mathbf{u} = 0, \tag{2.89}$$

where we have used the normalization (2.84). However, the term containing $\partial_s^2\chi_0$ does not vanish, and we define:

$$\eta(s) \equiv -\int \chi_0\frac{\partial^2\chi_0}{\partial s^2}\,\mathrm{d}^{n-1}\mathbf{u} = \int\left(\frac{\partial\chi_0}{\partial s}\right)^2\mathrm{d}^{n-1}\mathbf{u} \geq 0, \tag{2.90}$$

where we applied ∂_s to (2.89) to obtain the second equality.

Therefore, by collecting (2.86), (2.88) and (2.87), we obtain the following one-dimensional equation for $\phi(s)$:

$$-\frac{\hbar^2}{2}\frac{1}{\sqrt{M(s)}}\frac{\mathrm{d}}{\mathrm{d}s}\left(\frac{1}{\sqrt{M(s)}}\frac{\mathrm{d}\phi}{\mathrm{d}s}\right) + \left(V(s) + \epsilon_0(s) + \frac{\hbar^2}{2M(s)}\eta(s)\right)\phi(s) = E\,\phi(s). \tag{2.91}$$

However, the term with $\eta(s)$ is of order $\hbar^2$, and can be neglected in the WKB approximation; see equation (2.47): this expression is of order 1, and the potential enters only in this expression, so this term can be dropped. Therefore, we obtain the final one-dimensional equation for $\phi(s)$:

$$-\frac{\hbar^2}{2}\frac{1}{\sqrt{M(s)}}\frac{\mathrm{d}}{\mathrm{d}s}\left(\frac{1}{\sqrt{M(s)}}\frac{\mathrm{d}\phi}{\mathrm{d}s}\right) + V_{\text{eff}}(s)\,\phi(s) = E\,\phi(s), \tag{2.92}$$

where we define an effective potential along the fission path as $V_{\text{eff}}(s) = V(s) + \epsilon_0(s)$. This expression coincides with the one-dimensional collective Schrödinger equation (2.39) under the path coordinate s. A consequence of this reduction is that the transverse degrees of freedom enter the longitudinal problem only through the effective potential $V_{\text{eff}}(s)$, which is shifted by the transverse zero-point energy $\epsilon_0(s)$, at least at first approximation in the vicinity of the fission path.

Since we obtained a one-dimensional collective Schrödinger equation in the path coordinate, the WKB treatment of section 2.5 applies without modification in principle. Therefore, the WKB transmission coefficient is given by (2.68), with the action along the fission path γ given by (2.26) but with the effective potential $V_{\text{eff}}(s)$.

There is an additional subtlety regarding the energy E of the initial decaying state. This state is localized in a potential well, and its energy must be computed from (2.92). If $\epsilon_0(s)$ varies slowly around the well minimum, the effective potential is shifted there by the constant $\epsilon_0(s_{\text{well}})$, and the energy eigenvalue E will be shifted as well by $\epsilon_0(s_{\text{well}})$. This is, $E = \tilde{E} + \epsilon_0(s_{\text{well}})$, where $\tilde{E}$ is the corresponding eigenvalue of the reduced equation with the bare potential $V(s)$ alone. This is relevant when considering the energy in the WKB action (2.26).

This section is an attempt to show how a one-dimensional Schrödinger equation along the fission path can be obtained from the multi-dimensional collective Schrödinger equation, but it should be regarded as a first approximation. The well-known WKB result can be recovered from this reduction, but the number of assumptions it requires reflects how non-trivial the extension of the WKB formula to a multi-dimensional collective space is.

Key assumptions such as the wave function being concentrated in the vicinity of the fission path and the transverse degrees of freedom being in their lowest state are all approximations that may not hold in more complex scenarios. The separation of the longitudinal and transverse degrees of freedom in the metric may fail away from the fission path, and coupling between these degrees of freedom can become significant. The definition of $\epsilon_0(s)$ as a zero-point energy is only meaningful where the potential forms a well in the transverse directions.

A further point that this reduction overlooks is the treatment of the boundary conditions: the equation (2.92) is defined only along the fission path, while the matching of section 2.5 formally requires incoming and outgoing waves beyond its endpoints. Since the transmission coefficient is determined by the barrier region between the turning points, this is not expected to affect the result at the present level of approximation.

Finally, a similar idea of a path-transverse separation of the equation has been developed more rigorously in [52], for example. That work uses a two-dimensional Hamiltonian, where the potential on the transverse coordinate is approximated by a harmonic potential. The Hamiltonian can then be decomposed in a path component and a remainder, where in the former, a zero-point energy of such potential is added to the potential along the fission path. In this case, a one-dimensional barrier penetration problem is found, and the remainder is treated in the distorted wave Born approximation (DWBA).

Chapter 3

Solving the collective Schrödinger equation

In chapter 2, we derived the collective Schrödinger equation and the WKB approximation for the transmission coefficient. The latter provides, in principle, a simple and reliable strategy for the calculation of spontaneous fission half-lives. We restrict ourselves to the one-dimensional Schrödinger equation. This equation requires as inputs the fission path, that is, the potential barrier $V(q)$ and the collective inertia $M(q)$ along the single collective coordinate q. Solving the equation numerically we can obtain the transmission coefficient $T(E)$ and, through it, the spontaneous fission half-life $t_{1/2}^{\mathrm{SF}}$.

While the WKB formula is exact for a parabola [49], noticeable deviations from the exact solution appear for realistic barriers, and especially for multi-humped barriers, where additional effects appear that the WKB approximation cannot reproduce, as we will see. Solving the collective Schrödinger equation exactly removes these limitations and provides the reference against which the WKB error can be quantified.

The main objective of this chapter is to present the numerical methods used to solve the collective Schrödinger equation, and to investigate where the WKB approximation deviates from the exact solution and quantify the resulting error in the calculated $t_{1/2}^{\mathrm{SF}}$. The chapter is organized in two parts. In section 3.1, we describe the numerical procedure: the propagation schemes, the boundary conditions and extraction of the transmission coefficient, and the practical treatment of the fission-path data from microscopic calculations. In section 3.2, we test the resulting workflow against analytically solvable barriers and double-humped barriers with known qualitative features. Along the way, we assess the accuracy of the WKB approximation and the sensitivity of the half-life to the numerical treatment.

3.1 Numerical solution of the collective Schrödinger equation

Our starting point is the collective Schrödinger equation (2.38), which differs from the usual Schrödinger equation because of the position dependence of the inertia. Moreover, tunneling across a barrier is not an eigenvalue problem but a scattering-type problem, so the energy E is a fixed input. The equation is integrated across the barrier and matched to asymptotic plane waves, in regions where the potential is taken to vanish.

We discuss the main ingredients of the numerical procedure used in this work in the following sections: the propagation scheme used to integrate the equation (section 3.1.1), the boundary

conditions and the extraction of the transmission coefficient from the asymptotic amplitudes (section 3.1.2), and the practical treatment of the fission-path data coming from external microscopic calculations (section 3.1.3).

3.1.1 Finite difference methods

The usual methods to solve the Schrödinger equation numerically are based on finite-difference schemes, which propagate the wavefunction across the barrier. In this work we implement and compare three well-known methods: *Runge-Kutta integration* [53], the *Numerov method* [54] and the *Johnson logarithmic-derivative method* [55].

The implementation of the standard Runge-Kutta method is straightforward, making use of the built-in `SciPy` package in Python (`solve_ivp` function, more specifically). More specifically, we use the explicit RK5(4) method [53]; in this method, the error is controlled assuming accuracy of the 4th-order method, but the steps are taken using the 5th-order accurate formula. The following system of first-order differential equations is solved:

$$\psi' = \sqrt{M(q)}\,\eta, \qquad\qquad \eta' = 2\sqrt{M(q)}\,(V(q) - E)\,\psi, \tag{3.1}$$

where $\eta = \psi'/\sqrt{M(q)}$. Taking values of relative and absolute tolerances[1] of `solve_ivp` equal to $r_{\text{tol}} = 10^{-6}$ and $a_{\text{tol}} = 10^{-9}$, respectively, is more than enough for the purposes of this work.

The advantages of this method are its generality and ease of implementation, applying to a wide range of problems with no restriction on the form of the equation. In particular, and unlike the other two methods, it does not require the derivatives of $M(q)$, which for noisy data can be a source of instability. However, in classically forbidden regions the propagation can be unstable: exponentially decaying and growing solutions coexist, so any roundoff error could contaminate the growing component, which is then amplified exponentially along the barrier.

We discuss the boundary conditions and the definition of the transmission coefficient in detail in the next section, but we can already anticipate that, especially at low energies, the transmission coefficient becomes very small and the usual definition $T = 1 - |S|^2$ can be unreliable due to catastrophic cancellation ($|S| \to 1$, with the difference falling below machine precision). A more stable alternative for this method is to compute the transmission coefficient from the transmitted amplitude instead, as we explain in section 3.1.2.

On the other hand, the Numerov method [54] is a three-point recursion scheme for equations of the form $\psi'' + Q(q)\psi = 0$, with local error $O(h^6)$ (h being the step size), which is very efficient and accurate for the Schrödinger equation. In order to transform the collective Schrödinger equation (2.39) into this form, we apply the change of variable $\phi \equiv M(q)^{-1/4}\psi$, which removes the first-derivative term, obtaining

$$\phi'' + \tilde{Q}(q)\phi = 0, \tag{3.2}$$

where it can be shown that:

$$\tilde{Q}(q) \equiv Q(q) + \frac{1}{4}\frac{M''(q)}{M(q)} - \frac{5}{16}\left(\frac{M'(q)}{M(q)}\right)^2, \qquad\qquad Q(q) \equiv \frac{2M(q)}{\hbar^2}(E - V(q)). \tag{3.3}$$

[1] More precisely, at each step the solver bounds the estimated local error by $a_{\text{tol}} + r_{\text{tol}}\,|y|$, where $|y|$ is the magnitude of the propagated solution (here: ψ and η). The term r_{tol} controls a relative accuracy (number of correct significant digits), while a_{tol} controls an absolute accuracy (number of correct decimal places) [56]. If the RK estimated error exceeds this bound the step is rejected and retried with a smaller size; otherwise it is accepted.

With equation (3.2) in mind, the recursion scheme reads [54]:

$$\phi_{n+1} = \frac{2\left(1 - \frac{5}{12}h^2\tilde{Q}_n\right)\phi_n - \left(1 + \frac{1}{12}h^2\tilde{Q}_{n-1}\right)\phi_{n-1}}{1 + \frac{1}{12}h^2\tilde{Q}_{n+1}}, \tag{3.4}$$

where we denote the value of a function $f = f(q)$ evaluated at the n-th grid point as $f_n \equiv f(q_n)$.

Since this scheme is tailored to the Schrödinger equation, it is very fast (one function evaluation per grid point, in contrast to the RK substeps). However, it requires the first and second derivatives of $M(q)$, and it suffers from the same low-energy instability of T as the Runge–Kutta method. In addition, it does not provide automatic error control, so convergence must be checked by hand.

We can take a different approach by propagating the logarithmic derivative of the wavefunction instead of the wavefunction itself. This is a standard technique in scattering calculations, and it has the advantage of removing the exponential-growth instability, since the logarithmic derivative remains $O(1)$ in the classically forbidden region while ψ grows exponentially. The Johnson method [55] propagates the logarithmic derivative $u = \psi'/\psi$; for the usual Schrödinger equation, this turns the second-order equation into a first-order Riccati equation $u' + u^2 + Q(q) = 0$. For the collective Schrödinger equation (2.39), an additional change of variable, $v \equiv u - M'(q)/4M(q)$, is required to bring the equation to Riccati form, which leads to

$$v' + v^2 + \tilde{Q}(q) = 0, \tag{3.5}$$

where $\tilde{Q}(q)$ is the same as in (3.3). The Johnson recursion scheme therefore reads [55]

$$\frac{1}{1 - hv_{n+1} - \frac{1}{3}h^2\tilde{Q}_{n+1}} + \frac{1}{1 + hv_{n-1} - \frac{1}{3}h^2\tilde{Q}_{n-1}} = 2\,\frac{1 - \frac{1}{2}h^2\tilde{Q}_n}{1 + \frac{1}{6}h^2\tilde{Q}_n}. \tag{3.6}$$

Besides removing the exponential-growth instability, this method is as fast as Numerov. However, it does not provide the wavefunction itself, which is a drawback: the direct transmission coefficient T_d, computed from the transmitted amplitude (section 3.1.2), is therefore not accessible with this method. Only T can be obtained, but, in contrast to the other two methods, it remains stable at low energies because the logarithmic derivative is well-behaved there. The method also requires the first and second derivatives of $M(q)$, and it does not provide automatic error control. Finally, care must be taken with the step placement, since $u(q)$ has poles at the nodes of ψ.

Although we analyze and compare the performance of these three methods in section 3.2, we can already anticipate that the built-in RK method is the simplest and most reliable of the three, and is sufficient for our purposes; it is the main one we use for the subsequent calculations of the half-lives.

3.1.2 Boundary conditions and transmission coefficient

The numerical solution of the collective Schrödinger equation for this scattering-like problem requires the definition of boundary conditions. The simplest approach is to assume *plane-wave asymptotics*, which greatly simplifies the calculation of the transmission coefficient. However, this assumption requires that the potential and inertia become constant outside the barrier region. In practice, this is achieved by truncating the physical potential and padding it with flat regions[2].

[2]Without this truncation, the plane waves are not solutions of the asymptotic equation, so the simplified extraction of the transmission coefficient from the amplitudes S and A does not apply. The transmission coefficient itself remains well defined; it is this particular approach to computing it that relies on free asymptotic states.

As we will see in section 3.2, the truncation of the potential is itself a source of deviation from the WKB result, since WKB involves only the region where $V(q) \geq E$, while Schrödinger is sensitive to the entire potential. On the inner side, the truncation is a common assumption in calculations of fission half-lives [22, 52] and it is reasonable: the ground-state well provides a genuine floor, so the potential naturally flattens there rather than being cut off by hand.

With this assumption in mind, we consider the wavefunction in the asymptotic regions as a superposition of plane waves. Without loss of generality (the 1D problem is direction-invariant), the plane waves travel from large q to small q and take the form [57]

$$\psi(q) \approx \begin{cases} e^{-ik_{\mathrm{R}}q} - S\, e^{+ik_{\mathrm{R}}q}, & q > q_{\max}, \\ A\, e^{-ik_{\mathrm{L}}q}, & q < q_{\min}, \end{cases} \tag{3.7}$$

where A is the transmitted amplitude and S the reflected one. The asymptotic wavenumbers are

$$k_i = \frac{\sqrt{2\,M_i\,(E - V_i)}}{\hbar}, \qquad i = \mathrm{L}, \mathrm{R}, \tag{3.8}$$

with V_i and M_i the (constant) potential and inertia in the left and right asymptotic regions, respectively.

To solve for A and S, we start with imposing a unit transmitted wave, that is, $\psi_{\mathrm{start}} = e^{-ik_{\mathrm{L}}q_{\mathrm{start}}}$ and $\psi'_{\mathrm{start}} = -ik_{\mathrm{L}}\, e^{-ik_{\mathrm{L}}q_{\mathrm{start}}}$. We then propagate the solution numerically from the left asymptotic region towards the incident side and finally the numerical solution is matched to the incident-side asymptotic form of (3.7) at a point $q = q_{\mathrm{m}}$.

Because the equation is linear, the propagated solution equals the true one up to an overall constant: fixing the transmitted amplitude to 1 instead of A rescales the whole wavefunction by $1/A$. The incident-side asymptotic form of (3.7), multiplied by this same factor, must therefore match the propagated ψ at q_{m} as follows:

$$\psi(q_{\mathrm{m}}) = \frac{1}{A}(e^{-ik_{\mathrm{R}}q_{\mathrm{m}}} - S\, e^{+ik_{\mathrm{R}}q_{\mathrm{m}}}), \qquad \psi'(q_{\mathrm{m}}) = \frac{1}{A}(-ik_{\mathrm{R}}\, e^{-ik_{\mathrm{R}}q_{\mathrm{m}}} - ik_{\mathrm{R}}\, S\, e^{+ik_{\mathrm{R}}q_{\mathrm{m}}}). \tag{3.9}$$

These two equations form a linear system for the unknowns $1/A$ and S/A, which is solved by:

$$\frac{1}{A} = \frac{ik_{\mathrm{R}}\,\psi_{\mathrm{m}} - \psi'_{\mathrm{m}}}{2ik_{\mathrm{R}}}\, e^{+ik_{\mathrm{R}}q_{\mathrm{m}}}, \qquad \frac{S}{A} = -\frac{ik_{\mathrm{R}}\,\psi_{\mathrm{m}} + \psi'_{\mathrm{m}}}{2ik_{\mathrm{R}}}\, e^{-ik_{\mathrm{R}}q_{\mathrm{m}}}, \tag{3.10}$$

where $\psi_{\mathrm{m}} \equiv \psi(q_{\mathrm{m}})$ and $\psi'_{\mathrm{m}} \equiv \psi'(q_{\mathrm{m}})$. The values of ψ_{m} and $\psi'_{\mathrm{m}} = \sqrt{M_{\mathrm{R}}}\,\eta_{\mathrm{m}}$ are obtained directly from the numerical solution of the system of ODEs (3.1) from the RK5(4) method described previously[3].

The S and A amplitudes provide two separate ways to compute the transmission coefficient, which should be equivalent in the absence of absorption[4]. The first is the flux-based definition $T =$

[3] For the Numerov method, ψ'_{m} is instead estimated from the propagated wavefunction with a fourth-order central finite-difference approximation. The logarithmic-derivative method does not provide ψ_{m} and ψ'_{m} separately, but directly their ratio $u_{\mathrm{m}} = \psi'_{\mathrm{m}}/\psi_{\mathrm{m}}$; the reflection amplitude then follows from $S = (u_{\mathrm{m}} + ik_{\mathrm{R}})/(u_{\mathrm{m}} - ik_{\mathrm{R}})\, e^{-2ik_{\mathrm{R}}q_{\mathrm{m}}}$. As we mentioned in the previous section, since only the ratio is available, the transmitted amplitude A cannot be recovered, and this method yields $T = 1 - |S|^2$ but not T_{d}.

[4] Indeed, we checked this numerically on the parabolic barrier of section 3.2.1, computing T with the logarithmic-derivative method and T_{d} with the RK5(4) method: over a range of energies spanning from deep tunneling to well above the barrier top, the relative difference between the two stays at the 10^{-4}–10^{-7} level, of the order of the tolerances used in the integration.

$1-|S|^2$, which is the unitarity deficit of reflection. The second is the direct definition $T_\mathrm{d} = |A|^2$, which is the square of the transmitted amplitude. The transmission amplitude A follows immediately as the reciprocal of the first quantity in (3.10), and the reflection amplitude S as the ratio of the second to the first.

As anticipated in section 3.1.1, $1 - |S|^2$ suffers catastrophic cancellation deep below the barrier, precisely where spontaneous fission occurs: T becomes unreliable once $T \lesssim 10^{-12}$ and floors at $\sim 10^{-16}$ (machine precision). In contrast, T_d stays well-conditioned for very small values of the transmission coefficient, so we use T_d at all energies instead[5].

When a complex potential is involved, flux is absorbed, $T \neq T_\mathrm{d}$ and we can define the absorption as $T_\mathrm{abs} = T - T_\mathrm{d}$. In section 3.2.3 we test the influence of absorption.

If the potential in the asymptotic regions are not equal, the direct transmission coefficient T_d, which is the ratio of transmitted to incident flux, requires a correction factor to account for the different asymptotic wavenumbers. Following the derivation of appendix A.2, we can analogously calculate the flux of a plane wave $\mathcal{A}_i\, e^{\pm ikq}$ in a region $i = \mathrm{L}, \mathrm{R}$ with constant potential V_i and inertia M_i, which gives:

$$J_i = \pm \frac{p_i}{\sqrt{M_i}} |\mathcal{A}_i|^2 = \pm \sqrt{2\,(E - V_i)}\, |\mathcal{A}_i|^2, \tag{3.11}$$

since $p_i = \hbar k_i = \sqrt{2M_i(E - V_i)}$. Then, the corrected direct transmission coefficient is:

$$T_\mathrm{d} = \frac{J_\mathrm{L}}{J_\mathrm{R}} = \sqrt{\frac{E - V_\mathrm{L}}{E - V_\mathrm{R}}}\, |A|^2, \tag{3.12}$$

where we considered that the incident plane wave has unit amplitude and $\mathcal{A}_\mathrm{L} = A$. For simplicity, we take the assumption of a common floor $V_\mathrm{L} = V_\mathrm{R}$, and $T_\mathrm{d} = |A|^2$ holds.

Finally, we remind that the transmission coefficient is proportional to the inverse of the half-life as in (2.28). For spontaneous fission, this half-life is calculated at an energy E slightly above the ground-state energy, as discussed in section 2.3: $E = E_\mathrm{g.s.} + E_\mathrm{exc}$, where the zero-point energy E_exc is typically of the order of 0.5 MeV. We choose this value as a representative one, but we also explore the sensitivity of the half-life to this choice for analytical benchmarks in section 3.2 and the next chapter for fission paths of microscopic origin.

3.1.3 Fission paths from microscopic calculations and implementation details

Before testing the workflow on barriers with analytical results in section 3.2, one step of the numerical procedure remains to be described: the treatment of the fission-path data of microscopic origin, whose results are analyzed in the next chapter.

The input to the solver is a one-dimensional fission path extracted from the potential energy surfaces (PES) computed with the BSkG3 energy density functional in the MOCCa code [2]. The PES is defined over a collective space that is in principle *triaxial*, spanned by the quadrupole deformations β_{20}, β_{22} and the octupole deformation β_{30}. Each point carries the corresponding value of the inertia tensor evaluated in the ATDHFB framework under the cranking approximation. The fission path is constructed as the least action path (LAP) with methods of the PyNEB package [2], minimizing the WKB action, from the ground state to the exit point (being either a configuration

[5] We noticed that this cancellation seems to be unavoidable for the RK and Numerov methods and T_d is the only reliable choice at small transmission. The logarithmic-derivative method is the exception: the transmission can be rewritten as $T = -4k_\mathrm{R}\ \mathrm{Im}\, u_\mathrm{m}/(|u_\mathrm{m}|^2 + k_\mathrm{R}^2 - 2k_\mathrm{R}\ \mathrm{Im}\, u_\mathrm{m})$, in which the small result is carried by $\mathrm{Im}\, u_\mathrm{m}$ rather than by a cancelling difference, and T therefore remains stable since u_m is very stable for this method. If needed, T can be provided by this method (but as before, it cannot provide T_d at the same time).

with $E = E_{\text{g.s.}}$ or a low neck configuration prior to scission [2]). However, since we are interested only in a one-dimensional collective space, the datasets used correspond to nuclei with *axial* symmetry, that is, $\beta_{22} = 0$, a degree of freedom that is not explored by most nuclei in order to reach the global minimum of the action [58]. Therefore, only β_{20} varies along the path and β_{30} takes energy-optimal values only[6].

For a given nucleus, data of the collective potential $V(q) - E_{\text{g.s.}}$ and inertia tensor components (of which only the first diagonal element is required for the one-dimensional case) are provided for each value of the dimensionless quadrupole deformation β_{20}, which is related to the quadrupole moment q_{20} (which we use from now on) by:

$$q_{20} = \frac{3}{4\pi} A R_0^2 \beta_{20}, \qquad R_0 = 1.2 A^{1/3} \text{ fm}, \tag{3.13}$$

where A is the mass number of the nucleus. Energies are given in MeV, q_{20} is given in barns (b) and the collective inertia is expressed in $\hbar^2 \text{ MeV}^{-1} \text{ b}^{-2}$.

Because the microscopic calculation provides $V(q_{20})$ and $M(q_{20})$ only at a finite set of deformations, while the propagators require them either at arbitrary q or on a given fixed uniform grid, the tabulated data must be interpolated. We construct three piecewise cubic Hermite polynomial interpolants (PCHIP), built-in in the `SciPy` library, two for the real and imaginary parts of $V(q_{20})$ and one for $M(q_{20})$, with no extrapolation outside the potential range. PCHIP is preferred over a cubic interpolant, for example, because it is monotonicity-preserving and does not overshoot near the boundaries of the tabulated range. The sensitivity of the results to this interpolation for different types of barriers is quantified in section 3.2.4.

Outside the tabulated range, the flat asymptotic regions required by the boundary conditions of section 3.1.2 are imposed by setting $V(q_{20}) - E_{\text{g.s.}} = 0$ and holding the inertia at its value at the corresponding endpoint, $M_{\text{L}} = M(q_{\min})$ and $M_{\text{R}} = M(q_{\max})$. The matching point is placed as close as possible to the outer edge of the barrier while leaving room for the finite-difference stencils used by the fixed-step propagators. In principle it can be located anywhere in the asymptotic region, and the insensitivity of the result to this choice is verified in section 3.2.4.

Finally, the WKB transmission coefficient is evaluated from the Kemble expression (2.68), with the action integral taken over the classically forbidden region, which consists of set of points with $V(q_{20}) \geq E$. Only the real part of the potential enters the action, and the expression is applied only in the cases where the energy is below the barrier top: $E < V_{\max}$. As we mentioned at the end of section 2.5.1, formula (2.64) is strictly valid only for energies below the barrier everywhere between the turning points, but we are still interested in applying it outside its range of applicability due to its simplicity. In practice, therefore, we evaluate the WKB action (2.64) only over the classically forbidden intervals, letting the allowed ones contribute zero so that the integrand stays real. As we will see in the section (3.2.2), this implies that for energies reaching into the intermediate wells the formula cannot reproduce the behavior there, in particular the class-II resonances.

3.2 Numerical testing

We now test the numerical workflow on a series of barriers, starting with analytically solvable ones and progressing to more realistic double-humped barriers and finally to fission paths of microscopic

[6] More precisely, a two-step procedure is used in [2] to constrain the 3D collective space. First, $\beta_{30}^{\text{opt}}(\beta_{20})$ is obtained by building a 2D PES in (β_{20}, β_{30}) under axial symmetry and taking, at each β_{20}, the value of β_{30} that minimizes the energy. The second step finds the LAP in the 2D space (β_{20}, β_{22}) at fixed $\beta_{30}^{\text{opt}}(\beta_{20})$; since we take $\beta_{22} = 0$, the path reduces to the single collective coordinate β_{20}.

origin in the next chapter. The purpose is to quantify the error of the numerical scheme and its possible sources, and to observe distinctive qualitative features and behaviors on different types of barriers. We focus on: (i) how accurately the solver reproduces known analytic transmission coefficients, (ii) which qualitative and quantitative features characterize the deviation of the WKB approximation from the exact solution, (iii) how independent the result is with respect to arbitrary choices in the construction (matching point, truncation, energy choice), (iv) how sensitive the half-life is to the interpolation of the tabulated PES and inertia, and (v) which propagator is the most suitable and robust for the task.

3.2.1 Benchmarking with analytical solutions

We use three analytically solvable barriers to benchmark the numerical solution of the collective Schrödinger equation: the square barrier, the Eckart barrier, and the parabolic barrier. For these, we assume a constant inertia $M(q) = 50\ \text{MeV}^{-1}\hbar^2$ and zero potential on both boundaries; the effect of coordinate-dependence of the inertia is not tested on these analytic results.

The square barrier is one of the simplest possible barriers. Since this barrier is highly discontinuous, it constitutes a stress test for the accuracy of the propagators. It is important to keep in mind that the edges of the classically forbidden region are fixed here by the discontinuities of the potential and not by genuine turning points, since $V(q)$ never equals E. The connection formulas behind the WKB result, obtained by linearizing the potential around each turning point, therefore do not apply, and the Kemble expression (2.68) does not strictly apply for this barrier[7]. However, we can still give an estimate of this value by integrating over the whole classically forbidden region (where $V(q) \geq E$ still applies).

On the other hand, the Eckart barrier [55] is a single-humped, symmetric and smooth barrier that decays exponentially to zero at the barrier edges. Its continuity allows us to test WKB accuracy more properly, since the turning points are well-defined for a barrier such as this one.

Finally, a parabolic barrier is a case of interest since the WKB result is exact only for this parabola (with Kemble's formula for the transmission coefficient (2.68)), which is the well-known Hill-Wheeler transmission coefficient [49]. However, it is important to remember the truncation discussed in section 3.1.2 regarding the boundary conditions, which implies that the parabola used for the Schrödinger calculation differs from the *unbounded* parabola involved in the Hill-Wheeler formula. This difference is interesting because here resides one of the key deviations of our calculations from the WKB result: the transmission coefficient deviates at low energies, close to the truncation of the potential. This barrier is continuous but not smooth, since the truncation leads to corners at the edges of the barrier.

Figures (3.1), (3.2) and (3.3) show the results for the half-life $t_{1/2}(E)$ calculated from the Schrödinger calculation (from the RK5(4) method), WKB and the corresponding analytic result. The deviation of WKB from the exact result $\log_{10}(t_{1/2}^{\text{WKB}}/t_{1/2}^{\text{exact}})$ is also shown, together with the relative error of the RK5(4) method with respect to the exact value. We calculate the WKB value only on energy values lower than the barrier top, where the WKB action (2.64) is well-defined.

From these figures, we first note the expected behavior of the half-life with energy. The half-life decreases as the energy increases, which is consistent with the fact that tunneling becomes more likely with shorter barriers where to tunnel. As the energy approaches and exceeds the barrier top, the half-life flattens to an asymptotic value, again consistent with total transmission $T \to 1$ over the barrier. For the square barrier (3.1) this asymptotic region shows a characteristic oscillatory

[7] For a barrier with discontinuous edges, such as the square barrier, there exists an analogous WKB-type expression for the transmission coefficient, given by the usual $\exp(-2\gamma)$ term multiplied by an energy-dependent prefactor [37]. Since we are interested in the applicability of the specific Kemble expression (2.68), we do not consider it here.

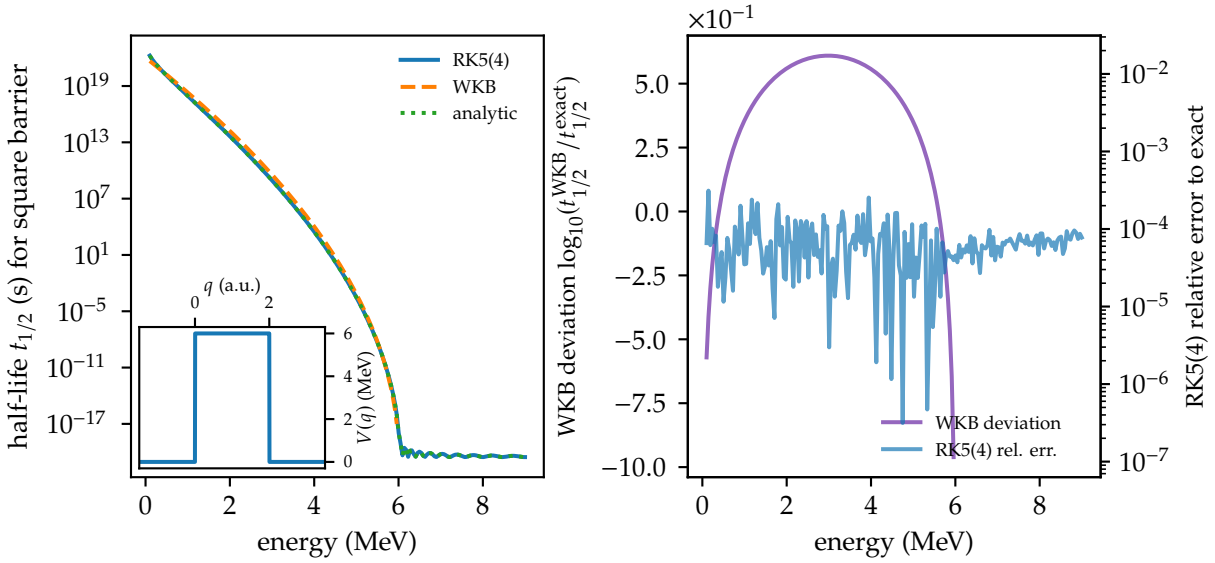

Figure 3.1: Half-life calculated for a square barrier, $V(q) = V_0$ for $0 \le q \le L$ and zero elsewhere, with $V_0 = 6$ MeV, $L = 2$ a.u. and constant inertia $M = 50\ \mathrm{MeV}^{-1}\hbar^2$. Left: half-life from the RK5(4) solution, the WKB approximation (below the barrier only) and the analytic result [59]; the inset shows the potential. Right: WKB deviation $\log_{10}(t_{1/2}^{\mathrm{WKB}}/t_{1/2}^{\mathrm{exact}})$ (left axis) and the relative error of the RK5(4) solution with respect to the analytic result (right axis). The solver uses $r_{\mathrm{tol}} = 10^{-6}$, $a_{\mathrm{tol}} = 10^{-9}$.

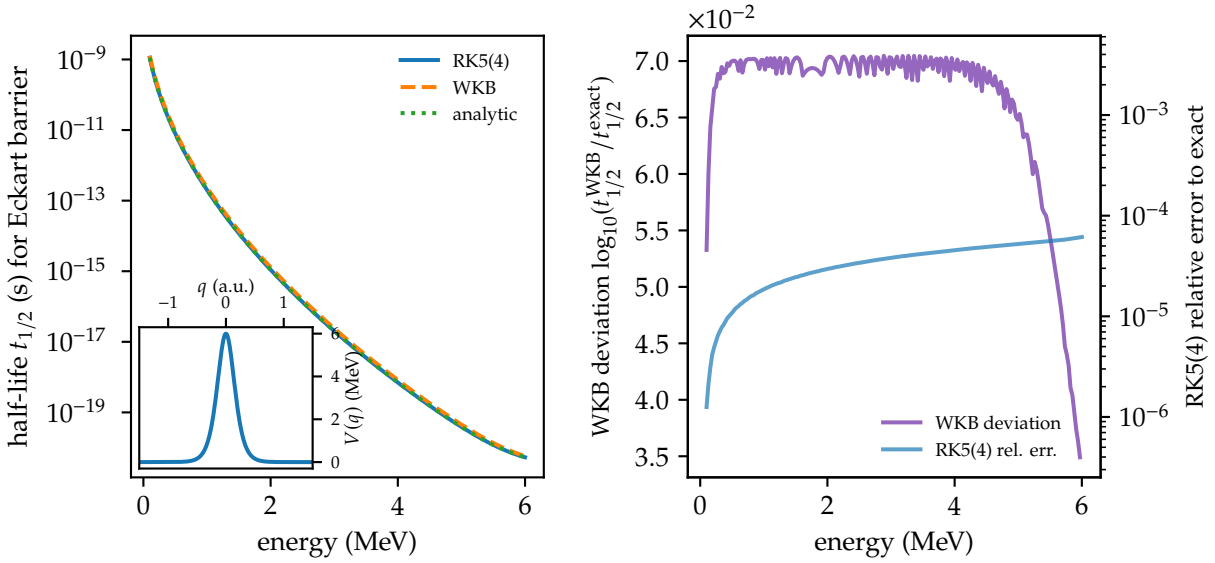

Figure 3.2: Half-life calculated for an Eckart barrier, $V(q) = V_0\, \mathrm{e}^{q/a_0}/(1 + \mathrm{e}^{q/a_0})^2$, and deviation of the WKB and calculated results with respect to the exact solution [55], analogously as before in figure (3.1). The height is $V_0/4$, with $V_0 = 24$ MeV, $a_0 = 0.1$ a.u. and $M = 50\ \mathrm{MeV}^{-1}\hbar^2$.

structure (accurately reproduced by the solver); it is of little interest here, since spontaneous fission probes the deep-tunneling regime far below the top.

It is also worth stressing how sensitive the half-life is to the energy in that sub-barrier regime: since $t_{1/2}$ depends exponentially on the action, a small change in energy shifts $t_{1/2}$ by many orders

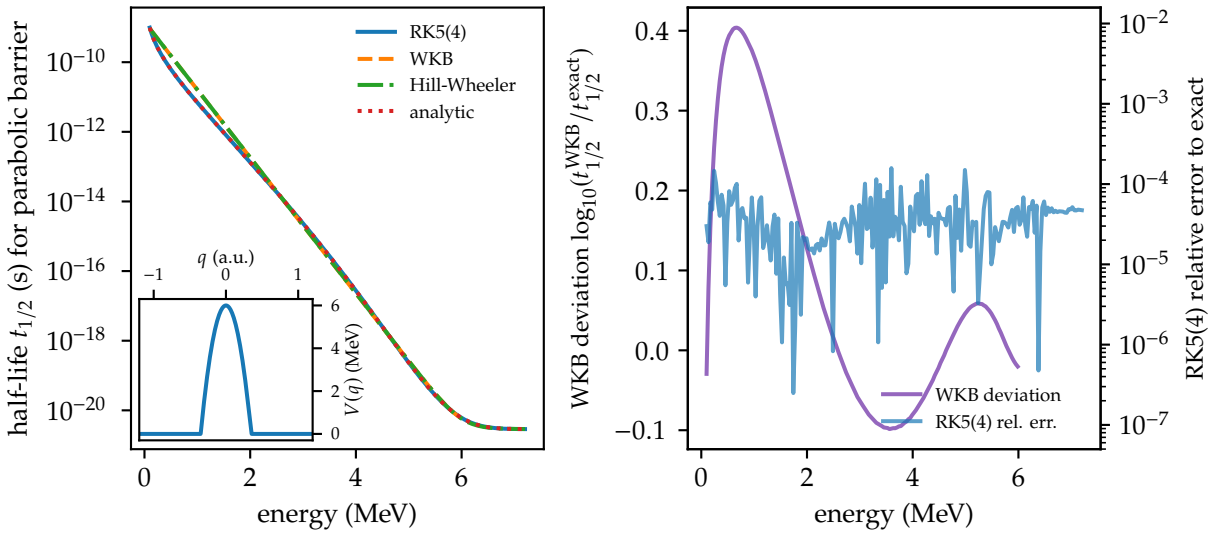

Figure 3.3: Half-life calculated for a truncated parabolic barrier, $V(q) = U_0[1 - (q/\alpha)^2]$ for $|q| \leq \alpha$ and zero elsewhere, and deviation of the WKB and calculated results with respect to the exact solution, analogously as before in figure (3.1). We use $U_0 = 6$ MeV, $\alpha = 0.35$ a.u. and $M = 50$ MeV$^{-1}\hbar^2$. The Hill-Wheeler expression [49] for an (non-truncated) parabolic barrier is shown in the left plot, in addition to the exact result of the truncated barrier [60].

of magnitude, as the left panels show. Even under this strong exponential dependence, the relative error and the WKB deviation remain stable and low across the whole range.

More precisely, the RK5(4) relative error is kept consistently between $\sim 10^{-7}$ and $\sim 10^{-4}$ across the full energy range, consistent with the imposed tolerance and largely independent of the barrier shape, which highlights the robustness of the numerical method. Even for a discontinuous barrier such as the square one, the imposed tolerance is enough to reach the exact value without issue: the error stays $\lesssim 10^{-4}$ in the worst case. Across the three benchmarks the accuracy is maintained over a remarkably wide range of half-lives, from $t_{1/2} \sim 10^{19}$ s for the square barrier down to $\sim 10^{-21}$ s for the parabolic one, which confirms that the $T_{\mathrm{d}} = |A|^2$ construction is stable enough and does not show numerical instabilities such as the ones discussed in the previous section for $T = 1 - |S|^2$ in this deep-tunneling regime.

The relative error of the non-smooth barriers (square and truncated parabola) is visibly noisier than that of the smooth Eckart barrier. This is expected: at the corners of the parabola and the discontinuity of the square barrier the solution is least regular, so the numerical error there is both larger and irregular from point to point.

We can now turn to the deviation of the WKB approximation. The three barriers behave quite differently, and together they isolate the two mechanisms that will matter for the real fission paths of the next chapter.

For the truncated parabola (3.3), the WKB half-life departs from the exact one at low energy, forming a positive ridge that peaks at ~ 0.4 orders of magnitude, below energies roughly a third of the barrier height. This deviation is smooth and clearly not numerical noise: it is the direct consequence of the truncation discussed in section 3.1.2. As discussed there, the truncation is hinted by the presence of the ground state bottom, it is needed to enforce the boundary conditions and define a transmission coefficient for the calculation. Furthermore, as shown in appendix B.1, this low-energy ridge does not disappear by a different choice of barrier features: its height stays

close to ~ 0.4 when the barrier height, width and inertia are varied over the ranges representative of the real BSkG3 barriers, so it is not an accident of a particular shape. As we will find in the next chapter, this offset is found on the microscopic fission paths as well.

The Eckart barrier (3.2) is smooth and involves no truncation, and correspondingly shows no such ridge: its WKB deviation is about ten times smaller, sitting at ~ 0.06 orders of magnitude, and is visibly noisier. This residual jaggedness hints at numerical error rather than at a genuine physical effect. The smoothness of the potential is therefore the key distinction from the parabolic case: with no corner at the barrier feet, the low-energy offset simply does not appear.

For both smooth barriers, the deviation improves as the energy approaches the barrier top. There, the barrier is locally parabolic, so Kemble's formula (2.68) is more accurate and the deviation tends to zero.

Two caveats are worth keeping in mind in this discussion. First, at very low energy the exact transmission $T_{\mathrm{d}} \to 0$ as $E \to 0$, while the WKB expression tends to a constant; the ratio therefore diverges and the deviation grows without bound as $E \to 0$. A vanishing energy is neither feasible nor physical from the Schrödinger point of view (since no plane waves would be allowed in the boundaries), which is one more reason a finite zero-point energy E_{exc} must be assumed. Second, the square barrier (3.1) shows a large WKB deviation with a qualitatively different, non-monotonic shape: this specific WKB formula is simply not well-suited to a barrier with no proper turning points. Even so, it is remarkable that the deviation stays below one order of magnitude at intermediate energies. Unlike the smooth cases, it does not improve toward the top, since the square barrier is nowhere locally parabolic.

3.2.2 Testing double-humped potentials

We can now turn to a more realistic barrier that resembles usual fission barriers, the double-humped potential, parametrized by smoothly connected parabolas [13, 57]. In contrast to the barriers of the previous section, the double-humped barrier has no closed-form of the transmission coefficient, however, we are interested in explore the qualitative physics and the ranges of deviation that emerge from introducing a second barrier.

In the intermediate range between the parabolic humps, a parabolic well is present (which represents the isomer well of the fission barrier), as previously illustrated in figure (2.1). As the previous truncated parabolic barrier, the potential is not completely smooth since corners are formed in the edges of the barrier, as we add the usual flat boundary regions. Figure (3.4) shows the half-life as a function of energy for this barrier, together with the deviation of WKB from the numerical solution. We choose humps with heights of 6 and 5 MeV, an isomeric well of height of 2 MeV, curvatures $\hbar\omega = 1.0,\ 0.8,\ 1.0$ MeV respectively, and constant inertia $M = 0.054\, A^{5/3}\ \mathrm{MeV}^{-1}\ \hbar^2$ with $A = 240$.

Figure (3.4) shows a new qualitative feature, absent from the single-humped potentials of the previous section. The exact solution develops sharp peaks that the WKB curve does not: these are resonances coming from the quasi-bound states of the isomeric well, the so-called class-II states in the literature. Away from the peaks, WKB still follows the background trend of the half-life with energy, but it has no mechanism to produce interior states and misses the resonances entirely[8];

[8] Rigorously, as mentioned at the end of section 2.5.1, the single-integral WKB formula can actually be modified to produce these resonances in a double-humped barrier, by combining the transmission across each hump with a phase accumulated across the well [13]. This phase is closely related to the quantization condition that gives the bound-state energies of the isomeric well in the WKB approximation [37]. The resonances produced by WKB are slightly shifted in energy and can differ in height from the exact result by as much as a factor of 10^{12} for a double-humped parabolic barrier [61]: even when WKB can describe these resonances, the differences in these regions can still be large. Resonances are

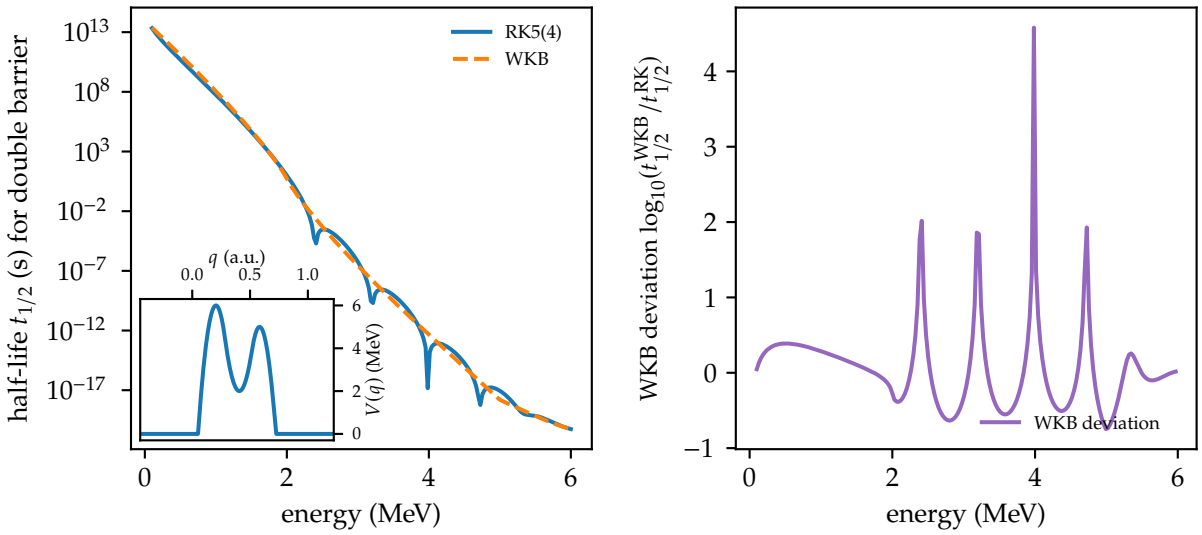

Figure 3.4: Half-life calculated for a double-humped barrier formed by the two smoothly connected parabolas from [13, 57], with barrier heights 6 and 5 MeV, an isomeric well at 2 MeV, curvatures $\hbar\omega = 1.0$, 0.8 and 1.0 MeV, and constant inertia $M = 0.054\,A^{5/3}$ MeV^{-1} $\hbar^2$ with $A = 240$. Left: half-life from the RK5(4) solution and from the WKB approximation, with the potential in the inset. Right: WKB deviation with respect to the numerical result, $\log_{10}(t_{1/2}^{\mathrm{WKB}}/t_{1/2}^{\mathrm{RK}})$.

the deviation is smooth and modest between them and spikes at each resonance energy. It is worth noting that these are not true compound-nucleus resonances nor they are related to the spectroscopy of the real nucleus; instead they originate from subsequent reflections in the inner well, returning in phase at the quasi-bound energies and amplifying the wavefunction [57].

The position of these peaks approximately follows the energy quantization of the isomeric (parabolic) well [13], $E_n = V_2 + (n + \frac{1}{2})\hbar\omega_2 \approx 2.40, 3.20, \ldots$ MeV. In appendix B.2, we compute the energy of one peak more precisely and compare it with this prediction, confirming that its origin is indeed a quasi-bound state of the isomeric well.

One caveat is worth stressing. These resonances are far narrower than a uniform energy grid on the scale of MeV can resolve, with widths of order meV, and their true peaks are also far taller than they appear on such a grid, at least 13 orders of magnitude above the background (see appendix B.2). Since the spontaneous fission half-life is evaluated at a single fixed energy, resolving these resonances is not necessary for the calculations that follow. It becomes important, however, whenever the transmission is used as an energy-dependent input, as in a Hauser-Feshbach treatment of fission cross sections [57].

Finally, at low energy, below the lowest resonance ($\approx$ 2.4 MeV), the two values differ only through the truncation effect. A mild positive deviation of $\sim$ 0.1–0.2 orders of magnitude builds up in this region, the counterpart of the low-energy ridge found for the truncated parabola. If resonances are not present at low energies, the WKB deviations are still kept lower than one order of magnitude for the double-humped barrier.

therefore not a feature missing from the WKB approximation itself, but from the simple formula (2.68). From now on, when referring to *deviation of WKB* we mean deviation from the simple WKB formula.

3.2.3 Testing complex double-humped potentials

As an additional test on the double-humped barriers of the previous section, we add an imaginary well $W(q)$ of depth E_W, with the same width as the inner parabola, and observe its effect on the transmission. Figure (3.5) shows T, T_d and T_abs as a function of energy for a given imaginary depth, together with the variation of T_d with the imaginary depth.

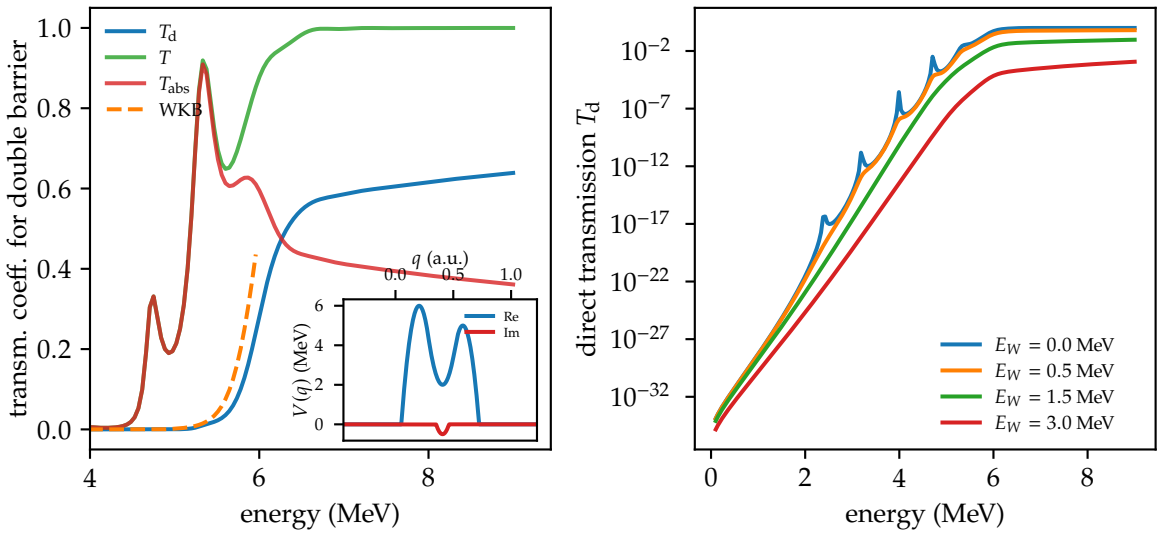

Figure 3.5: Double-humped barrier of figure (3.4) with an imaginary absorbing potential of depth E_W and the same width as the inner parabola added in the isomeric well. Left: direct transmission T_d, total transmission T and absorbed flux $T_\mathrm{abs} \equiv T - T_\mathrm{d}$ for $E_W = 0.5$ MeV, together with the WKB result obtained from the real part of the potential; the inset shows the real and imaginary parts. Right: direct transmission as a function of energy for $E_W = 0.0$, 0.5, 1.5 and 3.0 MeV.

We can visibly notice now that the two definitions of the transmission coefficient no longer coincide: $T = 1 - |S|^2$ (the total flux removed from the incident channel) and $T_\mathrm{d} = |A|^2$ (the flux that traverses directly) differ, and their difference $T_\mathrm{abs} = T - T_\mathrm{d}$ quantifies the flux absorbed, that is, trapped in the well. The left panel of figure (3.5) shows that under the barrier, absorption is dominant and tracks the class-II resonances. As the energy increases above the barrier, the direct transmission T_d dominates, increasing very slowly to reach 1 asymptotically. The WKB curve, built from the real part alone, follows approximately T_d below the barrier but does not account for absorption.

The right panel of figure (3.5) shows that the direct transmission T_d decreases at all energies by a few orders of magnitude while T_abs grows, as flux is progressively diverted from direct penetration into the well as expected. The class-II resonances are correspondingly damped and broadened until the resonant structure is washed out with increasing absorption. This is also a practical motivation for introducing the imaginary potential: as shown in appendix B.2, the undamped resonances are too narrow to be resolved on any usable energy grid, so a calculation that must deliver a smooth $T(E)$ benefits from absorption.

A physical interpretation of the addition of absorption is not straightforward, since the imaginary depth is arbitrary. However, absorption can be read as flux *trapped* in an isomeric state, which reduces the direct transmission and therefore is long-lived [57].

3.2.4 Numerical sensitivity to interpolation and propagators

Before applying the solver to the microscopic fission paths, it is important to assess how sensitive the computed half-life is to the choices made in the numerical scheme, such as the interpolation of the tabulated potential and inertia, the propagator used to integrate the equation, and the placement of the matching point where the numerical solution is joined to the asymptotic plane waves. A reliable result must be insensitive to these choices, or at least sensitive in a controlled and quantifiable way.

The fission paths of interest in this work are a restricted set of data: the potential $V(q)$ and the inertia $M(q)$ are known only at a finite set of deformation points and must be interpolated before the ODE can be integrated. The question this section addresses is how much of the final half-life $t_{1/2}^{\mathrm{SF}}$ is determined by the interpolation itself rather than by the physics of the input. We approach it first on the analytic barriers, where a true error analysis is possible: we sample the potential at N points, interpolate, solve, and compare the resulting half-life with the exact function. Figure 3.6 shows the relative error for this comparison for three barriers. This figure also shows a leave-one-out (LOO) test for each barrier: removing one point from a fixed-size set of data and comparing the resulting half-life with the full set; this test localizes sensitive areas of the data set/function where interpolation might be more ambiguous.

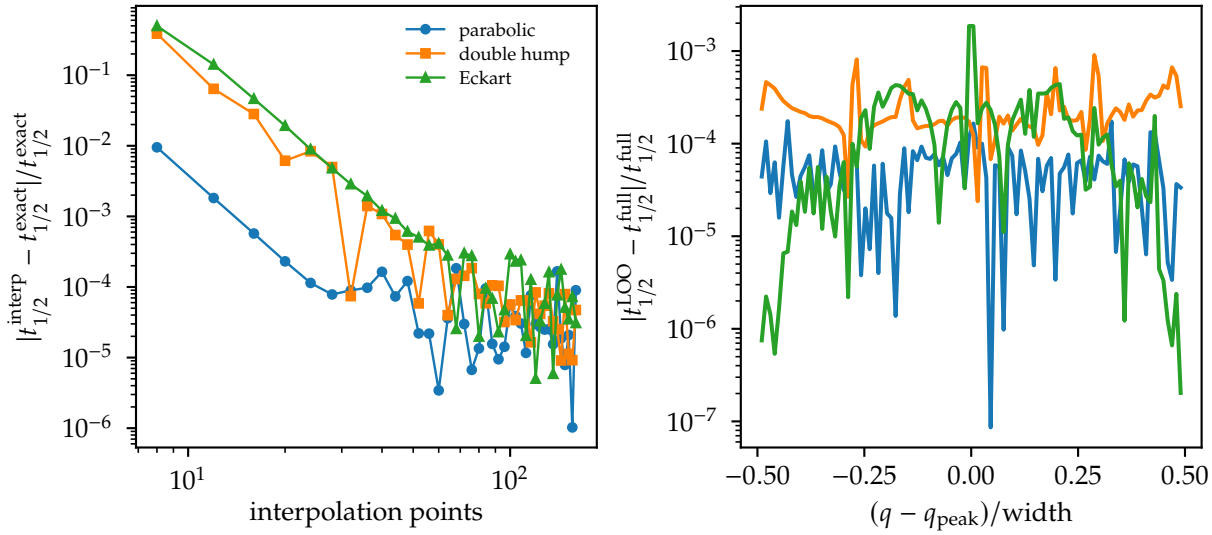

Figure 3.6: Interpolation sensitivity for the analytic barriers. Left: relative deviation of the half-life computed from an N-point PCHIP interpolant with respect to the exact result, as a function of N, for the parabolic, double-humped and Eckart barriers. Right: leave-one-out deviation with respect to the full 100-point interpolant, as a function of the position of the removed point, normalized as $(q - q_{\mathrm{peak}})/w$.

For the analytic barriers (figure (3.6), left panel), the relative deviation of the half-life from an N-point interpolant falls steeply with N up to a few tens of points, reaching the 10^{-4} level, and then flattens out: beyond that, adding more points no longer improves the result, and the residual scatter reflects the accuracy of the tolerance level of the calculation itself instead of the quality of the interpolant. The convergence is similar for all three barriers, although the parabola sits about an order of magnitude below the Eckart and double-humped curves in the initial decay: being a low-order polynomial, it is easily reconstructed by the interpolant, whereas the exponential tails of

the Eckart barrier and the two humps of the double barrier are harder to capture.

Regarding the LOO test (right panel), we can notice that the cost of removing a single point stays at the 10^{-4}–10^{-5} level or below across the whole barrier for the three cases. The parabola is again the lowest and the double-humped barrier the highest, consistent with the difficulty of reconstructing each shape. Reconstruction of the tails of Eckart is easier far away from the top, since they are asymptotic, close to a constant value, for example; closer to the top, the reconstruction is more sensitive. We can see that with a sufficiently dense set of interpolation points, no single point dominates the result, so the interpolation introduces no real ambiguity in the half-life for these barriers.

We can stress this test further with the fission paths from microscopic calculations, since interpolation performance is strongly function-dependent and very sensitive to the non-smoothness of the input. Here the exact result is not available, so we compare the half-life from a reduced set of tabulated points against the one from the full tabulated set: a self-consistency test rather than a true error analysis. Figure (3.7) shows the relative deviation of the half-life for the BSkG3 fission paths of ^{236}U, ^{286}Fl and ^{252}Cf as a function of the number of input points, together with the LOO error with respect to the full set.

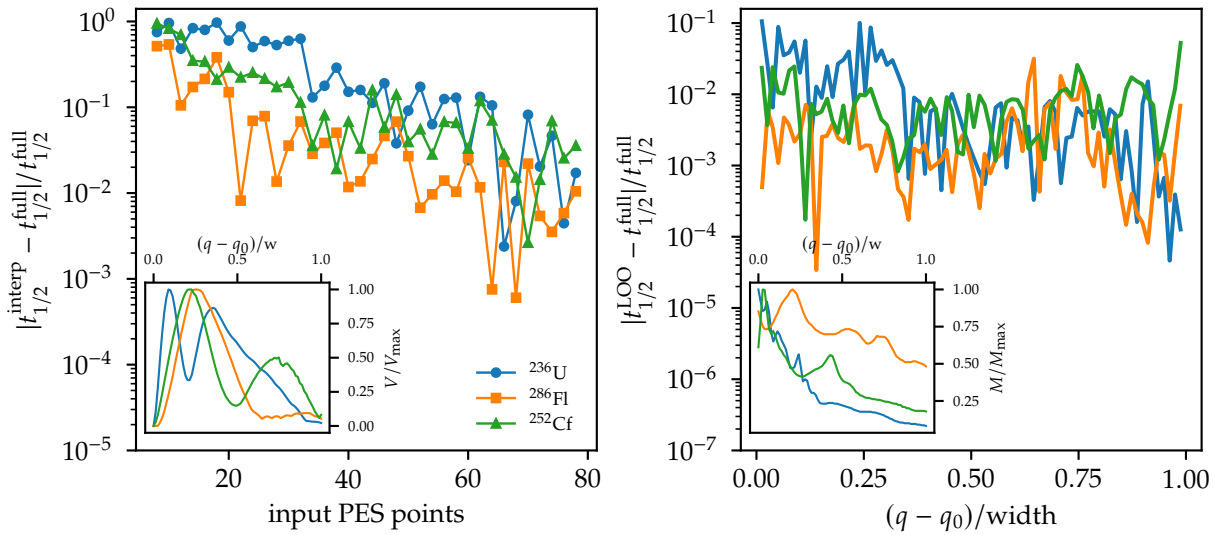

Figure 3.7: Interpolation sensitivity for the BSkG3 fission paths of ^{236}U, ^{286}Fl and ^{252}Cf. Left: relative deviation of the half-life obtained from a reduced number of input PES points with respect to the full tabulated set. Right: leave-one-out deviation as a function of the position of the removed point along the path, $(q - q_0)/w$; the insets show the corresponding normalized potential and collective inertia.

The relative deviation (figure (3.7), left panel) is still at the percent level even when points are removed only down to near-full density. Unlike the analytic barriers, the error does not decay strongly: it stays noticeable, of order 10^{-2}, against the 10^{-4}–10^{-6} reached by the analytic barriers at a comparable number of points, already with only a few points removed. Converted to half-life terms, this residual is nonetheless small: a relative error of 10^{-2} corresponds to $\Delta(\log_{10} t_{1/2}) \approx 0.434 \times 10^{-2} \sim 0.005$, negligible next to the WKB systematic studied earlier and far below the uncertainties from the fission-path inputs. The curves are also noisy and non-monotonic, so the convergence with the number of points is far less regular than in the analytic case. We note that the heavier nuclei appear to converge slightly faster than the lighter ones, consistent with their shorter

paths being more densely sampled per unit deformation.

The LOO test (right panel) shows that this sensitivity is not spread evenly along the path but concentrates at small deformation, on the ground-state side. As the insets show, the potential there is smooth while the collective inertia $M(q)$ is rough and varies rapidly, so it seems that the roughness of the inertia, not of the potential, limits the interpolation: sampling a spiky $M(q)$ is what no interpolant can reconstruct faithfully from too few points.

As mentioned in section 3.1.1, a more precise discussion of the propagator choice is offered in this section. Figure (3.8) shows the mean relative error of the half-life against runtime for RK5(4), Numerov and the logarithmic-derivative method, the error being averaged over 200 sub-barrier energies and measured against the analytic result. The relative tolerance of RK5(4) is scanned from 10^{-3} to 10^{-8} and the number of grid points of the fixed-step methods from 500 to 16000; the runtimes are the shortest of three repetitions.

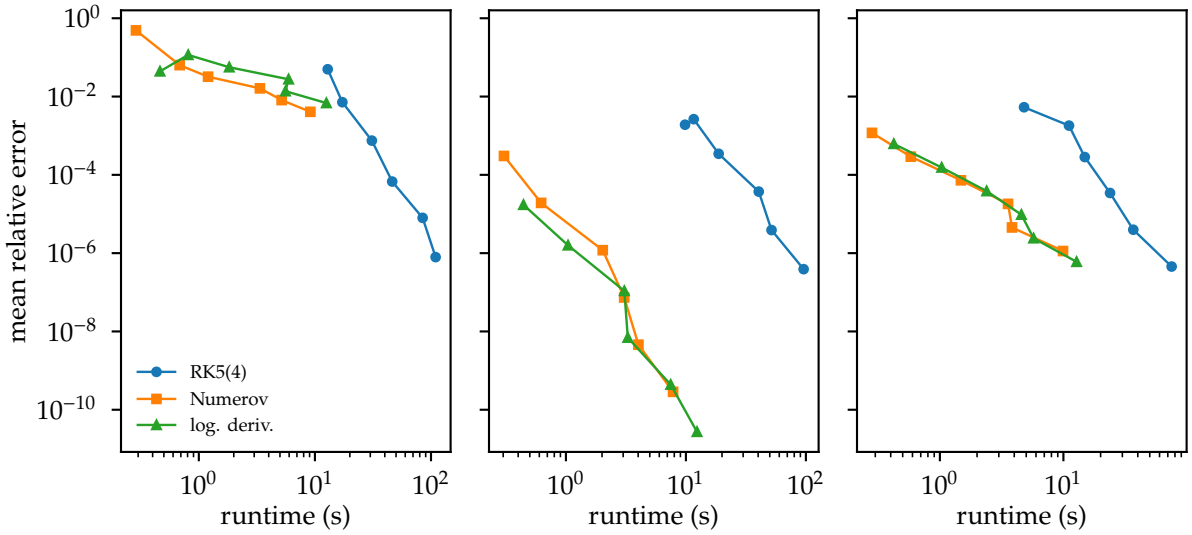

(a) square barrier (b) Eckart barrier (c) parabolic barrier

Figure 3.8: Mean relative error of the half-life against runtime for the RK5(4), Numerov and logarithmic-derivative propagators, for the (a) square, (b) Eckart and (c) parabolic barriers of figures (3.1)–(3.3). The error is averaged over 200 sub-barrier energies and measured against the analytic result. The relative tolerance of RK5(4) is varied from 10^{-3} to 10^{-8}, and the number of grid points of the fixed-step methods from 500 to 16000; runtimes are the shortest of three repetitions.

We can observe that, for these smooth barriers, the fixed-step methods are faster: at equal accuracy, Numerov and the logarithmic-derivative method are roughly an order of magnitude faster than the built-in RK5(4), since they take a single function evaluation per grid point with no adaptive steps from error control. However, this latter feature is a clear advantage of the built-in method, allowing a given tolerance to be achieved across barriers of very different shape, without any manual tuning. Notice the error on the fixed-step methods decays substantially faster on the smooth Eckart barrier compared to the discontinuous square barrier, while the built-in method provides consistent accuracy across both.

Runtime is in any case a secondary concern for our purposes. Even the slower RK5(4) runs in seconds per nucleus, a cost entirely negligible next to the microscopic calculation of the PES and the collective inertia that produce the input in the first place. Since accuracy at a mild tolerance is already more than enough, the relevant question is not speed or precision but robustness:

whether the same method can be applied blindly to thousands of barriers regardless of shape and smoothness. This is where RK5(4) is preferable. We therefore adopt RK5(4) as the standard method for the calculations of the following chapter.

Finally, we checked the sensitivity to the placement of the matching point q_{m}, where the numerical solution is joined to the asymptotic plane waves. Throughout the asymptotic region the relative variation of the direct transmission T_{d} stays below $\sim 10^{-10}$, reflecting only the integrator tolerance. Its placement within this flat region therefore does not affect the result, as required by the formulation of section 3.1.2.

A last point should be noted: the value of the zero-point energy E_{exc} at which the half-life is evaluated, also belongs to this discussion, but we treat it only briefly here. On one hand, the benchmarks already studied have made clear that the absolute half-life is extremely sensitive to this choice, since it depends exponentially on the energy through the tunneling action. On the other hand, the effect of this choice on the WKB-Schrödinger deviation is strongly barrier-dependent due to the resonance structure, and is therefore better studied on the full set of microscopic paths in the following chapter, where the statistics of thousands of nuclei is useful for this analysis.

Chapter 4

Results

In this chapter, we apply the solver developed and validated in chapter 3 to the more realistic fission barriers of microscopic origin, using several thousand realistic paths that the BSkG3 calculations provides across the nuclear chart. The object of study is the deviation of the WKB half-life from the exact solution of the collective Schrödinger equation, $\log_{10}(t_{1/2}^{\mathrm{WKB}}/t_{1/2}^{\mathrm{Schr}})$.

The analysis is organized around three aims. The first is to characterize the deviation between the two treatments, both qualitatively and quantitatively, and to establish how it is distributed across the nuclear chart. The second is to investigate the impact of this deviation compared to deviations from experiment on state-of-the-art calculations such as [2], and so to judge whether replacing the WKB approximation by the exact solution is a relevant improvement in practice. The third is to assess how strongly the deviation depends on the zero-point energy, the least constrained of the ingredients entering the calculation.

The chapter follows this order. Section 4.1 examines first the qualitative and quantitative features of the deviation for a few representative nuclei in detail. Section 4.2 extends the comparison to the whole available set of fission paths. Section 4.3 investigates correlations of the deviation on different features of the fission barriers such as the barrier height, length, A or Z, for example. Finally, section 4.4 studies the sensitivity of the deviation to the choice of zero-point energy for the whole set of fission paths.

4.1 Results for a few representative fission paths

Before analyzing the systematics over the whole chart, we focus on a few representative nuclei, in order to extract the qualitative and quantitative features of the WKB deviation on realistic barriers.

We select 3219 nuclei for which an axially symmetric least-action path can be obtained from the MOCCa code, following the procedure described in section 3.1.3. Only 129 of them have a measured spontaneous-fission half-life in NUBASE2020 [7], which gives an idea of the range of nuclei that can be treated and highlights the capability of the EDF model to go well beyond the well-measured region of the chart.

As in the previous chapter, we focus on the quantity $\log_{10}(t_{1/2}^{\mathrm{WKB}}/t_{1/2}^{\mathrm{Schr}})$, which measures the order of magnitude of the deviation of the WKB half-life from the exact one. This deviation is evaluated at a given zero-point energy $E_{\mathrm{exc}} = E - E_{\mathrm{g.s.}}$, for which we take $E_{\mathrm{exc}} = 0.5$ MeV as mentioned previously.

We choose three nuclei in order to illustrate the diversity of barrier shapes and half-lives found across the chart. First, ^{256}Fm is an actinide, accessible experimentally, with a double-humped barrier with a measured half-life of $t_{1/2} \sim 10^4$ s [7]. Second, ^{325}Fl is a very neutron-rich superheavy

far from the known nuclei, with a single, low and thin barrier; we expect it to be very short-lived, showing how susceptible this nucleus is to fission. Third, ^{245}Fr is the opposite case, with a long, high and multi-humped barrier, and we expect it to be very long-lived, far beyond any known nucleus. As with the analytic barriers of the previous chapter, we evaluate the half-life of each of them as a function of the energy, together with the corresponding WKB deviation; the results are shown in figures (4.1)–(4.3).

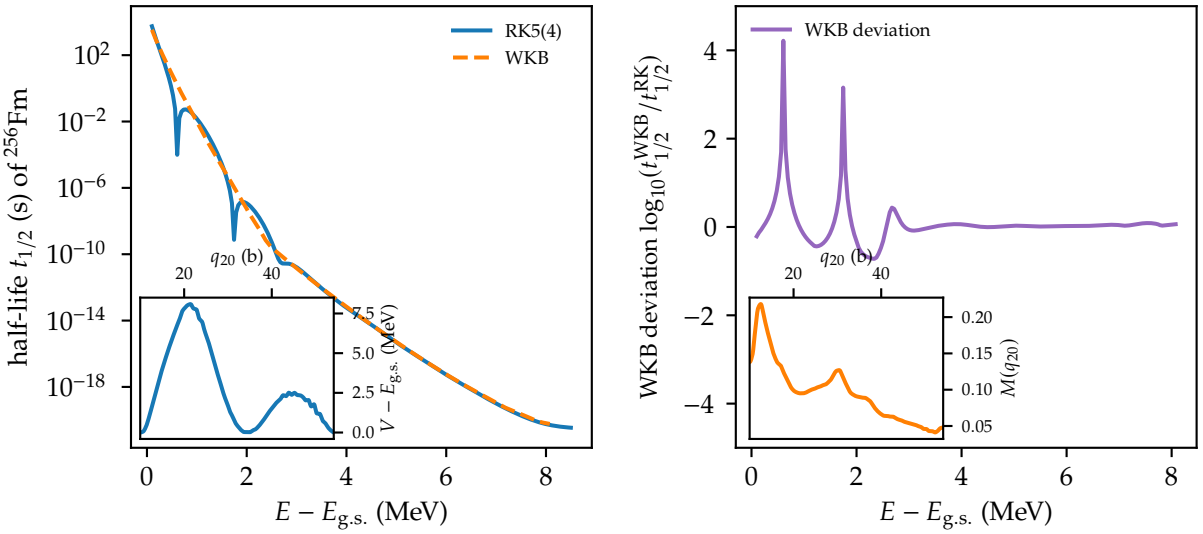

Figure 4.1: Left: spontaneous-fission half-life $t_{1/2}$ as a function of the zero-point energy $E - E_{\text{g.s.}}$ for the LAP of ^{256}Fm, from the numerical solution (RK5(4)) and from the WKB approximation. Insets: fission barrier and effective inertia, with the inertia in $\hbar^2\,\text{MeV}^{-1}\,\text{b}^{-2}$. Right: logarithmic deviation $\log_{10}(t_{1/2}^{\text{WKB}}/t_{1/2}^{\text{RK}})$.

The first noticeable feature of the half-life as a function of energy is the presence of the resonance peaks introduced for the double-humped barrier of section 3.2.2, which are absent for the single-humped barrier of ^{325}Fl. These peaks, corresponding to class-II resonances which the WKB formula (2.68) does not capture, reach three to four orders of magnitude, at least for the energy grid spacing of ~ 0.05 MeV used in the figures. Their number and density reflect the structure of the barrier: ^{256}Fm, with a single isomeric well, shows two well-separated peaks below 2 MeV, while the strongly multi-humped ^{245}Fr shows a dense sequence of them across the whole upper half of its barrier. Away from these peaks, the WKB result stays remarkably close to the Schrödinger one over a logarithmic scale spanning tens of decades: a choice of zero-point energy a few MeV below the barrier top covers more than seventy orders of magnitude in half-life between the three nuclei, and even then, the WKB deviation remains a few tenths of an order of magnitude.

A second type of deviation emerges again, one that was first observed for the single parabolic barrier of section 3.2.1: the smooth positive offset of a few tenths of an order of magnitude at low energy, decaying towards zero as the energy approaches the barrier top. It is most clearly seen for the single-humped barrier of ^{325}Fl, where no resonances obscure it. These three nuclei have substantially different barrier shapes, sizes and inertias, and yet all of them seem to display this low-energy ridge. This is a global behavior we will study in more detail in section 4.4.

Notice also how the inertia decreases with increasing deformation, with pronounced peaks at small deformation. This non-smooth behavior is the main source of interpolation error, as discussed in section 3.2.4.

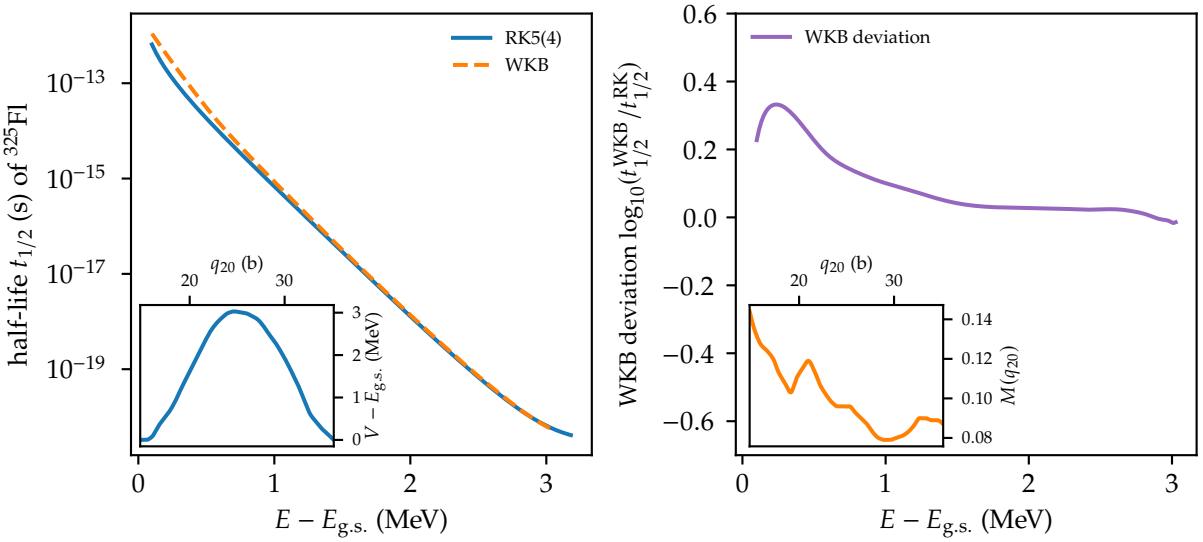

Figure 4.2: Left: spontaneous-fission half-life $t_{1/2}$ as a function of the zero-point energy $E - E_{g.s.}$ for the LAP of ^{325}Fl, from the numerical solution (RK5(4)) and from the WKB approximation. Insets: fission barrier and effective inertia, with the inertia in $\hbar^2\,\mathrm{MeV}^{-1}\,\mathrm{b}^{-2}$. Right: logarithmic deviation $\log_{10}(t_{1/2}^{WKB}/t_{1/2}^{RK})$.

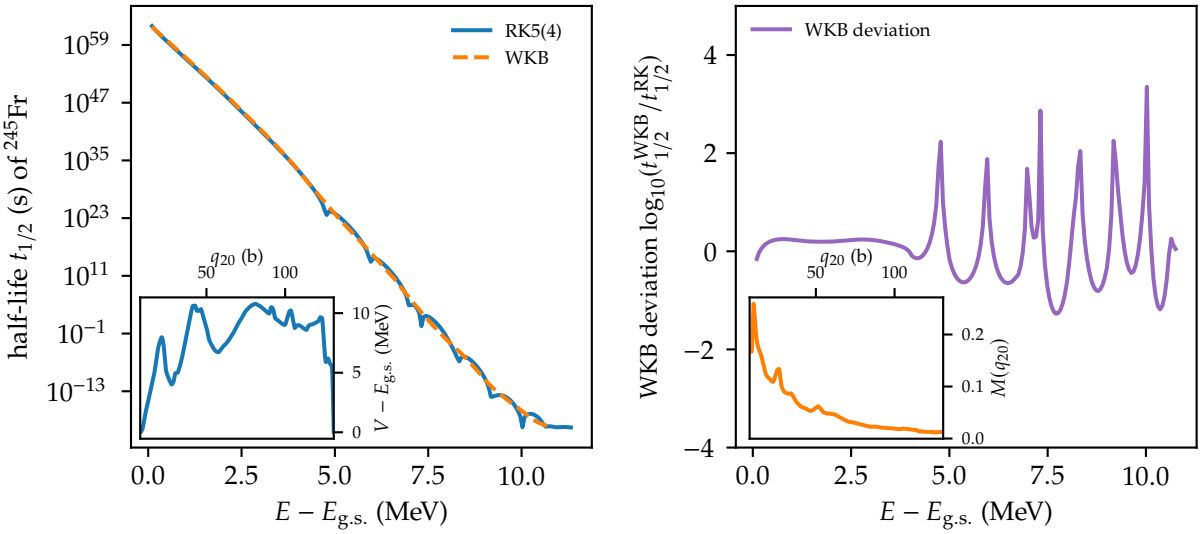

Figure 4.3: Left: spontaneous-fission half-life $t_{1/2}$ as a function of the zero-point energy $E - E_{g.s.}$ for the LAP of ^{245}Fr, from the numerical solution (RK5(4)) and from the WKB approximation. Insets: fission barrier and effective inertia, with the inertia in $\hbar^2\,\mathrm{MeV}^{-1}\,\mathrm{b}^{-2}$. Right: logarithmic deviation $\log_{10}(t_{1/2}^{WKB}/t_{1/2}^{RK})$.

The case of ^{256}Fm deserves a closer look, since it illustrates two features that will be relevant for the systematics of the next section. The first is that one of its class-II resonances lies very close to the evaluation energy, so that the deviation at $E_{exc} = 0.5$ MeV is no longer of a few tenths but of one full order of magnitude. The second is the broad bump visible in the deviation panel of

figure (4.1) between roughly 2 and 3 MeV, which is not a resonance but instead an interference effect. This bump originates from the difference in height of the two humps, of about 7.5 and 3 MeV respectively. Below the lower hump, the state in the isomeric well is confined on both sides and the transmission shows the sharp class-II peaks discussed before. As the energy approaches the top of the lower hump, the states are less confined, the peaks broaden and lose contrast. Once the lower hump is surpassed, the well is no longer bounded by two barriers: the outer side is now classically allowed, and the wave is only weakly reflected there instead of being trapped. The wave reflected back from the taller hump then interferes with the incoming one, forming an interference pattern. The oscillations from this pattern are analogous to the above-barrier ones already found for the square barrier in figure (3.1). The energy window in which they can appear is the interval between the two hump tops, so the effect is more noticeable for barriers whose humps differ most in height. In figure (4.3), for example, it is not apparent: the many humps of ^{245}Fr have comparable heights, and the sharp resonance peaks dominate over the whole range above 5 MeV, where the first isomeric well appears.

The values of the half-lives at $E_{\text{exc}} = 0.5$ MeV also offer insight themselves. Table (4.1) collects them for the three nuclei of the figures together with a few other representative cases, chosen to span the extremes of the data set.

	$t_{1/2}^{\text{Schr}}$ (s)	$t_{1/2}^{\text{WKB}}$ (s)	$\log_{10}$ ratio
^{256}Fm	7.95×10^{-1}	7.09×10^{0}	+0.95
^{325}Fl	1.84×10^{-14}	3.10×10^{-14}	+0.23
^{245}Fr	5.62×10^{59}	9.30×10^{59}	+0.22
^{286}Mc	1.11×10^{-11}	6.95×10^{-9}	+2.80
^{268}Po	1.05×10^{205}	1.13×10^{205}	+0.03
^{295}Sg	2.98×10^{-21}	5.89×10^{-21}	+0.30
^{236}U	3.85×10^{20}	6.13×10^{20}	+0.20
^{240}Pu	1.92×10^{13}	3.28×10^{13}	+0.23
^{252}Cf	7.16×10^{5}	1.50×10^{6}	+0.32

Table 4.1: Spontaneous-fission half-lives obtained from the numerical solution of the Schrödinger equation and from the WKB approximation at $E_{\text{exc}} = 0.5$ MeV, together with the deviation $\log_{10}(t_{1/2}^{\text{WKB}}/t_{1/2}^{\text{Schr}})$. The first three correspond to the fission paths of figures (4.1)–(4.3); the next three collect the extreme cases of the data set, namely the largest deviation (^{286}Mc), the longest half-life (^{268}Po) and the shortest one (^{295}Sg); the last three are some of the most commonly studied fissioning nuclei.

The half-lives in table (4.1) run from 10^{-21} s for ^{295}Sg to 10^{205} s for ^{268}Po, more than two hundred orders of magnitude. The shortest of them approaches the floor that this framework can produce: with $T_{\text{d}} \to 1$, which is approximately the case of barriers with maximum close to 0.5 MeV, the half-life reduces to a constant value of $\sim 10^{-21}$ s. Across this entire range, the deviations remain mostly of the same size. Besides ^{256}Fm and ^{286}Mc, the remaining deviations stay less than ~ 0.3 orders of magnitude. This constant deviation seems to be independent of the shape of the barrier. We already noted this barrier-independent behavior in appendix B.1 for the parabolic barrier, and the next section will show that it holds for the thousands of nuclei available.

Two entries stand out from this pattern. In ^{256}Fm, the deviation reaches +0.95 and in ^{286}Mc, the largest of the whole data set, it reaches +2.80. In both cases, a class-II resonance happens to lie close to the evaluation energy, so that the exact transmission is resonantly enhanced while the WKB one is not. This is explicitly observed in figure (4.1).

At a fixed evaluation energy $E_{\text{exc}} = 0.5$ MeV, the presence of a nearby resonance is therefore what mostly determines the deviation of WKB from the exact Schrödinger solution. For ^{245}Fr the resonances lie well above this energy, so the half-life is essentially unaffected, while for ^{256}Fm the lowest one falls close enough to dominate the deviation entirely. We can expect nuclei with low isomeric wells, such as the latter (see the inset of figure (4.1)), to be the most affected. These cases will become more visible in the following section.

4.2 Systematics across the nuclear chart

We now extend these calculations to the whole set of 3219 nuclei[1] at a fixed zero-point energy $E_{\text{exc}} = 0.5$ MeV. Figure (4.4) shows the logarithmic deviation between the WKB and Schrödinger half-lives as a function of the mass number A.

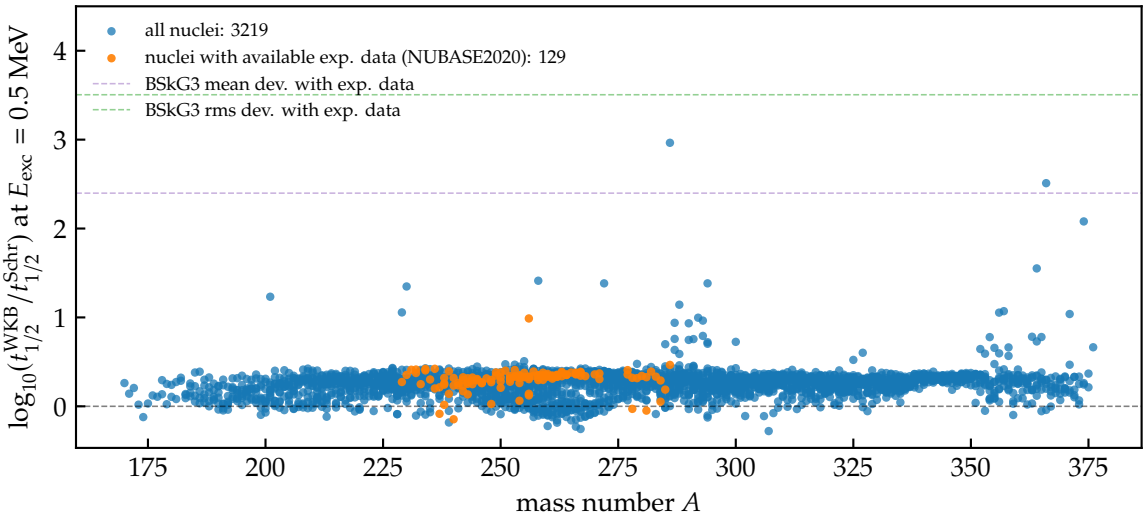

Figure 4.4: Logarithmic deviation $\log_{10}(t_{1/2}^{\text{WKB}}/t_{1/2}^{\text{Schr}})$ at $E_{\text{exc}} = 0.5$ MeV as a function of mass number, for the 3219 nuclei with a BSkG3 fission path. Nuclei with a measured spontaneous-fission half-life in NUBASE2020 [7] (129) are highlighted. The horizontal lines indicate the mean and rms deviation of the BSkG3 WKB half-lives with respect to the measured ones [2, 58]. 43 nuclei (1.3%, one of them measured) deviate by more than 0.5 orders of magnitude.

We can first notice the nearly constant deviation, which most of the cases in table (4.1) already suggested, but now we can observe that it holds in bulk: the distribution is narrow and centered slightly above zero, at $\lesssim 0.2$ orders of magnitude, with no visible trend in A across the two hundred mass units covered. The cases observed in figures (4.2) and (4.3) fall under this narrow distribution, for example. The 129 experimentally measured nuclei of NUBASE2020, highlighted in the figure, populate the same band as the rest. At the same time, they occupy only a small part of it, which illustrates how far beyond the measured region these mean-field calculations reach.

The positive offset is systematic: WKB is biased towards longer half-lives almost everywhere,

[1] Some 45 further nuclei, around 1.4% of the original set, are excluded because their barrier peak lies less than 0.5 MeV above the ground state, so that no classically forbidden region is left at the evaluation energy. These are very short-lived superheavy nuclei with $Z \gtrsim 113$, whose zero-point energy would require a dedicated treatment; we keep the global phenomenological choice instead, for simplicity.

which is equivalent to an underestimation of the transmission. This is the low-energy ridge already identified in the previous section and traced to the corner produced by the truncation of the potential. Its magnitude, a few tenths of an order of magnitude, is consistent with what was found for the truncated parabola and the double-humped barrier.

A tail of 43 nuclei, 1.3% of the total, deviates by more than 0.5 orders of magnitude, with excursions up to 3–4. These are mostly cases in which a class-II resonance happens to lie close to the evaluation energy $E_{\text{g.s.}}$ + 0.5 MeV, so that the exact transmission is resonantly enhanced while the WKB one is not. This is precisely the situation anticipated in the previous section for nuclei whose isomeric well lies low enough in energy. Only one nucleus of this tail belongs to the measured NUBASE2020 subset, namely ^{256}Fm from figure (4.1).

Not all of the outliers originate directly from a sharp resonance, though. As discussed for ^{256}Fm, barriers whose humps differ appreciably in height develop an interference pattern for energies above the top of the lower hump. Inspecting the deviation curves of the 43 outliers one by one, we found that $\sim$ 8–10 of them, such as ^{272}Bk, ^{325}Rf or ^{201}Th, show a broad bump of this kind around the evaluation energy rather than a narrow spike. However, as noted in the previous section, the two effects differ only in the degree to which the wave is trapped in the isomeric well, not in nature.

These outliers are physically real, but the sharp ones should be read with care: as shown in appendix B.2, the resonances are extremely narrow, so the determination of their position is highly sensitive, for example, to the accuracy of the mean-field input. They are best understood as an indication that a resonance is possible near the evaluation energy, rather than as a prediction of the specific half-life of that nucleus. The broader bumps from the interference pattern discussed above are less affected by this, since a small shift in the barrier would not move them away from the evaluation energy. Moreover, as seen in section 3.2.3, including a imaginary potential motivated from absorption in the isomer wells, would damp and broaden these resonances, so the tail found here should be read as an upper bound in this case.

It is worth putting the size of this deviation in perspective. The horizontal lines in figure (4.4) mark the mean and rms (root-mean-square) deviation of the BSkG3 WKB half-lives with respect to the measured ones. The entire WKB-Schrödinger spread, resonances included, sits below the deviations from experiment of a state-of-the-art model. It is also important to keep in mind that the uncertainty coming from the limited accuracy of $V(q_{20})$ and $M(q_{20})$, output of demanding mean-field calculations, dominates over the difference between the two tunneling treatments [21]. On the other side of the scale, the numerical uncertainties quantified in section 3.2.4 are far smaller than the deviation discussed here.

We can therefore observe that going beyond WKB by solving the collective Schrödinger equation does not change half-life systematics at the level of accuracy of current EDF input. WKB remains adequate for large-scale calculations of fission rates, while the exact solver matters for individual nuclei that happen to sit near a resonance.

4.3 Dependence on the barrier features

In appendix B.1, we noticed that the deviation as a function of energy behaves in the same way for different parameter values of the parabolic barrier. This hints at a barrier-independence of the deviation.

A natural question at this point is how the WKB deviation behaves across the range of more realistic fission barriers. We are interested to see if barriers with different lengths, heights or numbers of humps deviate differently, and if any correlation with these geometric descriptors can

be found along the nuclear chart. To this end, we extract a set of descriptors per nucleus: the mass and proton numbers A and Z, the barrier length Δq_{20}, the barrier height $\Delta V(q_{20})$, the number of humps, and the inertia variation from start to end $\Delta M(q_{20})$. These are compared with the target quantity $\log_{10}(t_{1/2}^{\mathrm{WKB}}/t_{1/2}^{\mathrm{Schr}})$. As in the previous section, we do not consider nuclei whose barrier peak lies below $E_{\mathrm{g.s.}} + 0.5$ MeV, since the WKB formula used in this work does not apply directly above the barrier top (section 3.1.3).

Figure (4.5) shows the marginal distributions of these features together with the pair plots between them, and figure (4.6) quantifies the same information through the Pearson correlation coefficients.

The marginal distributions are informative in themselves. The barrier length Δq_{20} is bimodal, with a main group below ~ 100 b and a second one around 150 b, while the barrier height $\Delta V(q_{20})$ is strongly peaked at a few MeV with a long tail extending up to ~ 40 MeV. The inertia variation $\Delta M(q_{20})$ is negative for essentially every nucleus, meaning that the inertia decreases along the path, as already seen in the insets of section 4.1. Most paths have one or two humps, with a small population reaching up to ten; this count, however, depends on how a hump is defined. Here we count local maxima of $V(q_{20})$ whose prominence exceeds 10% of the total barrier height, but never less than a 0.2 MeV floor. The relative term adapts to tall and short barriers alike, while the floor prevents ripples on a low barrier from being counted. Even so, marginal peaks may be included or missed, so the upper tail of this distribution should be read as indicative rather than exact. Finally, the deviation distribution is sharply peaked near 0.2 with a one-sided tail made of the resonance cases, as anticipated from figure (4.4).

Turning to the correlations, the deviation is weakly correlated with every descriptor: -0.36 with Δq_{20}, -0.34 with $\Delta V(q_{20})$, 0.30 with Z, 0.29 with $\Delta M(q_{20})$ and 0.15 with A. The signs of the two largest ones are in the expected direction, since longer and higher barriers deviate slightly less: a larger action means a deeper tunneling regime and therefore a better-behaved semiclassical limit. The correlation with $\Delta M(q_{20})$ is of comparable size; notice the correlation with Z (0.62), implying it is not fully independent of the other correlations.

Some of the behaviors one might expect beforehand are not observed. One could expect, for example, more humps to produce more resonances and therefore more deviation, since a class-II resonance requires an isomeric well to exist in the first place. Yet the number of humps is the least correlated descriptor of all (-0.08). The reason is that having a well is necessary but not sufficient: the well only enhances the deviation if one of its class-II states happens to fall at the evaluation energy, and where those states lie depends on the detailed shape of the barrier rather than on how many humps it has. Hitting a resonance at a fixed energy is therefore coincidental across the chart, and the effect washes out in the average.

The remaining correlations are largely redundant. The strongest entries of figure (4.6) are among the descriptors themselves (Z–$\Delta q_{20} = -0.81$, ΔV–$\Delta q_{20} = 0.79$, A–$Z = 0.82$), and they are physical: heavier, higher-Z nuclei sit closer to the point of instability, so their barriers are both lower and shorter. The descriptors are then different measures of the same heavy-to-superheavy trend, and the weak individual correlations of the log-ratio with each of them are not independent pieces of information but different projections of a single mild dependence.

Since the previous section established that the deviation is narrowly distributed and approximately the same for every barrier, it was actually reasonable to expect that the deviation would not correlate strongly with any of the descriptors. The absence of correlations is therefore a confirmation of the same conclusion reached before: the bulk of the WKB error is a boundary effect at the barrier feet, common to all fission paths and independent of their shape. On the other side, deviations coming from resonances are largely coincidental, so we did not expect them to correlate with any of the geometric features either. In short, no simple geometric property of the barrier

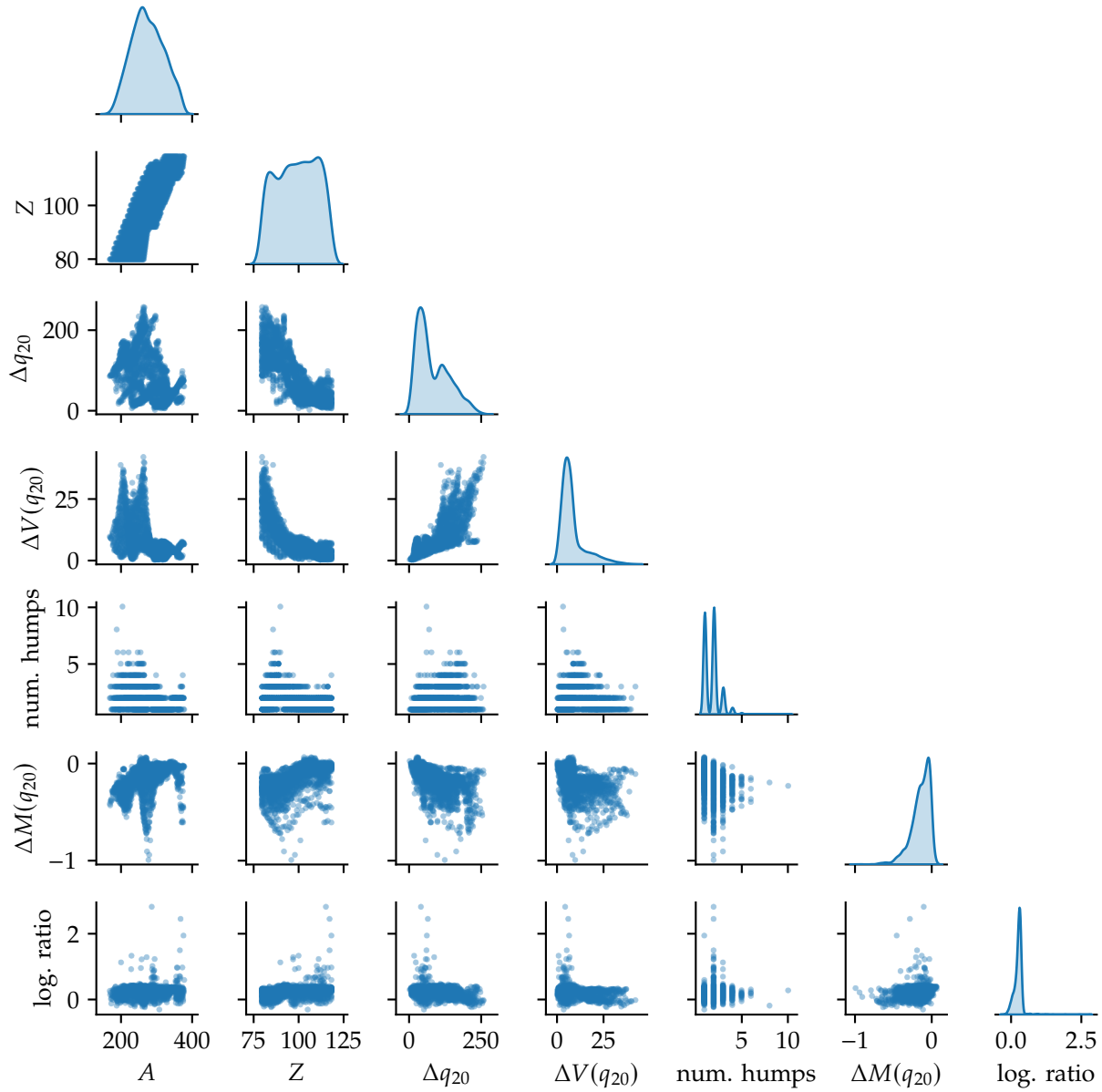

Figure 4.5: Pair plot of the barrier features: mass number A, proton number Z, barrier length Δq_{20}, barrier height $\Delta V(q_{20})$, number of humps and inertia variation $\Delta M(q_{20})$, together with the logarithmic deviation $\log_{10}(t_{1/2}^{\mathrm{WKB}}/t_{1/2}^{\mathrm{Schr}})$ at $E_{\mathrm{exc}} = 0.5$ MeV. Diagonal panels show the marginal density distributions of these.

predicts the WKB deviation since it is an barrier-independent effect.

4.4 Sensitivity to the choice of zero-point energy

We now address the pending discussion regarding the choice of the zero-point energy, and how sensitive the WKB deviation is to it for these more realistic barriers.

We remind that the value $E_{\mathrm{exc}} = 0.5$ MeV is a convention. It is commonly treated as an adjustable

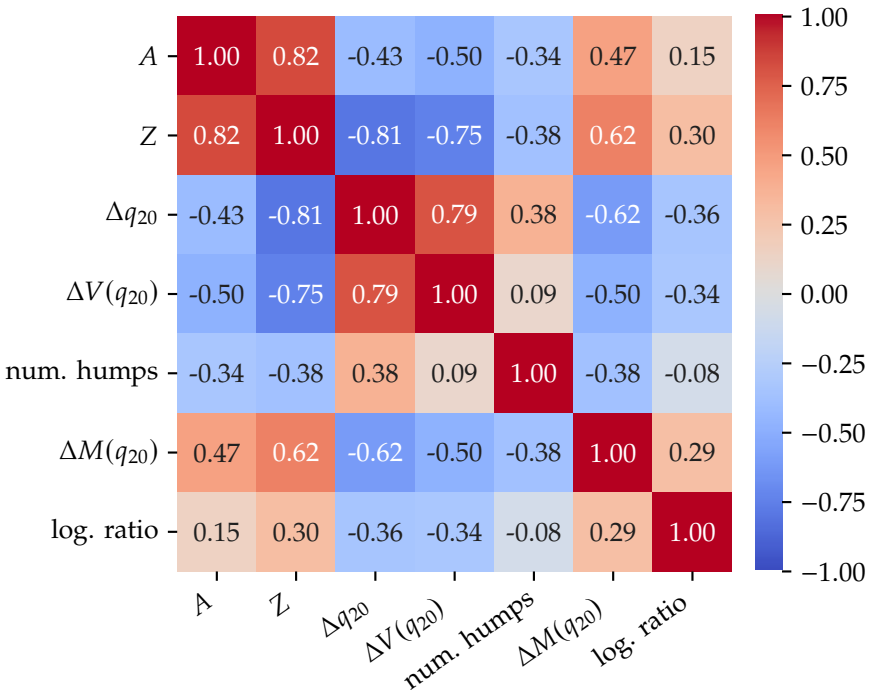

Figure 4.6: Pearson correlation matrix of the quantities of figure (4.5), for the same set of nuclei.

parameter which shifts the half-lives of neighboring nuclei as a whole [39]. Alternatives have been used in the literature, such as extracting the zero-point energy from the GCM formalism described in section 2.2.3 [9]; for Fm isotopes, for instance, this value is reported between $\sim$ 0.5 and 0.7 MeV. A zero E_{exc} is also a possible choice: the BSkG3 half-lives reported in [2] are WKB values evaluated at $E_{\text{exc}} = 0$, since the inertias used there are not obtained from the GCM formalism and therefore do not subtract a zero-point energy contribution. A direct comparison with those results is not possible here, because setting $E_{\text{exc}} = 0$ gives a trivial result for the numerical solution of the Schrödinger equation: the exact transmission vanishes at threshold. However, we are interested in the comparison between the WKB and Schrödinger treatments at a fixed energy rather than in the absolute half-lives themselves.

The deviation is therefore computed for all available fission paths on a grid of E_{exc} between 0.1 and 5 MeV, shown in figure (4.7). Since the WKB formula is applicable only below the barrier top, we exclude at each energy those nuclei whose barrier peak lies below E_{exc}. The red curve keeps track of the number of remaining nuclei, and the fraction of nuclei in each deviation bin is normalized to it. The white lines are the median (solid) and the 16th and 84th percentiles (dashed) of the distribution at each energy.

The overall behavior is the one already found for the individual paths of section 4.1: the low-energy ridge builds up below $\sim$ 1.5 MeV, and above $\sim$ 2 MeV the median settles close to zero and stays there. Figure (4.7) goes further and confirms that this is a property of the whole data set and not of the few nuclei examined earlier. The two reference curves confirm its origin: the truncated parabola reproduces the ridge while the smooth Eckart barrier does not, so the effect is indeed related to the corner at the barrier feet and not to the specifics of the fission paths.

The resonances appear here as the sparse population of points scattered well above the bulk, present at every energy and reaching two orders of magnitude or more. These amount to $\lesssim 1\%$ of

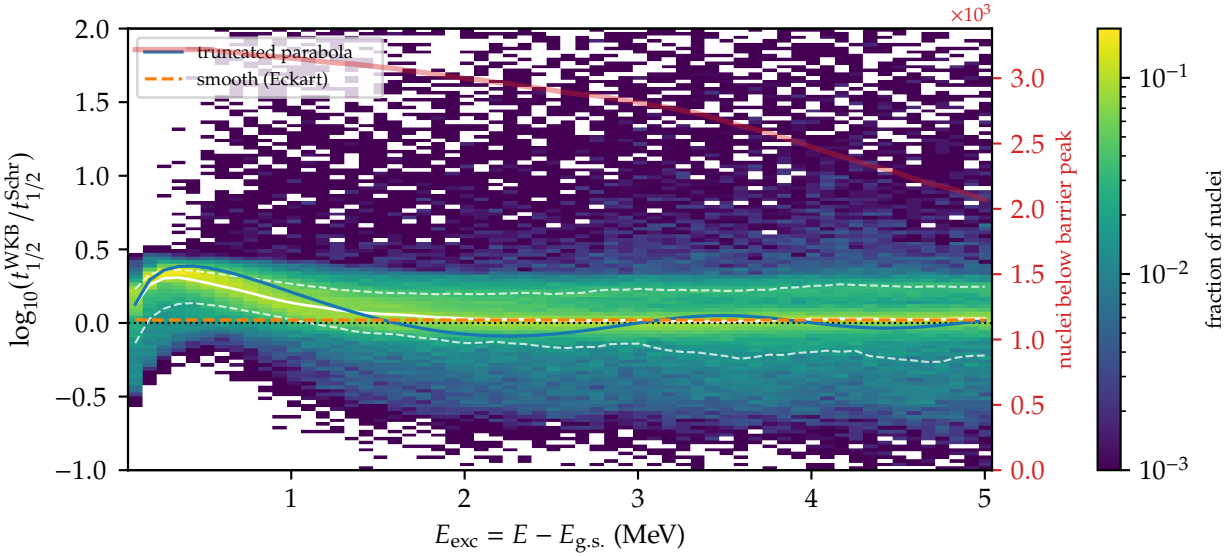

Figure 4.7: Distribution of the logarithmic deviation $\log_{10}(t_{1/2}^{\mathrm{WKB}}/t_{1/2}^{\mathrm{Schr}})$ as a function of the zero-point energy $E_{\mathrm{exc}} = E - E_{\mathrm{g.s.}}$, for the 3219 nuclei of the data set. The color scale gives the fraction of nuclei in each deviation bin. At each energy, the normalization is the number of nuclei whose barrier peak lies above E_{exc}, shown by the red curve on the right axis. White lines: median and quartiles. The blue and orange curves are the deviations obtained for a single truncated parabolic barrier and for a smooth Eckart barrier of comparable heights and widths.

the nuclei at any given energy, consistent with the 1.3% found at $E_{\mathrm{exc}} = 0.5$ MeV in section 4.2.

There is a feature we already noticed before in section 4.1 worth noting now for the whole nuclei set in a broad range of energies. First, the distribution is notably asymmetric, with a wider spread to positive deviations, which is expected since resonances enhance the exact transmission, while WKB cannot capture these resonances underestimating the transmission.

Two caveats should be kept in mind in this analysis. As already noted in section 3.2.1, the deviation diverges as $E_{\mathrm{exc}} \to 0$, because the exact transmission vanishes at threshold while the WKB expression tends to a constant. The distribution at very small energies is therefore not shown, and is in any case of little interest: a finite zero-point energy is required both physically and numerically in this approach. The second caveat concerns the changing population. The red curve falls from ~ 3200 to ~ 2000 nuclei between 0 and 5 MeV, so the sample surviving at high energy is biased towards tall barriers. The stabilization of the median above 2 MeV, and the mild but steady widening of the upper quartile above it, therefore reflect in part a change of population. As the energy increases there is also more room for resonances to occur, since more class-II states lie below the evaluation energy, which contributes to the gradual broadening of the upper quartile.

The deviation between the two treatments is therefore fairly insensitive to the choice of E_{exc}: over the whole range explored, the median stays within a few tenths of an order of magnitude of zero, never reaching a full order of magnitude even where the low-energy ridge is most pronounced. Therefore, the single-integral WKB formula overestimates the half-lives at low energies. The half-lives themselves behave very differently. As figures (4.1)–(4.3) show, they change by many orders of magnitude over the same interval, since the tunneling probability depends exponentially on the action. A shift of a few tenths of an MeV in E_{exc} therefore moves the predicted half-life far more than the difference between WKB and the exact solution ever does. This is also what makes the zero-point energy a useful parameter to adjust when reproducing experimental half-lives. The

choice of energy is thus relevant for the absolute half-lives, but substantially less so for the deviation of WKB from the exact solution, except in the isolated resonance cases.

4.5 Discussion

About the choice of the zero-point energy

A more complete discussion of the choice of the zero-point energy E_{exc} is in order, since this parameter has a strong effect on the absolute half-lives. The 0.5 MeV value rests on empirical arguments, and several authors simply treat E_{exc} as a free parameter [40, 62]. Values in the literature span $\sim$ 0.3–1.0 MeV [9, 62], while calculations that subtract other zero-point energies from the potential itself, such as the ones at the end of section 2.2.2, set $E_{\text{exc}} = 0$ [2, 63]. The convention is therefore not settled.

In WKB calculations the choice is often reported not to change the qualitative conclusions: for the $^{232-280}$U chain, the half-life trends are mostly the same for energies between 0.5 and 2.0 MeV in Gogny calculations, with a vertical displacement of $\sim$ 10 orders of magnitude across the energy interval [62]. In a Schrödinger framework this might not hold if nuclear states encounter resonances within the energy interval; these cases require special attention. As we have seen, increasing this energy shortens the half-life, most markedly for nuclei with higher and wider barriers [62], which often can be turned to advantage to improve the agreement with experiment [62, 63].

A more appropriate alternative to a global value would be to estimate the zero-point energy case by case, in a harmonic approximation, from the curvature of the potential around the minimum; typical values in the region are indeed around 0.5 MeV, but with fluctuations with neutron number [64]. In this case, we note that the assault frequency in the definition of $t_{1/2}$ (2.28) must change accordingly. As we have noted before, the GCM formalism (section 2.2.3) also provides a natural zero-point energy [9], and it is worth remarking that this last choice belongs properly to a collective Schrödinger equation, while other choices and discussions in the literature are formulated within WKB perspective only. We settled for the 0.5 MeV convention in sections 4.2 and 4.3 for simplicity, to study the qualitative behavior and correlations at this commonly adopted low energy region.

The role of the collective inertia and its uncertainty

Beyond the absence of correlation between $\Delta M(q_{20})$ and the deviation found in section 4.3, we have not yet asked how much the variation of the inertia along the path matters at all, even though it is a distinctive input of the collective Schrödinger equation with respect to the standard one. We therefore recomputed the half-life of every nucleus twice: once with the full $M(q_{20})$, and once with a constant inertia given by its average along the path. The two results differ by less than one order of magnitude for 60% of the chart, especially in the region $A \gtrsim 280$. Elsewhere the disagreement is large and systematically negative, the coordinate-dependent inertia predicting shorter half-lives by up to $\sim$ 100 orders of magnitude in the worst case. A coordinate-dependent inertia is thus essential over most of the chart, and a constant effective mass is not a safe simplification. It also shifts the positions and heights of the class-II resonances, so the WKB deviation changes accordingly for the nuclei affected by them.

It is worth remarking once again that the uncertainties from the underlying mean-field calculation are larger than anything separating WKB from the exact solution. For the inertia alone, the literature reports that the ATDHFB values are typically 1.5 to 2 times larger than the GCM ones, making the WKB action 20–40% larger, which can amount to several orders of magnitude in $t_{1/2}$ [62]. In Gogny calculations for the uranium isotope chain, this difference reaches 12 orders of

magnitude for the lighter isotopes at $E_0 = 0.5$ MeV and grows up to 31 orders with neutron number [62]. On top of the choice of scheme, the inertias used here are of the perturbative cranking type (section 2.2.3), known to underestimate the true values by a factor as small as 0.7 and to reduce the WKB action by 15% [62]. The ambiguity in the inertia alone is therefore plausibly a larger source of uncertainty in the absolute half-lives than anything examined in this chapter.

Extending the Schrödinger framework to larger collective spaces

A natural question at this point is whether the Schrödinger treatment can be extended in practice to more than one dimension, and what would change with respect to the one-dimensional implementation used here. This is not trivial, as we discussed in section 2.6, but it may well be physically relevant: as we mentioned in section 2.1, triaxiality ($q_{22} > 0$) lowers the top of the inner barrier of many actinides by at most a few MeV [5], and some superheavy nuclei with oblate ground states may fission through a triaxial path[2].

We already showed in section 2.6 how the multi-dimensional collective Schrödinger equation can be reduced to a one-dimensional equation along a path coordinate, with the transverse degrees of freedom entering through a zero-point energy added to the potential. However, the assumption of a unique path is not sufficient in a fully quantum mechanical description, since a bifurcation of the tunneling path could emerge in the presence of competing fission modes. One possibility is then a coupled-channel approach, in which the tunneling problem is solved numerically after expanding the wave function on a complete orthogonal basis in the coordinate transverse to the fission path [22], although its usefulness in practice is limited by the large number of channels needed to reach convergence and by the exponentially growing solutions of the closed channels.

Another possibility, still within the collective space and the Schrödinger equation, is a time-dependent perspective. In [66], the time-dependent Schrödinger equation is solved in a box with an imaginary absorbing potential at the edge, which absorbs the outgoing flux and thereby eases the boundary conditions. Diagonalizing the resulting non-Hermitian Hamiltonian gives the resonance energy and width directly from its complex eigenvalues. This study shows that the flux of the resonance wave function shows where the system tunnels without postulating a path, following the semiclassical escape path closely in a two-dimensional fission model. Despite the enormous range of time scales involved in fission, the method is suitable from a few fm/c up to half-lives of the order of a billion years. Most of such attempts have been tested on toy-model Hamiltonians with important numerical simplifications, but they consistently suggest that the adiabatic approximation may overestimate the spontaneous fission half-life significantly [1].

Regarding of what would change in more dimensions, the half-lives themselves are expected to be affected, since additional collective coordinates modify the barrier, but our concern here is rather the deviation of the WKB approximation. In this chapter we found this deviation to be largely insensitive to the barrier geometry, staying below one order of magnitude at low zero-point energies, so a similar pattern can reasonably be expected along the fission path as far as the barrier geometry is concerned. However, identifying the precise tunneling path could change the analysis substantially, and this problem, together with the possible interference between several such paths, remains an open problem [67], so further conclusions on multi-dimensional calculations are beyond the scope of this work.

[2]It has been shown that this lowering comes together with an increase of the collective inertia, which tends to compensate in the final WKB action, so that the net impact of triaxiality on $t_{1/2}$ is rather limited [62]. However, this result depends strongly on the assumptions underlying the calculation of the inertia: the perturbative approach tends to drive the system towards near-axial shapes, while non-perturbative calculations show stronger triaxial effects [65].

Chapter 5

Conclusions

In state-of-the-art calculations, spontaneous fission half-lives are almost always obtained from a single WKB action integral along a fission path. The formula is practical and considerably simpler to implement than the solution of the collective Schrödinger equation, and for that reason it is rarely questioned in the literature. The aim of this work was to test the WKB estimate against the solution of the problem it approximates, the one-dimensional collective Schrödinger equation. By confronting both approaches on fission paths of microscopic origin and studying the systematics of the resulting deviation, we aimed to establish to what extent the WKB approximation is sufficient for large-scale predictions of spontaneous fission rates.

For this purpose we developed a solver for the one-dimensional Schrödinger equation for a given fission barrier and coordinate-dependent inertia, integrated numerically and matched to plane-wave asymptotics at the boundaries. The quadrupole moment q_{20} is taken as the collective coordinate. The transmission coefficient, and hence the half-life, was computed from the transmitted amplitude. After validating the results on analytical benchmarks and performing stability tests, the solver was applied to the 3219 axially symmetric fission paths available from the BSkG3 mean-field calculations.

The main findings from the calculations can be summarized as follows:

- WKB and the Schrödinger equation agree to $\simeq 0.2$ orders of magnitude at $E_{\mathrm{exc}} = 0.5$ MeV for the large majority of the 3219 BSkG3 paths, over half-lives covering more than two hundred orders of magnitude.
- The residual difference is dominated by a low-energy offset of boundary-reflection origin, tied to the corners formed at the barrier feet by the truncation of the potential, which is required in order to impose the boundary conditions of the numerical scheme.
- A sparse population of 1.3% of the nuclei deviates by more than 0.5 orders of magnitude, and up to 3–4, through class-II resonances, which the single-integral WKB formula cannot reproduce. These resonances originate from the quasi-bound states of the isomeric wells present in the fission barrier, and the nuclei affected are those whose isomeric well lies low enough for one of these states to fall close to the chosen zero-point energy.
- The deviation is not correlated with any single barrier feature ($|\rho| \leq 0.4$), which indicates that it is largely barrier-independent.
- Leaving aside the resonances, which represent a small population at every energy considered, the deviation is only mildly sensitive to the choice of zero-point energy: it peaks at 0.3–0.4 orders of magnitude below about 1.5 MeV and settles near zero above roughly 2 MeV.

The main contribution of this work lies in the scale of the comparison. Although the accuracy of the WKB formula had been assessed previously on model barriers or on a reduced number of nuclei, the present assessment rests instead on thousands of fission paths, each of them extracted from a full EDF calculation of the PES and of the collective inertia. Over a sample of this size, the two deviations listed above are not isolated observations anymore and reveal their nature: the offset is an effect of the boundary conditions, shared by every path irrespective of its shape, while the resonances are coincidental across the distribution of nuclei, arising only when a quasi-bound state happens to lie close to the evaluation energy. Their lack of correlation with the barrier features is therefore the expected outcome, since neither mechanism is related to the geometry of the path.

A second outcome of the analysis is an ordering of the sources of uncertainty entering the calculation. The mean-field input dominates: the uncertainty on the collective inertia alone displaces the half-lives by more than the difference between the two tunneling treatments. The choice of zero-point energy follows, then the WKB approximation itself, and finally the numerical error, which is negligible in comparison. The entire WKB-Schrödinger spread, resonances included, remains below the deviation of the BSkG3 half-lives from the measured ones [2], so the semiclassical treatment is not the limiting approximation of current large-scale predictions.

Some limitations of the present study should be stated. The calculation is one-dimensional and restricted to axial symmetry, so that triaxial degrees of freedom are excluded. The fission path is obtained as a least-action path, that is, by minimizing the WKB action, so that the exact solver is applied to a trajectory selected on semiclassical grounds. Although the comparison is meaningful, since both treatments share the same input, a proper fully quantum definition of the fission path is not available. The truncation of the barrier is physically motivated but not unique, and gives rise to the systematic offset, which should therefore be attributed to a numerical/physical setup rather than to the WKB formula alone.

These limitations suggest the natural continuations of this work. The choice of zero-point energy is the most immediate issue to address: estimating this quantity case by case from the curvature of the potential around the ground-state minimum, instead of adopting a global value, would constrain the least controlled ingredient of the calculation. The extension to larger collective spaces constitutes the more ambitious direction, in which the notion of a single fission path is no longer meaningful and the bifurcation of the tunneling amplitude among competing valleys can be addressed properly.

The objective at the beginning of this work therefore admits a twofold conclusion. Solving the collective Schrödinger equation in place of the WKB formula modifies the predicted half-lives only marginally at the present accuracy of the mean-field input, so that the semiclassical estimate remains adequate for large-scale calculations. In one dimension, however, the exact solution requires seconds of computation per nucleus, a negligible cost compared with that of the PES and the collective inertia. The approximation can therefore be removed at little expense, with the additional benefit of recovering the isolated nuclei situated close to a class-II resonance, for which the two treatments differ by a few orders of magnitude. The situation is different in larger collective spaces, where the quantum effects arising from the competition between fission paths, and the numerical treatment they require, are far from trivial; whether the exact solution remains equally accessible in that case is a question beyond the scope of this work.

Appendix A

Additional derivations on WKB

A.1 Matching of WKB solutions across a turning point for variable mass

We are interested in solving the one-dimensional collective Schrödinger equation near a turning point:

$$\frac{1}{\sqrt{M(q)}}\frac{\mathrm{d}}{\mathrm{d}q}\left(\frac{1}{\sqrt{M(q)}}\frac{\mathrm{d}\psi}{\mathrm{d}q}\right)+\frac{2}{\hbar^2}(E-V(q))\psi=0. \tag{A.1}$$

We perform the change of variable:

$$x=\int^{q}\sqrt{M(q')}\,\mathrm{d}q'\,, \qquad \frac{\mathrm{d}}{\mathrm{d}x}=\frac{1}{\sqrt{M(q)}}\frac{\mathrm{d}}{\mathrm{d}q}, \tag{A.2}$$

and therefore, from (A.1):

$$\frac{\mathrm{d}^2\psi}{\mathrm{d}x^2}-\frac{2}{\hbar^2}(E-V(q(x)))\psi=0. \tag{A.3}$$

If q_t is a turning point, in the vicinity of $x_\mathrm{t}=x(q_\mathrm{t})$ we consider the linear approximation:

$$U(x)\equiv V(q(x))\approx E+U'(x_\mathrm{t})(x-x_\mathrm{t}), \tag{A.4}$$

where we considered that $U(x_\mathrm{t})=V(q(x_\mathrm{t}))=V(q_\mathrm{t})=E$ since it is a turning point. Notice that since $\sqrt{M(q)}>0$, the transformation defined by (A.2) is strictly monotonic and therefore invertible, then $q(x_\mathrm{t})=q_\mathrm{t}$. The equation to be solved is then:

$$\frac{\mathrm{d}^2\psi}{\mathrm{d}x^2}-\frac{2}{\hbar^2}U'(x_\mathrm{t})(x-x_\mathrm{t})\psi=0. \tag{A.5}$$

Performing the change of variable:

$$y=\left(\frac{2}{\hbar^2}U'(x_\mathrm{t})\right)^{1/3}(x-x_\mathrm{t}), \tag{A.6}$$

we arrive at the Airy equation:

$$\frac{\mathrm{d}^2\psi}{\mathrm{d}y^2}-y\psi=0. \tag{A.7}$$

This is a well-known equation whose solutions are the Airy functions $\mathrm{Ai}(y)$ and $\mathrm{Bi}(y)$. The asymptotic forms of these functions for $y \to \pm\infty$ are [68]:

$$\mathrm{Ai}(y) \approx \begin{cases} \dfrac{1}{\sqrt{\pi}|y|^{1/4}} \sin\left(\dfrac{2}{3}(-y)^{3/2} + \dfrac{\pi}{4}\right), & y \ll 0, \\ \dfrac{1}{2\sqrt{\pi}y^{1/4}} \exp\left(-\dfrac{2}{3}y^{3/2}\right), & y \gg 0. \end{cases} \quad \mathrm{Bi}(y) \approx \begin{cases} \dfrac{1}{\sqrt{\pi}|y|^{1/4}} \cos\left(\dfrac{2}{3}(-y)^{3/2} + \dfrac{\pi}{4}\right), & y \ll 0, \\ \dfrac{1}{\sqrt{\pi}y^{1/4}} \exp\left(\dfrac{2}{3}y^{3/2}\right), & y \gg 0. \end{cases} \tag{A.8}$$

From (A.4) and (A.6) we see that:

$$E - U(x) = -U'(x_\mathrm{t})(x - x_\mathrm{t}) = -\frac{1}{2}(2\hbar U'(x_\mathrm{t}))^{2/3} y. \tag{A.9}$$

Let us consider the following integral for $E > U(x)$ (where $y < 0$):

$$\int_q^{q_\mathrm{t}} k(q')\,\mathrm{d}q' = \frac{1}{\hbar}\int_x^{x_\mathrm{t}} \sqrt{2(E - U(x'))}\,\mathrm{d}x' = s\int_y^0 (-y')^{1/2}\,\mathrm{d}y' = \frac{2}{3}s(-y)^{3/2}, \tag{A.10}$$

where we used (2.56), the change of variable (A.2) was performed in the first integral and where we defined $s = \mathrm{sgn}(U'(x_\mathrm{t}))$, which comes from the cubic root in (A.6). This relates the Airy variable y to the WKB phase integral on the classically allowed side of the turning point. Analogously, on the classically forbidden side, for $E < U(x)$ (where $y > 0$):

$$\int_{q_\mathrm{t}}^q \kappa(q')\,\mathrm{d}q' = \frac{1}{\hbar}\int_{x_\mathrm{t}}^x \sqrt{2(U(x') - E)}\,\mathrm{d}x' = s\int_0^y y'^{1/2}\,\mathrm{d}y' = \frac{2}{3}s y^{3/2}. \tag{A.11}$$

Now, consider a turning point q_1 where the potential is increasing, i.e., $U'(x_1) > 0$. The region $q < q_1$ corresponds to $y < 0$, and $q > q_1$ corresponds to $y > 0$. If we consider that:

$$\psi(q \simeq q_1) = 2C\,\mathrm{Ai}(y) + D\,\mathrm{Bi}(y), \tag{A.12}$$

and $|y| \propto 2|E - V(q)|$, we can use (A.8), (A.10) and (A.11) with $s = 1$ to obtain the asymptotic form for the case of a positive-slope turning point:

$$\psi(q \simeq q_1) = \begin{cases} \dfrac{1}{[2(E - V(q))]^{1/4}} \left[2C\sin\left(\displaystyle\int_q^{q_1} k(q')\,\mathrm{d}q' + \frac{\pi}{4}\right) + D\cos\left(\int_q^{q_1} k(q')\,\mathrm{d}q' + \frac{\pi}{4}\right)\right], & q \lesssim q_1, \\ \dfrac{1}{[2(V(q) - E)]^{1/4}} \left[C\exp\left(-\displaystyle\int_{q_1}^q \kappa(q')\,\mathrm{d}q'\right) + D\exp\left(\int_{q_1}^q \kappa(q')\,\mathrm{d}q'\right)\right], & q \gtrsim q_1, \end{cases} \tag{A.13}$$

where the constants from $|y|$ in the amplitude were absorbed by C and D.

Analogously, we now consider a turning point q_2 with decreasing potential, i.e., $U'(x_2) < 0$ and therefore $s = -1$. The region $q < q_2$ corresponds to $y > 0$, and $q > q_2$ corresponds to $y < 0$. Finally, using (A.12), (A.8), (A.10) and (A.11) with $s = -1$, we obtain the asymptotic form for the case of a negative-slope turning point:

$$\psi(q \simeq q_2) = \begin{cases} \dfrac{1}{[2(V(q)-E)]^{1/4}} \left[C \exp\left(-\displaystyle\int_q^{q_2} \kappa(q')\, \mathrm{d}q' \right) + D \exp\left(\displaystyle\int_q^{q_2} \kappa(q')\, \mathrm{d}q' \right) \right], & q \lesssim q_2, \\ \dfrac{1}{[2(E-V(q))]^{1/4}} \left[2C \sin\left(\displaystyle\int_{q_2}^{q} k(q')\, \mathrm{d}q' + \dfrac{\pi}{4} \right) + D \cos\left(\displaystyle\int_{q_2}^{q} k(q')\, \mathrm{d}q' + \dfrac{\pi}{4} \right) \right], & q \gtrsim q_2. \end{cases} \tag{A.14}$$

A.2 Transmission coefficient definition for variable mass

In order to obtain the probability currents needed to define the transmission coefficient, defined as the ratio between transmitted and incident fluxes, we need to express the collective Schrödinger equation (2.40) as a continuity equation. We start from a time-dependent version of (2.40):

$$\left(-\frac{\hbar^2}{2D(\mathbf{q})} L(\mathbf{q}) + V(\mathbf{q}) \right) \Psi(\mathbf{q}, t) = i\hbar \frac{\partial}{\partial t} \Psi(\mathbf{q}, t). \tag{A.15}$$

where we defined:

$$L\Psi \equiv \sum_{ij} \frac{\partial}{\partial q_i} \left(D(\mathbf{q}) B_{ij}(\mathbf{q}) \frac{\partial \Psi}{\partial q_j} \right). \tag{A.16}$$

Motivated by the natural volume element in collective space, given by $\mathrm{d}\tau = D\, \mathrm{d}\mathbf{q}$, we define the probability density as:

$$\rho(\mathbf{q}, t) = D(\mathbf{q}) |\Psi(\mathbf{q}, t)|^2. \tag{A.17}$$

Taking the time derivative of ρ we have:

$$\frac{\partial \rho}{\partial t} = D \left(\frac{\partial \Psi^*}{\partial t} \Psi + \Psi^* \frac{\partial \Psi}{\partial t} \right) = D \left(\left[-\frac{i\hbar}{2D} L\Psi^* + \frac{i}{\hbar} V \Psi^* \right] \Psi + \Psi^* \left[\frac{i\hbar}{2D} L\Psi - \frac{i}{\hbar} V \Psi \right] \right), \tag{A.18}$$

$$= \frac{i\hbar}{2} (\Psi^* L\Psi - \Psi L\Psi^*), \tag{A.19}$$

where we assumed that the potential is real, i.e., $V = V^*$. Now, if we define a probability current as:

$$J_i(\mathbf{q}, t) = \frac{\hbar}{2i} \sum_j D B_{ij} \left(\Psi^* \frac{\partial \Psi}{\partial q_j} - \Psi \frac{\partial \Psi^*}{\partial q_j} \right), \tag{A.20}$$

we can take the divergence of J:

$$\sum_i \frac{\partial J_i}{\partial q_i} = \frac{\hbar}{2i} \sum_{ij} \left[\frac{\partial}{\partial q_i} \left(D B_{ij} \right) \left(\Psi^* \frac{\partial \Psi}{\partial q_j} - \Psi \frac{\partial \Psi^*}{\partial q_j} \right) + D B_{ij} \frac{\partial}{\partial q_i} \left(\Psi^* \frac{\partial \Psi}{\partial q_j} - \Psi \frac{\partial \Psi^*}{\partial q_j} \right) \right] \tag{A.21}$$

$$= -\frac{i\hbar}{2} \left[\Psi^* \left(L\Psi + \sum_{ij} D B_{ij} \frac{\partial \Psi^*}{\partial q_i} \frac{\partial \Psi}{\partial q_j} \right) - \Psi \left(L\Psi^* + \sum_{ij} D B_{ij} \frac{\partial \Psi}{\partial q_i} \frac{\partial \Psi^*}{\partial q_j} \right) \right] \tag{A.22}$$

$$= -\frac{i\hbar}{2} (\Psi^* L\Psi - \Psi L\Psi^*), \tag{A.23}$$

where we assumed that B is symmetric, i.e., $B_{ij} = B_{ji}$, which can easily be seen from (2.29) by swapping the i and j indices and relabeling them. From (A.19) and (A.23), we obtain the continuity equation:

$$\frac{\partial \rho}{\partial t} + \sum_i \frac{\partial J_i}{\partial q_i} = 0. \tag{A.24}$$

As usual, the transmission coefficient is defined as the ratio between the transmitted and incident fluxes. In the one-dimensional case, the transmitted flux is given by:

$$T = \frac{\text{transmitted flux}}{\text{incident flux}} = \frac{J_{\text{transm}}(q,t)}{J_{\text{inc}}(q,t)}, \tag{A.25}$$

where we consider that both waves propagate in the same direction and:

$$J_{\text{transm}}(q,t) = \frac{\hbar}{2i\sqrt{M(q)}}\left(\Psi^* \frac{\partial \Psi}{\partial q} - \Psi \frac{\partial \Psi^*}{\partial q}\right). \tag{A.26}$$

Assume a stationary state at a fixed energy E: $\Psi(\mathbf{q},t) = \psi(\mathbf{q})\exp(-iEt/\hbar)$. We can calculate now the transmission coefficient for the WKB solution (2.52):

$$\psi_\pm(q) = \frac{C_\pm}{(2|E - V(q)|)^{1/4}} \exp\left(\pm \frac{i}{\hbar}\int^q p(q')\, \mathrm{d}q'\right) \equiv A_\pm(q) \exp\left(\pm \frac{i}{\hbar}\int^q p(q')\, \mathrm{d}q'\right). \tag{A.27}$$

We consider $p(q)$ real, since the incident and transmitted waves are in classically allowed regions, i.e., $E > V(q)$. Let us calculate the derivative of $\psi_\pm$:

$$\frac{\mathrm{d}\psi_\pm}{\mathrm{d}q} = \left(\frac{A'}{A} \pm \frac{i}{\hbar}p(q)\right)\psi_\pm. \tag{A.28}$$

Therefore:

$$J_\pm = \frac{\hbar}{2i\sqrt{M(q)}}\left[\left(\frac{A'}{A} \pm \frac{i}{\hbar}p(q)\right)|\psi_\pm|^2 - \left(\frac{A'}{A} \mp \frac{i}{\hbar}p(q)\right)|\psi_\pm|^2\right] = \pm\frac{p(q)}{\sqrt{M(q)}}|\psi_\pm|^2 \tag{A.29}$$

$$= \pm\frac{\sqrt{2M(q)(E - V(q))}}{\sqrt{M(q)}}\frac{|C_\pm|^2}{\sqrt{2(E - V(q))}} = \pm|C_\pm|^2. \tag{A.30}$$

where we consider that the exponentials with time dependence cancel. By taking both waves moving in the positive direction, we obtain the (direct) transmission coefficient:

$$T_{\mathrm{d}} = \frac{|C_{\text{transm}}|^2}{|C_{\text{inc}}|^2}, \tag{A.31}$$

where C_{inc} and C_{transm} are the coefficients of the incident and transmitted waves, respectively.

Appendix B

Additional tests on numerical implementation

B.1 Apparent universality of the low-energy WKB offset

The objective of this appendix is to test whether the positive offset seen at low energy in the WKB half-life deviation of section 3.2.1 is a feature of the barrier shape or a global property. To this end, we take a truncated parabola and vary one parameter at a time, the barrier height V_b, the width a and the constant inertia M, over ranges resembling those of the real BSkG3 barriers.

Figure (B.1) shows two features common to all parameter values: a positive peak of ≈ 0.4 orders of magnitude at low energy, and decaying oscillations towards zero. While the peak position and the location of the oscillations shift with the parameters, the height of the low-energy ridge is essentially independent of V_b, a and M. The offset is therefore intrinsic to the truncation, at least, and not a property of a specific barrier. Since the half-lives of chapter 4 are evaluated at the fixed zero-point energy $E_{\text{exc}} = 0.5$ MeV, which falls in this low-energy region, the offset is the dominant WKB deviation in those results.

B.2 Resolution of class-II resonances

The class-II resonances of section 3.2.2 are far narrower than they appear in a scan of $T_{\text{d}}(E)$. This appendix quantifies how narrow they are and what it takes to resolve one, using the lowest-energy resonance of that section as a test case.

Its position, found by minimization of $-\log_{10} T_{\text{d}}(E)$, is $E_{\text{res}} = 2.3998772$ MeV, which agrees to 5×10^{-5} with the ground-state energy of the intermediate parabola, $V_2 + \frac{1}{2}\hbar\omega_2 \approx 2.4$ MeV, confirming that the resonance originates from the quasi-bound states of the isomeric well. Its width, obtained by bisection on the half-maximum, is $\Gamma = 4.24 \times 10^{-9}$ MeV $= 4.2$ meV, and the peak rises to $T_{\text{d}} = 4.3 \times 10^{-3}$ against a background of $\sim 10^{-16}$.

A fixed uniform grid is therefore not a viable way to find it, since covering a 0.4 MeV interval at a spacing able to resolve Γ would require $\sim 2.4 \times 10^{9}$ points. On any coarser grid the nodes almost never land on the maximum, so the displayed peak height is set by the grid rather than by the physics, as the right panel of figure (B.2) shows: the recovered height degrades by orders of magnitude as soon as the spacing exceeds the width. This highlights the practical value of the complex potentials of section 3.2.3, where absorption broadens and damps the resonances into structure that a usable energy grid can represent.

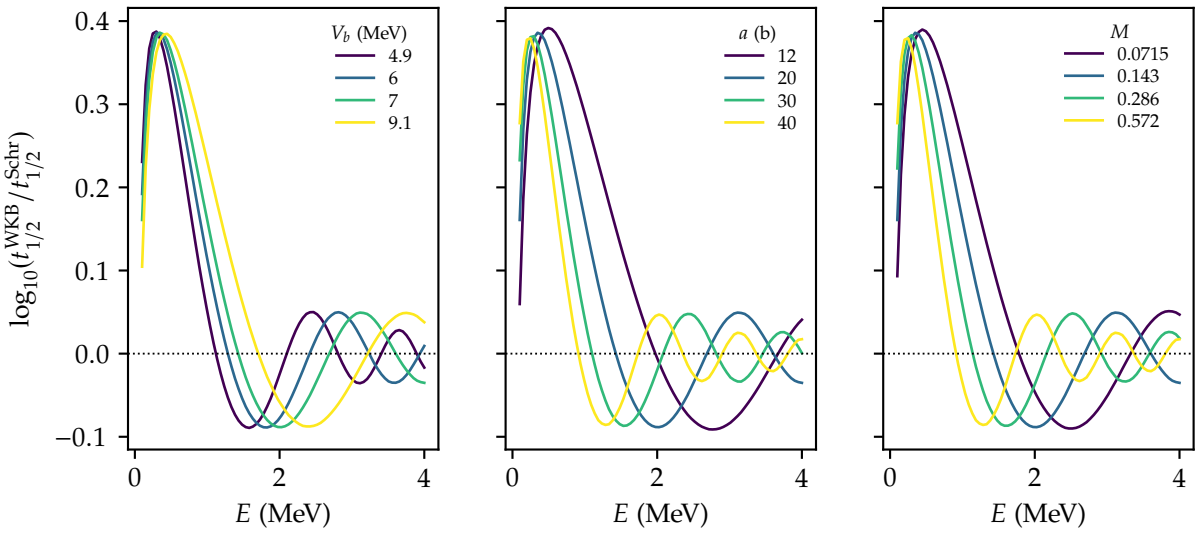

Figure B.1: WKB deviation of the half-life, $\log_{10}(t_{1/2}^{\mathrm{WKB}}/t_{1/2}^{\mathrm{Schr}})$, for a truncated parabolic barrier as a function of energy, varying the barrier height V_b (left), the width a (centre) and the constant inertia M (right) over similar ranges of the BSkG3 barriers.

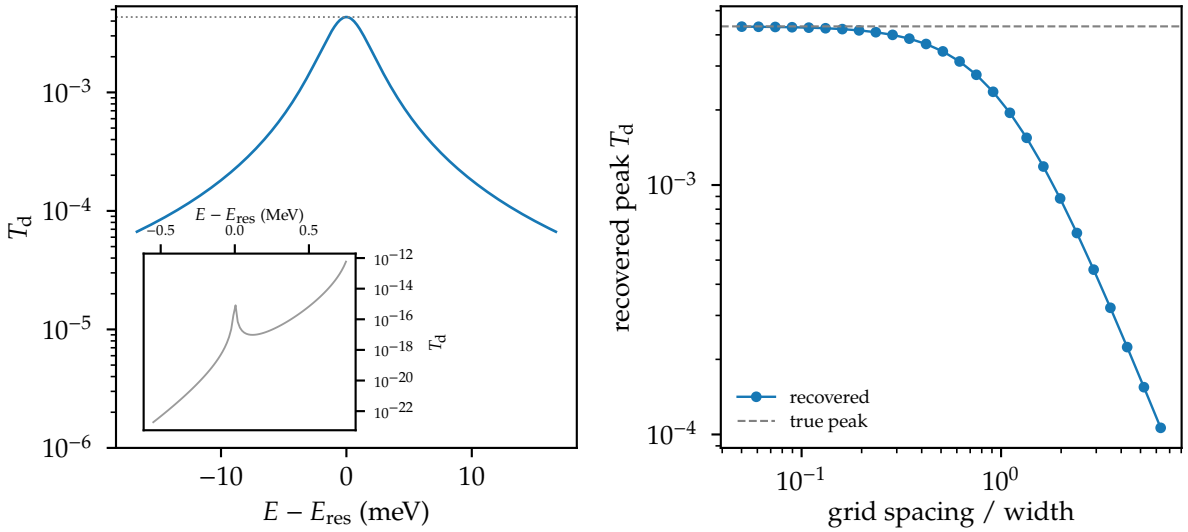

Figure B.2: Resolution of the lowest-energy class-II resonance of the double-humped barrier of section 3.2.2. Left: transmission coefficient in a window of a few meV around the resonance energy E_{res}; the inset shows the same resonance on a broader energy scale, to visualize the magnitude of the peak. Right: peak value recovered from a uniform energy grid as a function of the grid spacing in units of the resonance width, assuming an estimation lying midway between two grid nodes, compared with the true peak.

Acknowledgements

I would like to express my sincere gratitude to my main supervisor, Dr. Wouter Ryssens, for giving me the foundations, the guidance, the tools and the suggestions needed to carry out this work successfully. I am very grateful for the time he devoted to advising me on this project, and for his support throughout the administrative process of the mobility. I would also like to thank Dr. Adrián Sánchez-Fernández for his support and guidance during the development of this work, and prof. Lorenzo Fortunato for welcoming this project and taking part in it, and for his time and feedback. My thanks go as well to the IAA group at the ULB, for hosting me during my stay and for their feedback.

I owe special thanks to my mother and my father, who have believed and invested in me, and on whose unconditional support I have been able to count throughout my studies. To my sister and my grandmother, who were always there whenever I needed them.

Finally, to Diego, for being there for me every day and for making the hardest moments much easier with his company and his encouragement.

Bibliography

[1] N. Schunck and D. Regnier, Progress in Particle and Nuclear Physics **125**, 103963 (2022).

[2] A. Sánchez-Fernández, S. Bara, W. Ryssens, and S. Goriely, Physics Letters B **874**, 140287 (2026).

[3] N. Schunck and L. M. Robledo, Reports on Progress in Physics **79**, 116301 (2016).

[4] S. Goriely, Eur. Phys. J. A **51**, 22 (2015).

[5] W. Ryssens, G. Scamps, S. Goriely, and M. Bender, The European Physical Journal A **59**, 96 (2023).

[6] M. Bender, R. Bernard, G. Bertsch, S. Chiba, J. Dobaczewski, N. Dubray, S. A. Giuliani, K. Hagino, D. Lacroix, Z. Li, P. Magierski, J. Maruhn, W. Nazarewicz, J. Pei, S. Péru, N. Pillet, J. Randrup, D. Regnier, P.-G. Reinhard, L. M. Robledo, W. Ryssens, J. Sadhukhan, G. Scamps, N. Schunck, C. Simenel, J. Skalski, I. Stetcu, P. Stevenson, S. Umar, M. Verriere, D. Vretenar, M. Warda, and S. Åberg, J. Phys. G: Nucl. Part. Phys. **47**, 113002 (2020).

[7] F. Kondev, M. Wang, W. Huang, S. Naimi, and G. Audi, Chinese Physics C **45**, 030001 (2021).

[8] P. Möller, A. J. Sierk, T. Ichikawa, A. Iwamoto, R. Bengtsson, H. Uhrenholt, and S. Åberg, Phys. Rev. C **79**, 064304 (2009).

[9] A. Staszczak, A. Baran, and W. Nazarewicz, Phys. Rev. C **87**, 024320 (2013).

[10] M. Warda and J. L. Egido, Phys. Rev. C **86**, 014322 (2012).

[11] S. Levit, J. W. Negele, and Z. Paltiel, Phys. Rev. C **22**, 1979 (1980).

[12] J. Skalski, Phys. Rev. C **77**, 064610 (2008).

[13] J. D. Cramer and J. R. Nix, Phys. Rev. C **2**, 1048 (1970).

[14] J. Dudek, Nuclear Physics A **194**, 552 (1972).

[15] A. Baran, J. A. Sheikh, J. Dobaczewski, W. Nazarewicz, and A. Staszczak, Phys. Rev. C **84**, 054321 (2011).

[16] H. Goutte, J. F. Berger, P. Casoli, and D. Gogny, Phys. Rev. C **71**, 024316 (2005).

[17] E. Flynn, D. Lay, S. Agbemava, P. Giuliani, K. Godbey, W. Nazarewicz, and J. Sadhukhan, Phys. Rev. C **105**, 054302 (2022).

[18] P. Talou and R. Vogt, eds., *Nuclear Fission: Theories, Experiments and Applications*, 1st ed. (Springer Cham, Cham, Switzerland, 2023).

[19] W. Younes, D. Gogny, and J. Berger, *A Microscopic Theory of Fission Dynamics Based on the Generator Coordinate Method*, Lecture Notes in Physics (Springer International Publishing, 2019).

[20] S. Bara, *Experimental and Theoretical Studies of β-Delayed Fission*, Ph.D. thesis, KU Leuven, Leuven, Belgium (2025).

[21] H. Krappe and K. Pomorski, *Theory of Nuclear Fission: A Textbook*, Lecture Notes in Physics (Springer Berlin Heidelberg, 2012).

[22] P. Ring, H. Massmann, and J. Rasmussen, Nuclear Physics A **296**, 50 (1978).

[23] J. Sadhukhan, J. Dobaczewski, W. Nazarewicz, J. A. Sheikh, and A. Baran, Phys. Rev. C **90**, 061304(R) (2014).

[24] R. Smolańczuk, J. Skalski, and A. Sobiczewski, Phys. Rev. C **52**, 1871 (1995).

[25] W. Younes and W. D. Loveland, *An Introduction to Nuclear Fission*, 1st ed., Graduate Texts in Physics (Springer Cham, Cham, Switzerland, 2021).

[26] J. D. McDonnell, W. Nazarewicz, and J. A. Sheikh, Phys. Rev. C **87**, 054327 (2013).

[27] T. Bürvenich, M. Bender, J. A. Maruhn, and P.-G. Reinhard, Phys. Rev. C **69**, 014307 (2004).

[28] P. Hohenberg and W. Kohn, Phys. Rev. **136**, B864 (1964).

[29] M. Stoitsov, Physics of Particles and Nuclei **41**, 868 (2010).

[30] N. Barnea, Phys. Rev. C **76**, 067302 (2007).

[31] J. Engel, Phys. Rev. C **75**, 014306 (2007).

[32] D. Lacroix, "Quantum nuclear many-body dynamics and related aspects," Research Report (CNRS, 2011).

[33] P. Ring and P. Schuck, *The Nuclear Many-Body Problem*, 1st ed., Theoretical and Mathematical Physics (Springer Berlin, Heidelberg, Berlin, Heidelberg, 1980) p. 718.

[34] D. Vautherin and D. M. Brink, Phys. Rev. C **5**, 626 (1972).

[35] G. Grams, N. N. Shchechilin, A. Sánchez-Fernández, W. Ryssens, N. Chamel, and S. Goriely, The European Physical Journal A **61**, 35 (2025).

[36] Lin, Lin and Wu, Xiaojie, ESAIM: M2AN **55**, 763 (2021).

[37] N. Zettili, *Quantum Mechanics: Concepts and Applications*, 2nd ed. (Wiley, 2009).

[38] A. Baran, K. Pomorski, A. Lukasiak, and A. Sobiczewski, Nuclear Physics A **361**, 83 (1981).

[39] M. Warda, J. L. Egido, L. M. Robledo, and K. Pomorski, Phys. Rev. C **66**, 014310 (2002).

[40] K. Pomorski, M. Warda, and A. Zdeb, Physica Scripta **90**, 114013 (2015).

[41] A. Baran, Physics Letters B **76**, 8 (1978).

[42] H. Hofmann, Z. Physik **250**, 14 (1972).

[43] F. Wagner, Classical and Quantum Gravity **41**, 045006 (2024).

[44] B. Podolsky, Phys. Rev. **32**, 812 (1928).

[45] O. von Roos, Phys. Rev. B **27**, 7547 (1983).

[46] E. Schrödinger, Phys. Rev. **28**, 1049 (1926).

[47] E. Merzbacher, *Quantum Mechanics*, 3rd ed. (Wiley, 1998).

[48] S. G. Nilsson, C. F. Tsang, A. Sobiczewski, Z. Szymański, S. Wycech, C. Gustafson, I.-L. Lamm, P. Möller, and B. Nilsson, Nuclear Physics A **131**, 1 (1969).

[49] D. L. Hill and J. A. Wheeler, Phys. Rev. **89**, 1102 (1953).

[50] B. R. Holstein and A. R. Swift, American Journal of Physics **50**, 833 (1982).

[51] W. H. Miller, N. C. Handy, and J. E. Adams, The Journal of Chemical Physics **72**, 99 (1980).

[52] H. Hofmann, Nuclear Physics A **224**, 116 (1974).

[53] J. Dormand and P. Prince, Journal of Computational and Applied Mathematics **6**, 19 (1980).

[54] L. Fox and E. T. Goodwin, Mathematical Proceedings of the Cambridge Philosophical Society **45**, 373–388 (1949).

[55] R. Friedman and M. Jamieson, Computer Physics Communications **85**, 231 (1995).

[56] P. Virtanen, R. Gommers, T. E. Oliphant, *et al.*, Nature Methods **17**, 261 (2020).

[57] T. Kawano, P. Talou, and S. Hilaire, Phys. Rev. C **109**, 044610 (2024).

[58] A. Sánchez-Fernández, S. Bara, W. Ryssens, and S. Goriely, Physics Letters B **880**, 140737 (2026).

[59] L. I. Schiff, *Quantum Mechanics*, 3rd ed., International Series in Pure and Applied Physics, Vol. 1 (McGraw-Hill, New York, 1968).

[60] P. Collas and D. Klein, "Exact solutions for compactly supported parabolic and landau barriers," (2026), arXiv:2601.06369 [quant-ph] .

[61] R. C. Sharma and M. D'Amico, Phys. Rev. C **47**, 2801 (1993).

[62] R. Rodríguez-Guzmán and L. M. Robledo, Phys. Rev. C **89**, 054310 (2014).

[63] Washiyama, Kouhei, EPJ Web Conf. **306**, 01026 (2024).

[64] R. Rodríguez-Guzmán, L. M. Robledo, and R. N. Bernard, Journal of Physics G: Nuclear and Particle Physics **51**, 115102 (2024).

[65] J. Sadhukhan, K. Mazurek, A. Baran, J. Dobaczewski, W. Nazarewicz, and J. A. Sheikh, Phys. Rev. C **88**, 064314 (2013).

[66] G. Scamps and K. Hagino, Phys. Rev. C **91**, 044606 (2015).

[67] K. Takatsuka, H. Ushiyama, and A. Inoue-Ushiyama, Physics Reports **322**, 347 (1999).

[68] M. Abramowitz and I. Stegun, *Handbook of Mathematical Functions with Formulas, Graphs, and Mathematical Tables*, NBS Applied Mathematics Series (U.S. Government Printing Office, 1964).